Sensors for Structural Control Applications Using Piezoelectric Polymer Film

by

Simon Andrew Collins

B.A.Sc. University of Toronto (1988)

SUBMITTED TO THE DEPARTMENT OF
AERONAUTICS AND ASTRONAUTICS
IN PARTIAL FULFILLMENT OF THE
REQUIREMENTS FOR THE DEGREE OF

Master of Science
in
Aeronautics and Astronautics
at the
Massachusetts Institute of Technology
September 1990

Signature of Author _____
Department of Aeronautics and Astronautics
August 17, 1990

Certified by _____
Professor Andreas H. von Flotow
Thesis Supervisor, Department of Aeronautics and Astronautics

Accepted by _____
Professor Harold Y. Wachman
Chairman, Department Graduate Comittee

Sensors for Structural Control Applications Using Piezoelectric Polymer Film

by

Simon Andrew Collins

Submitted to the Department of Aeronautics and Astronautics
on August 17, 1990 in partial fulfillment of the
requirements for the Degree of Master of Science in
Aeronautics and Astronautics

Abstract

This work explores the use of distributed piezopolymer sensors for structural control. These sensors integrate strain measurements weighted by the sensor's width along the length of the sensor. Various properties can be obtained by shaping the film's electrode in different patterns.

Several spatial shapes are investigated. Good modal filtering behavior is obtained with sensors which are shaped proportionally to the structure's modal strain shape. Two patterns are also developed which provide rolloff without phase lag. The exponential sensor provides first-order rolloff on a beam, whereas the sinc function sensor provides higher-order rolloff. Truncation effects are examined and suggestions made for leakage reduction. The experimental demonstration of these sensors correlates well with theory.

Transducer manufacture with polyvinylidene fluoride (PVDF) is described and recommendations are made for electrode shaping, bonding the sensor to the structure, making electrical connections and interfacing the sensor with conditioning electronics.

Thesis Supervisor: Dr. Andreas H. von Flotow
Title: Associate Professor,
Department of Aeronautics and Astronautics

Acknowledgements

At this time I would like to thank my advisor, Prof. Andy von Flotow, for all his assistance and his many insightful comments on this work. Dr. Dave Miller, my co-advisor, also deserves a great deal of credit. He got things moving again when I got bogged down in details. Both of these men did a very thorough job of proofreading this thesis, and I must take full responsibility for the remaining errors.

The SERC lab was a very friendly environment to work in, and thanks go to all who make up the lab, especially those who have helped me learn my way around the lab equipment. Jon and Doug deserve special mention for dealing with all my computer problems. Andrew G. was also instrumental in the completion of this thesis, or at least his Mac was.

I now understand why most textbooks are dedicated to the author's family. I'm very grateful that Lisa is such an understanding wife, and she really made a difference in those last couple of weeks.

Contents

List of Figures

List of Tables

Chapter 1

Introduction

The components of a closed-loop feedback system are usually separated into a plant, one or more sensors, one or more actuators, and the associated compensators. Sensor and actuator dynamics are often regarded as a source of error, as they are omitted from the simplest design studies. Even if an attempt is made to include these dynamics in an analysis, they may not be well characterized, so the sensor and actuator dynamics often act as constraints on the system's performance, limiting the gains and/or the bandwidth [1]. In order to achieve high performance, we must minimize the constraining aspects of these dynamics.

Of course, it would much better if these dynamics were actually working in our favor, rather than acting as a constraint. If the sensors and actuators were well characterized, the control system designer could choose the transducers that suited the rest of the system. And if the designer were lucky, transducers may be available which implement some aspect of the compensator.

This catalog-approach to control systems design is rather limiting, though, and it assumes that the sensors or actuators needed already exist. A more rationale way of going about this is to actually design the transducers, giving them the desired characteristics. This work has studied such an idea, in particular looking at sensors for structural control applications.

The research was further restricted to the use of piezoelectric polymer film for the transducer material. Piezoelectrics in general have been found to be a good choice for transducers for structural control applications [2], and piezopolymers offer the advantages of ruggedness, flexibilty and lightweight, making them very attractive sensor materials. Polyvinylidene fluoride (PVDF) was used on account of its high piezoelectric stress coefficients, resulting in a large field being developed under a given stress. PVDF is commercially available, easy to work with and has been studied before for use in structural control systems [3,4].

Previous research had revealed dramatic changes in the characteristics of distributed PVDF sensors and actuators when the film's spatial shape was changed [5–7]. This thesis examined the possibility of shaping PVDF sensors so as to achieve a particular sensor response. The associated manufacturing issues were also considered in the course of an experimental verification of some of the analytical findings. The work was restricted to one-dimensional sensors, as the piezoelectric anisotropy of PVDF makes an extension to two-dimensions somewhat difficult.

There are several areas of structural control that would seem to benefit from the use of these spatially distributed piezoelectric sensors. One such area is modal control [8]. Modal coordinates are needed to implement modal control, which usually necessitates an observer using physical measurements as its input states. There are problems with observation spillover here. These problems can be handled to some extent by an array of discrete sensors, but such an array has problems of its own, *e.g.* spatial aliasing. Modal sensors can be fashioned from PVDF to allow direct observation of the modal coordinates, and as the piezo film is continuously distributed, it is not affected by spatial aliasing.

Noncausal compensators for structural control have recently attracted some attention [9–11]. These offer truly remarkable performance. For example, it has been shown that it is theoretically possible to eliminate all the resonances of beam with a single actuator and a single sensor [12]. But this scheme can only be carried out if the compensator

has access to future measurements. These measurements can be made by using the fact that energy is propagating in the structure, so spatially distributed measurements can be thought of as measuring future and past information.

A more mundane example of a noncausal compensator is one with rolloff but without phase lag. There is a real need for such a filter, as high-frequency noise is often a factor that limits gains in experimental demonstrations of structural control. Several ways of achieving this type of filter with a spatially distributed piezo film sensor are presented, their limitations discussed and experimental demonstrations provided.

The overall objective of this work was demonstrate the ability to create piezopolymer sensors which have interesting and unusual characteristics. Specifically, these characteristics were intended to make the sensors useful for structural control applications.

The following steps were taken to meet this objective and will be presented in this thesis. PVDF is examined as a piezoelectric material and as a potential structural sensor in Chapter 2. This includes a discussion of the previous research that made use of PVDF as a sensor or an actuator in structural control experiments. Some details of the development of piezopolymers will be given, as will be some tips on transducer fabrication with this material. This experience was built up over the course of constructing a number of distributed sensors.

The subject of Chapter 3 is the implementation of modal filters with PVDF. Some modal theory is reviewed, and the required shaping for a modal sensor is derived. This is a sensor which only observes a single mode. Several of these sensors were designed for Martin Marietta's Large Space Manipulator. The selection of the spatial sensor pattern is presented in detail, and experimental results are shown. An attempt was also made to place strain gauges such that some modes are unobservable. The results of this will be compared with the modal sensors.

While all the resonances of a beam were not eliminated in the course of this work, two different sensors were designed to give magnitude rolloff without phase lag. By combining the piezoelectric sensor equation with the output of a conventional point sensor, these

sensors can be interpreted as spatial filters, taking the point sensor's output and filtering it. As the filtering is done in the spatial domain, causality is not a constraint, and a response such as magnitude rolloff without phase lag becomes possible. Using infinite domain analysis, an exponential sensor and a sinc function sensor were designed. These names refer to the actual shape of the film's electrode. The exponential sensor provides second-order rolloff in the wavenumber domain, while the sinc function sensor acts as an ideal filter. As both these functions are infinte in extent, it is necessary to truncate them; the errors introduced by this operation are studied. Frequcncy responses were predicted and experimentally verified. This work is presented in Chapter 4.

Finally, conclusions and suggestions for further work are covered in Chapter 5.

Chapter 2

"Tough Plastic With A Sensitive Side"

The sensors that will be discussed in the following chapters all exploit the versatility of the piezoelectric polymer from which they are made, so it is important that the reader has some understanding of this material, polyvinylidene fluoride (PVDF or PVF_2). Not only will a brief description of the material and some applications be presented, but an attempt will be made to show this polymer's place in the broader field of piezoelectricity. Finally, some lessons learned in the course of manufacturing the sensors will be given.

2.1 A History of Piezoelectricity

Piezoelectricity has been studied for about 110 years now, and the field could certainly be considered mature scientifically. Applications have been well developed; the understanding of the important phenomena is currently such that devices relying on the accurate prediction of nonlinear effects can be built. A thorough discussion of the many aspects of piezoelectricity is clearly beyond the scope of this work. Any reader seeking more detail should consult Cady's monumental text [13]. He provides a lucid synthesis of the developments up to 1945, and so deals almost exclusively with crystals. Jaffe *et*

al. present an interesting multidisciplinary view (one author is a crystallographer, the second a ceramist and the third a physicist) focusing on piezoceramics [14]. But a single monograph of this calibre covering piezoelectric polymers has not yet emerged. There is certainly no shortage of related literature—over 2500 articles (including many reviews) are cited in Lang's bibliographies on piezoelectricity and pyroelectricity of polymers [15]. These bibliographies are published quasi-annually in the journal *Ferroelectrics*, which has also devoted several special issues to PVDF [16,17]. But there was a great deal of developmental work that went on before things got to this stage.

2.1.1 Piezocrystals

The brothers Jacques and Pierre Curie are the acknowledged fathers of piezoelectricity. They were by no means the first to study charge-producing phenomena; the Greeks had been fascinated by the static electricity developed when *elektron* (amber) was rubbed [18]. In the eighteenth and nineteenth centuries many similar effects were recognized and classified. However, the Curies were well prepared to discover the direct piezoelectric effect—Pierre had been studying the relation between pyroelectricity and crystal symmetry. They expected to find that the application of pressure along certain axes of certain classes of crystals would lead to the production of charge. By 1880 they had observered both the transverse and the longitudinal effect in ten types of crystals, including quartz and Rochelle salt [19].

Crystallographers had been studying pyroelectricity for about fifty years at this point. The pyroelectric effect is the change in polarization exhibited by certain crystal classes when exposed to temperature changes [13]. The Curies felt there was a direct correspondence between the electrical effects of thermal and mechanical deformation—they claimed to have discovered a new method to observe the same phenomenon. Hankel did not agree: Based on some earlier work with quartz [20], he contended the Curies' observations had a significantly different cause, "und ich habe sie deshalb als Piezoelektricität unterschieden [and I have therefore distinguished it as piezoelectricity]" [21], *piezein* be-

ing Greek for *to press*. The phenomenon now had its own name, and more complications soon followed.

One of the Curies' contemporaries was examining the application of thermodynamic principles to reversible processes involving electric quantities. Lippmann used the Curies' results as an example and asserted a corresponding converse phenomenon should exist [22]. The Curies proceeded to verify experimentally this "phénomène réciproque" before the end of the year [23]. The converse piezoelectric effect causes a piezoelectric crystal to become strained by an amount directly proportional to the applied electric field.

In an attempt to explain these observations, a phenomenological theory of piezoelectricity was being developed independently by several scientists, including Lord Kelvin, P. Duhem and F. Pockels. But the greatest advances were made by Woldemar Voigt. Challenged by what he called the most complicated branch of crystal physics, he sought a rigorous formulation which would clarify the relations between piezoelectricity and crystal structure. In 1890 he presented a theory [24] which combined the symmetry of electric vectors and elastic tensors with the geometric symmetry of crystals to determine which of the 18 piezoelectric coefficients (six stress components and three electric polarization components) would be nonzero for the various crystal classes; this theory was improved over the next four years [25].

2.1.2 Crystal Applications

For the first several decades, piezoelectricity was regarded as little more than a scientific curiosity, although the effect had been put to limited use in some scientific instruments. Characteristically, it was the Curies who suggested many such devices. In Jacques's doctoral dissertation of 1888 [26], he discussed the "quartz piézoélectrique," which was a suspended quartz plate with an attached scalepan. This used the transverse effect to produce known charges for the measurement of voltages, currents, capacitances and pyro- and piezoelectric effects in other crystals. Marie and Pierre Curie made use of a similar instrument to measure radioactivity [27]. Pierre and Jacques also developed a

piezoelectric manometer and a piezoelectric electrometer [13], but the credit for the first practical application of piezoelectricity would go to another Frenchman, Paul Langevin.

During the First World War, many countries put a great deal of effort into research on ways of detecting submarines and mines. As radio waves are quickly attenuated by sea water, Langevin was working on using quartz plates to produce high-frequency sound waves under water. Tests conducted in the River Seine between December 1915 and March 1916 revealed that he could radiate much more power by using, instead of a single thick quartz plate, a mosaic of quartz sandwiched between two steel plates [28]. By October 1918 he was able to use his "condensateur chantant [singing condenser]" as both an emitter and a receiver. The device was successfully patented in several countries [29], but it was completed too late to see any action in the war. The Langevin Supersound Source Projector did lead, however, to dramatic improvements in depth sounding [30]. The term "ultrasonic" only became prevalent after the Second World War, so as to distinguish high-frequency waves from the high speeds being attained by aircraft.

Meanwhile the scientific instruments taking advantage of piezoelectricity had become much more sophisticated. For example, high-power ultrasonics were being used to study liquids and biological samples [31] and the measurement of velocity dispersion in liquids and gases was now possible with either an acoustic interferometer or an optical diffraction grating [13]. Another important device was the piezoelectric resonator, which had been employed in scientific labs for the measurement of elastic constants. But it was the use of the resonator by the communications industry that really spurred the development of piezoelectric applications.

Stabilizers, oscillators and filters are all considered to be resonators as they are designed to operate at the resonant frequency of the crystal. They take advantage of both the direct piezoelectric effect and the converse one to operate with very little loss; in electrical engineering terminology, they have a very high Q factor. Langevin, in his U.S. patent [29], mentioned that quartz was the "frequency-determining element," but Nicolson and Cady were the true inventors of reliable oscillators for frequency con-

trol [32, 33]. The U.S. National Bureau of Standards quickly realized these oscillators provide ideal frequency standards [34], and once it was found that quartz crystal could be temperature-compensated through the use of special crystallographic cuts, they became a practical way of stabilizing the frequency of a transmitter. Such stabilizers saw widespread use in the communication sets of tanks and aircraft in World War II [31]. Mason modified these resonators so that the bandwidth was wide enough for use in carrier communication systems [35]. Coupled with the low dissipation in the crystal filter, this allowed the transmission of many conversations on a single circuit, making transatlantic communication much more efficient. The great stability and the superior temperature characteristics of single-crystal quartz have ensured that it remains the material of choice for high-quality resonators.

2.1.3 Ferroelectrics

A new class of materials was emerging at this time. Rochelle salt had been included in the Curies' first studies [19] and continued to attract a great deal of interest on account of its huge piezoelectric effect—its piezoelectric strain constant d_{14} can be thousands of times greater than quartz's [13]. The crystals are grown from a solution of the natural tartaric acid of grapes, which gave researchers more control over supply than was the case with quartz. The salt had been synthesized since 1655, when the pharmacist Elie Seignette in the seaport of La Rochelle started promoting it as a mild cathartic and diuretic [36], which explains both its names: Rochelle or Seignette salt. Although Nicolson demonstrated loudspeakers, microphones and phonograph pickups made of Rochelle salt crystals [32], an anomalous electrical effect was not thoroughly investigated until 1921 [37].

It had been observed that the electric displacement along one crystal axis was not uniquely determined by the applied electric field; it depended on its field history, suggesting spontaneous polarization. Valasek explained this with a ferromagnetic analogy: just as ferromagnetics are characterized by maximum permeability at the Curie point,

above which the permeability decreases rapidly, ferro*electrics* are characterized by a similar change in their dielectric constant. Rochelle salt has both an upper and lower Curie temperature, but this is unusual for ferroelectrics [13]. Above the Curie temperature, *i.e.* in the paraelectric region, the polarization is directly proportional to the applied field. However, in the ferroelectric (or Seignette-electric) region, the relation between polarization and field is nonlinear, so the crystal exhibits a distinctive dielectric hysteresis [37].

The combination of the induced polarization caused by the applied electric field and the spontaneous polarization makes ferroelectrics more sensitive than piezoelectric crystals, and it gives them greater electromechanical coupling (the ability to convert electrical energy to mechanical energy and vice versa). Attempts were made to exploit this in applications like submarine sound transducers, but some of the characteristics of Rochelle salt (poor mechanical strength, prone to dehydration, decomposes above 55°C) were real limitations [31]. The stability of quartz could not be rivaled for resonators, and ammonium dihydrogen phosphate (ADP) was found to be more suitable for hydrophones.

The introduction of ADP in the 1940s was due to the research that was turning up more ferroelectric materials. Busch and Scherrer had been quick to announce "a new Seignette-electric substance" in 1935 [38] but the more significant discovery was cloaked in wartime secrecy. Two teams had been working independently on ferroelectric polycrystals: Wul in the Soviet Union [39,40] and Von Hippel at M.I.T.'s Laboratory for Insulation Research [41]. They were investigating the effect of polarization on barium titanate ($BaTiO_3$) and found that, by applying a strong field at temperatures above the Curie temperature and maintaining the field as the temperature was lowered, the ceramic could be turned into a ferroelectric. It is interesting to note that Wul felt the evidence in his first study of $BaTiO_3$ did not "permit it to be classed with the group of Rochelle salt dielectrics" [39]; it was only once a dielectric hysteresis was noted that he believed $BaTiO_3$ is indeed a ferroelectric [40].

Ferroelectric ceramics were found to have greater coupling than quartz, and, because

they are polycrystals, the polarization is more stable than with single crystals, such as quartz or Rochelle salt. The ceramics could also be molded in a number of useful forms. The applications blossomed when it was found that solid solutions of lead zirconate titanate (PZT) have strong piezoelectric properties [42]. Not only does PZT have greater piezoelectric coefficients than $BaTiO_3$, it has a higher Curie temperature (340°C *vs* 120°C), giving it a wider operational temperature range [14]. The piezoelectric market has become dominated by PZT in the last couple of decades.

2.1.4 Piezoelectric Polymers

Piezoelectricity had always been associated with crystal physics. So the suggestions, made in the 1920s, of piezoelectric effects in noncrystalline materials [43, 44] would have indicated a significant discovery, but the experts quickly dismissed these reports. Cady [13] was clearly not convinced:

> Considering the erratic and qualitative character of most of this testimony and the likelihood that the results were due largely to contact potentials, such observations should not be taken too seriously as indicating anything that can properly be called a piezoelectric effect.

And that is where matters remained for several decades.

In the 1950s, Japanese and Soviet workers initiated the quantitative investigation of noncrystalline materials that would put these early observations on somewhat firmer ground. Wood was the first polymeric material to give them the evidence needed to refute the sentiments expressed by Cady. Values for the piezoelectric strain coefficient d_{14} were found to be approximately one twentieth of d_{11} of quartz [45, 46]. The origin of this effect was ascribed to the piezoelectric property of crystallites of cellulose; wood consists of oriented fibers in which many such crystallites are aligned along the fibers. Fukada and Yasuda [47] later found the piezoelectric constant of bone was more than twice that of wood. In this case, the origin of the effect is thought to be the uniaxial orientation of the crystalline micelle of collagen molecules which make up the hard outer

layers of bone. Perhaps these discoveries reinforced the ties between piezoelectricity and crystal physics after all.

However, these ties were radically changed by further work with biological substances. Fukada [48] described the piezoelectric effect in soft tissues such as skin, blood vessels and the intestines. He attributed the effect to the orientation of protein fibers, and the study of the piezoelectricity of synthetic polypeptides suggested it originated in the asymmetry of the atomic configuration in polypeptides. Reminiscent of Nicolson's work with Rochelle salt [32], Fukada constructed a phonograph pickup, a microphone and even an earphone from poly-γ-methyl-L-glutamate. The piezoelectricity of biological polymers is an area of study that has grown rapidly and has suggested some fascinating physiological theories. The state of the art is demonstrated in the proceedings of an international symposium dedicated to this topic [49].

Japan was clearly the leader in the field of piezoelectric polymer studies at this time. Fukada, in the conclusions of his paper on the piezoelectric effect in wood, suggested "it might not be too absurd to imagine the creation of highly piezoelectric plastics which are artificially manufactured from linear high polymers" [46]. Fourteen years later, in 1969, Kawai announced that "a new type of piezoelectric effect has been discovered in elongated and polarized films of polymers" [50]. The films were polarized in a manner similar to that described above for ceramics, but they were stretched to several times their original length before applying the electric field. More than ten types of polymers were tested, with a strong piezoelectric effect being found in six of them. Of these, polyvinylidene fluoride (PVDF) was by far the most active, with a piezoelectric strain constant d_{31} more than three times greater than the values measured for the other polymers. Another attraction of PVDF was that, along with poly(vinyl fluoride) and poly(vinyl chloride), little change was observed in the piezoelectric effect over the course of several months. These materials are obviously much more attractive for applications than polycarbonate, polyethylene or polytetrafluorethylene; the piezoelectric effect of the latter polymers had half-lives of one to four days [50]. The large stable piezoelectric

effect in PVDF sparked extensive research and development, as will be described in subsequent sections. Other polymers have received attention [51], but their piezoelectric effects have not really been exploited in applications.

2.2 Polyvinylidene Fluoride

Almost all the interesting applications of PVDF rely on the piezo- or pyroelectric properties which are present only after processing. The unpolarized form of this polymer is clear, lightweight, tough and compliant. Chemical companies, such as Pennwalt in America, Solvay in Belgium and Kureha in Japan, had been examining PVDF because it is not degraded by ultraviolet radiation (the bane of most polymers) and it is resistant to many chemicals. The flexible sheets allow coverage of diverse shapes, making this an ideal coating to provide protection from harsh environments. Chemical vat liners, cladding for exposed metal on skyscrapers, cable insulation and molded pipes are all examples of this application of PVDF [52], but there is not much scope here for active control. A more detailed examination of the material is required to understand the changes that make PVDF so fascinating as a transducer. The four basic steps involved in the creation of piezoelectric PVDF are: creation of the polymer; extrusion and stretching; poling; and surface metallization (sometimes carried out before poling). The polarized film has aroused a remarkable degree of interest, with coverage ranging from the popular press (from which the chapter title was taken) [52] to the more usual technical articles [16,17]. The following description will draw heavily on the latter, especially Pennwalt's technical manual [53] and Sessler's review [54].

2.2.1 Polymer Structure

PVDF starts its life as the monomer vinylidene fluoride, $CH_2=CF_2$. When polymerized, forming polyvinylidene fluoride, the long-chain molecules are arranged in a head to tail orientation based on the repeat unit (CH_2-CF_2-). Head to head and tail to tail chain

defects occur in only a few percent of the sequences [55]. As is usual for semicrystalline polymers, PVDF consists of crystallites embedded in an amorphous phase and an intermediate phase. The lamellar crystallites, which make up about half the material, are roughly 10 nm thick and up to 100 nm long. The amorphous phase has supercooled-liquid properties, with a glass-transition temperature T_g of about $-40°C$. Each molecule has an extended length of 500 nm and typically stretches through several crystalline and amorphous regions [54].

The four common crystalline forms of PVDF are called Forms I, II, III and II_p (IV) or β, α, γ and α_p (δ) phases, respectively [54]. The identity and crystalline structure of these forms have been studied by infrared transmission and X-ray scattering. Projections of the structure onto a plane normal to the molecular axis are shown in Fig. 2.1 [56]. Note that Form II_p has the same configuration as Form II except that every second chain has been rotated such that all chains are aligned, resulting in a polar crystal. A fifth polymorph has also been discovered [57]; the ϵ phase is the result of the reverse chain rotation occurring in Form III, producing an antipolar crystal. This form is rare and difficult to observe. In his review [54], Sessler provides a crystallographic description of Forms I–IV. The various forms may be obtained from a melt or from solutions, or they can be interconverted. Figure 2.2 [56] illustrates some of these procedures.

2.2.2 Physical Properties

Being a polymer, PVDF is lightweight and flexible. After stretching the film to effect a phase conversion, it has a Young's modulus of 2 GPa, making it more than thirty times as compliant as PZT. Lead zirconium titanate is also more than four times as dense as PVDF, which has a density of 1780 kg/m^3. Thus, sensors made of PVDF will have much less effect on the dynamic properties of the structure to which they are attached. Another result of the low density is an acoustic impedance which is near that of water, human tissue and other organic materials ($Z_a = \rho v_s$, where v_s is the speed of sound in the material). For PVDF, the acoustic impedance through the thickness is

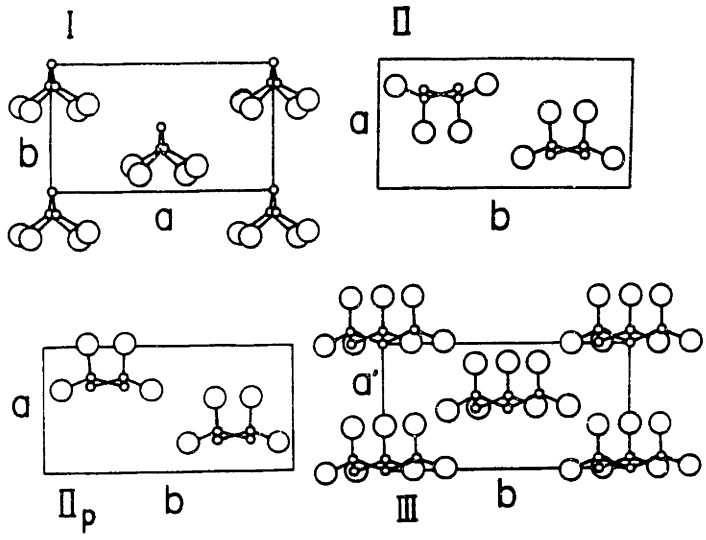

Figure 2.1: Crystalline structure of PVDF Forms I(β), II(α), II_p(α_p) and III(γ) projected onto the a–b plane of the unit cell. Fluorine atoms are shown as large circles, carbon atoms as small circles and hydrogen atoms are omitted.

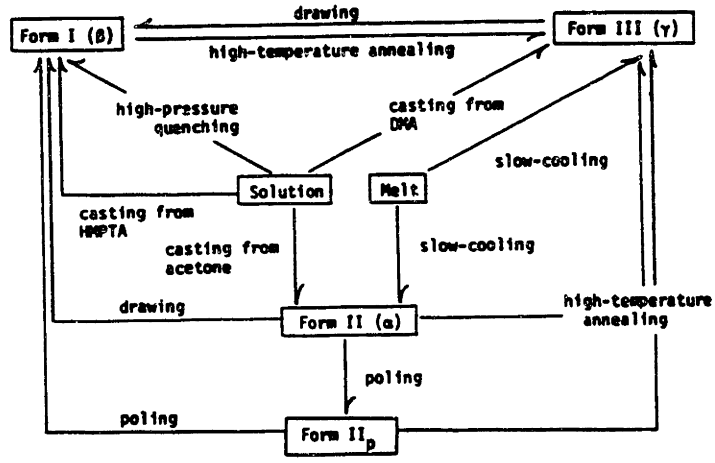

Figure 2.2: Production and conversion of the forms of PVDF. HMPTA: hexamethylphosphorictriamide; DMA: dimethylacetamide.

2.6 times that of water ($1.5 \times 10^6\,\mathrm{kg/m^2 \cdot sec}$), whereas PZT's is 16 times greater [53]. A close impedance match will ensure that little of an acoustic signal is reflected at a water-PVDF boundary, maximizing the signal to be sensed.

The dielectric nature of PVDF is determined to a great extent by its monomer constituent because there are so few configuration defects in the long-chain molecules. Thus, the polymer exhibits the large net dipole moment of vinylidene fluoride, $7.56 \times 10^{-30}\,\mathrm{C \cdot m}$ [53], resulting in a permittivity which is high for a polymer: the relative permittivity ϵ_R (the ratio of the material's permittivity to that of free space) is roughly 12 [51]. This is, however, much smaller than the permittivity of ceramics, *e.g.* $\epsilon_R = 1200$ for PZT. The low dielectric constant of PVDF can be a disadvantage for sensor applications, as it necessitates the use of an impedance match circuit to minimize the capacitive shunting effects. The effect of the low permittivity on the piezoelectric constants will be noted below. On the other hand, PVDF has greater dielectric strength than ceramics; for 28 μm film, the dielectric strength is about 70 V/μm, which is much greater than PZT's 1 V/μm [53] and allows stronger fields to be applied.

A summary of the physical properties of PVDF and other piezoelectric materials is presented in Table 2.1 [53,54].

PVDF is quite a lossy material, both electrically and mechanically: $\tan\delta_e \simeq 0.018$ and $\tan\delta_m \simeq 0.10$ [53]. This leads to highly damped resonance frequencies, which contrasts sharply with the behavior of quartz, $\tan\delta_e < 10^{-6}$ [13]. The reason for the use

Table 2.1: Comparison of piezoelectric materials—physical properties.

Material	ρ ($10^3\,\mathrm{kg/m^3}$)	E (GPa)	ϵ_R	Z_{a3} ($10^6\,\mathrm{kg/m^2 \cdot sec}$)
Quartz	2.7	80	4.5	15
Rochelle Salt	1.8	20	350	5.6
$BaTiO_3$	5.7	110	1700	30
PZT	7.5	80	1200	24
PVDF	1.8	2	12	3.9

of quartz in resonators is clear.

As could be expected of a viscoelastic polymer, the electrical and mechanical properties exhibit both temperature and frequency dependencies. The properties also vary with the crystal form and the amount of stretching; Pennwalt provides details on the temperature and frequency dependencies of electrical properties of KYNAR piezo film [53], but little data is provided on the mechanical relaxation behavior.

The effect of the glass-transition temperature is strong [54]; the dielectric loss tangent $\tan \delta_e$ peaks at T_g, and the dielectric permittivity ϵ_{33}, Poisson's ratio ν_{31} and the elastic compliances s_{11} and s_{22} all increase sharply at this point ($-40°$C).

The film is inherently capacitive, so it is must be used dynamically. But it has a very wide bandwidth. Several factors affect this. The dielectric permittivity of the polymer varies with frequency. There are two regions, one near 0.1 Hz and the second starting at 10^7 Hz, where ϵ_R is proportional to the logarithm of the frequency; it is reasonably independent of frequency between these regions [54]. The film's internal resonances also affect the frequency response, with the natural frequency through the thickness being given by $f_r = v_s/(2t)$. Substituting the acoustic speed (2.2 km/sec [53]), it is clear that the resonance values will range from 1 MHz (for 1 mm films) to 120 GHz (for 9 μm film, Pennwalt's thinnest). The electrical impedance of the film has the usual capacitive frequency relationship, $Z_e = 1/(\omega C)$.

Uniaxial or biaxial stretching is used to improve the mechanical or electrical properties of the film or to change the crystallites from one form to another. For example, stretching α-phase PVDF up to draw ratios of 4:1 will generate β-phase material. If uniaxial stretching is continued until the onset of superplastic deformation, the mechanical and electrical properties of the PVDF film will be improved; Nix *et al.* were able to double both Young's modulus and the hydrostatic piezoelectric strain constant by using these large draw ratios (up to 7:1) at temperatures up to 140°C before polarization [58]. The draw ratio has a great effect on the Poisson's ratios. For unstretched film, ν_{31} is 0.37, but this rises to 0.7 for films subjected to a draw ratio of 4.5:1. Over the same

interval ν_{21} falls from 0.35 to 0.25 [54]. The *1* axis is the direction along which the film is stretched. The permittivity of drawn film is almost 50% greater than that of the undrawn PVDF; this has been attributed to the reorientation of the crystal lamellae that occurs during stretching [54].

At some point during manufacture, both sides of the film will be coated with conductive metals. These electrodes provide intimate electrical connection with the polymer, allowing one to apply electric fields to the film or to collect the charges which have accumulated at the surface. The electrodes can affect the piezoelectric properties by constraining the film, preventing a truly stress-free condition from being established. Two forms of metallization are available for KYNAR films: thin metal layers deposited by vacuum metallization and thicker coatings deposited by spraying or by silk screening with a conductive silver ink. The vacuum deposited electrodes can be made using a wide variety of metals; typical combinations are nickel/copper or nickel/aluminum. The metal thickness ranges from 250–1000 Å. The silver ink electrodes are much more rugged but are also thicker (5–7 microns). These electrodes can mass load the system, changing the dynamic response of the film [53].

2.2.3 Poling and Polarization

Most commercially available PVDF film consists of antipolar Form II crystallites. This must be processed before it becomes piezoelectric (Fig. 2.3). The subsequent piezoelectric coefficients are highly dependent on how this is performed; Pennwalt claims to have improved d_{31} by an order of magnitude over the last ten years through an increased understanding of these processes [53].

The film is first uniaxially stretched at 60–65°C to 3–5 times its original length. The material will recrystallize as Form I due to the packing of unit cells in parallel planes during the drawing [54]. Subsequent annealing of the (still stretched) sample will heal any damage due to the stretching and will stabilize the film. Poling can then be performed using either a thermal or a corona procedure.

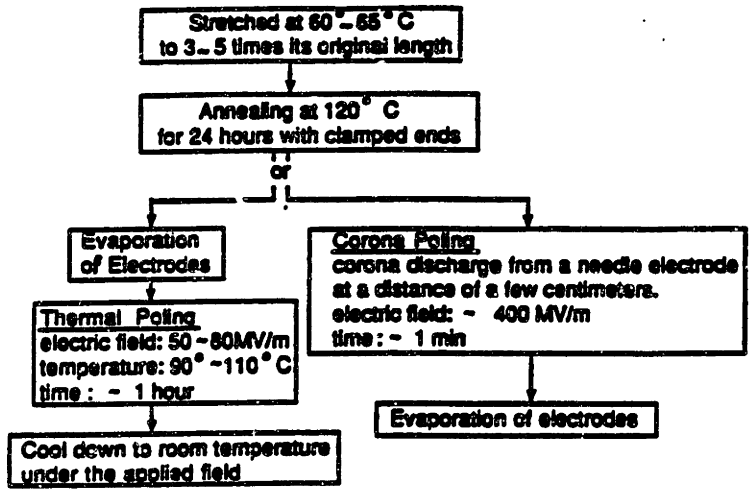

Figure 2.3: Processing of Form II PVDF to yield piezoelectric film.

In the case of thermal poling, electrodes are first placed on the film, then it is subjected to a field of 50–80 MV/m at 90–110°C for about an hour. This partially aligns the dipoles in the crystalline regions in the field direction; Pennwalt always uses the thickness axis as the polarization axis. The electric field is maintained as the film is cooled to room temperature, stabilizing the polar alignment and causing a permanent polarization. If poled for a long enough time, the polarization is only a function of the poling field—the temperature determines the rate of polarization build-up. For applied fields of up to 200 MV/m the polarization achieved is proportional to the field. For stronger fields, a maximum polarization of about 20 mC/m^2 is reached [54]. This is considerably lower than the polarization attained in PZT, which can approach 400 mC/m^2 [14]. If weak fields are used, the resulting polarization is spatially nonuniform: greater piezoelectric act ity is found near the positive electrode, which has been attributed to space-charge injection [54].

For corona poling, the film is either nonmetallized or has only had one electrode applied. It is then subjected to a corona discharge from a needle electrode at a distance of a few centimeters. A charge builds up on the film which causes a strong field in the material. This field aligns the dipolar chains even at room temperature. If the field resulting from the corona charge is less than 100 MV/m, little polarization results. For

greater fields, the polarization rises sharply and assumes a saturation value of about 120 mC/m^2 [54]. This polarization tends to be centered around the needle position with field-compensating charges at the polarization-zone boundaries.

Either poling process causes dipolar alignment through the reorientation of the randomly oriented crystalline regions. The fluorine atoms are attracted to the positive electrode, and the hydrogen atoms are attracted to the negative electrode. Recall that molecular chains pass through several regions, so it is not possible to align the entire crystallite with the field. Instead, chain rotations occur. Because of the molecular bond angles, only discrete orientation directions are possible for the chains [60], and if the chain axis has a component normal to the electrodes an incomplete alignment will be achieved.

2.2.4 Origins of the Piezoelectric Effect

The piezoelectricity of PVDF has been fairly well modelled [54]. The models assume the material consists of a crystalline and an amorphous phase, with the two phases differing in their dielectric and elastic properties. The material's polarization is due to aligned dipolar chains in the crystalline and perhaps the surrounding amorphous regions. Injected charges at the boundaries of the polarization zones also contribute to the polarization. There are three primary mechanisms which cause piezoelectricity in such a material:

A. Electrostrictive Contribution The strain dependence of the dielectric constants of the crystalline and amorphous parts differ. In the presence of polarization, this produces a piezoelectric effect.

B. Dimensional Contribution The elastic constants of the crystalline and amorphous regions are different. This causes the polarization to have a strain dependence, thereby contributing to the piezoelectric activity.

C. Crystal Contribution The crystallites have an intrinsic piezoelectricity effect due to the strain dependence of their polarization.

Wada and Hayakawa [59] have numerically evaluated a theory based on the above assumptions. They obtained good agreement between their predicted piezoelectric constants and experimental data. Mechanism B predominated for all constants. In the case of the transverse effect (d_{31} or d_{32}), the dimensional contribution is proportional to the appropriate Poisson's ratio μ_{3i}. This reinforces the claim that the temperature dependence of the Poisson's ratios has a direct effect on the piezoelectric constants. The ferroelectric behavior of PVDF (reversal of polarization by a strong electric field, hysteresis of piezoelectric constants) is also predicted by this theory.

2.2.5 Piezoelectric Constants

The relationship between the mechanical and electrical behavior of piezoelectric materials is expressed through a number of coefficients. Two subscripts are used with the piezoelectric constants, the first identifying the axis of induced or applied electrical field, the second referring to the axis of induced mechanical strain or applied stress. Any purely symmetric crystal will not be piezoelectric, so PVDF must be anisotropic. The severe stretching the film is subjected to during manufacture also contributes to the anisotropy. This will be dealt with by using the following axes definitions: the *3* axis corresponds to thickness and the *1* axis corresponds to the draw direction in the case of uniaxial stretching (Fig. 2.4). Tensile mechanical forces are taken as positive, as is

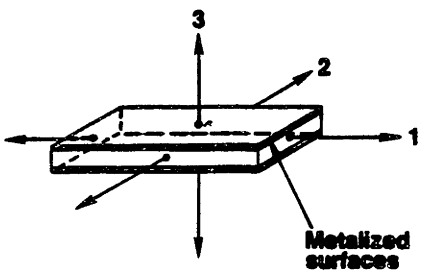

Figure 2.4: Definition of material axes.

Table 2.2: Compressed matrix notation.

ij or kl	p or q
11	1
22	2
33	3
23 or 32	4
31 or 13	5
12 or 21	6

an increase in charge polarization. Thus, a positive electric field is one which is in the same direction as the original poling field. The anisotropy also necessitates the use of subscripts for the permittivity constants, the compliances, etc. Rather than the usual tensor notation, I.E.E.E. compressed matrix notation will be used [61]. This consists of replacing subscript pairs ij or kl by p or q according to Table 2.2. So, for example, the compliance s_{yyxz} ($\equiv s_{2213}$) will now be given by s_{25}.

Four variables are considered when defining the piezoelectric constants: the electric displacement D; the mechanical strain S; the electric field intensity E; and the mechanical stress T. Combined with the compressed matrix notation, we have $\sigma_{xx} \equiv T_1$, etc. When used as a superscript, these variables represent a boundary condition which is fixed, *e.g.* T^{E} is the mechanical stress under short circuit conditions and E^{T} is the electric field under stress free conditions. To define any constant properly the electrical and mechanical boundary conditions must be given.

When an electric field is applied to piezo film under stress free conditions, all three film dimensions change. The piezoelectric strain constant d is the ratio of charge per unit electrode area to the applied stress under short circuit conditions. It is also the ratio of the developed strain to the applied field in the stress-free condition.

$$d_{ip} = \frac{D_i}{T_p^{\mathrm{E}}} = \frac{S_p}{E_i^{\mathrm{T}}} \tag{2.1}$$

The piezoelectric strain constant has units of C/N or m/V.

The piezoelectric stress constant g is the negative of the ratio of the induced electric field to the applied stress under open circuit conditions. It also expresses the induced strain relative to the applied electric charge per unit electrode area under stress free conditions.

$$g_{ip} = \frac{-E_i}{T_p^{\mathrm{D}}} = \frac{S_p}{D_i^{\mathrm{T}}} \tag{2.2}$$

This constant has units of $\mathrm{V \cdot m/N}$ or $\mathrm{m^2/C}$.

Two further coefficients complete the definitions: the piezoelectric field intensity constant e [$\mathrm{C/m^2}$ or $\mathrm{N/V \cdot m}$] and the piezoelectric displacement constant h [V/m or N/C].

$$e_{ip} = \frac{D_i}{S_p^{\mathrm{E}}} = \frac{-T_p}{E_i^{\mathrm{S}}} \tag{2.3}$$

$$h_{ip} = \frac{-E_i}{s_p^{\mathrm{D}}} = \frac{-T_p}{D_i^{\mathrm{S}}} \tag{2.4}$$

These constants are related by the permittivity matrix ϵ and the stiffness tensor c .

$$d_{ip} = \epsilon_{ij}^{\mathrm{T}} g_{jp} \tag{2.5a}$$

$$e_{ip} = \epsilon_{ij}^{\mathrm{S}} h_{jp} \tag{2.5b}$$

$$e_{ip} = d_{iq} c_{qp}^{\mathrm{E}} \tag{2.5c}$$

$$h_{ip} = g_{iq} c_{qp}^{\mathrm{D}} \tag{2.5d}$$

where $i, j = 1, 2, 3$ and $p, q = 1, 2, \ldots, 6$ and implicit summation notation is understood. The electric and mechanical fields are now coupled, the extent being determined by the number of nonzero piezoelectric coefficients.

The energy stored in these fields and the ability to exchange one form of energy for another is expressed by the electromechanical coupling factor k. The square of k is the ratio of the stored mechanical energy to the total stored energy, and is related to the other piezoelectric constants by means of the stiffness tensor:

$$k_{ij}^2 = g_{iq} c_{qp}^{E} d_{jp} \tag{2.6}$$

The piezoelectric coefficients of PVDF have been the object of a number of experimental investigations. A wide range of values have been reported, and the variation of these coefficients with assorted parameters, such as temperature, electric field, etc., has been studied. Table 2.3 presents Pennwalt's data on KYNAR piezo film [53]. The anisotropy between the *1* and *2* directions is well known and due in large part to the uniaxial stretching; biaxial film is also marketed. Electromechanical coupling factors as high as 20.5% for PVDF have been reported in the literature [62]; Pennwalt has attained values near 30% for the copolymer VF_2/VF_3 [53]. Currently, much of the basic research is devoted to PVDF's copolymers, especially poly(vinylidene fluoride-trifluorethylene) [63]. All of the quoted coupling factors represent values attained at frequencies between 100 and 1000 Hz. The coupling factor k_{31} tends to be almost 50% lower below 100 Hz [53]. This effect has been attributed to internal relaxation mechanisms affecting the Poisson's ratios and is not nearly as strong for k_{33}.

A summary of the piezoelectric properties of PVDF and other piezoelectric materials is presented in Table 2.4 [53,54]. Note that PVDF's piezoelectric stress constant g_{31} is greater than PZT's, while the strain constant d_{31} is smaller. This can be explained by combining the low permittivity of PVDF (Table 2.1) with Eq. (2.5a), $d = \epsilon^T g$.

The primary piezoelectric activity is considered to be the longitudinal effect (electrical and mechanical action along the same axis). The transverse effect is largely due to the lateral contraction of the film and so is determined by the Poisson's ratio ν_{31}. This conclusion is based primarily on the behavior of the electromechanical coupling

Table 2.3: Typical piezoelectric constants of KYNAR piezo film.

Strain Constants (pC/N)		Stress Constants (mV·m/N)		Coupling Factor	
d_{31}	23	g_{31}	216	k_{31}	12%
d_{32}	3	g_{32}	19		
d_{33}	-33	g_{33}	-339		

Table 2.4: Comparison of piezoelectric materials—piezoelectric properties.

Material	d_{31} (pC/N)	g_{31} (mV·m/N)	k_{31} (%)
Quartz	2	50	9
Rochelle Salt	280	90	73
$BaTiO_3$	78	5	21
PZT	110	10	30
PVDF	23	220	12

factor [54]: For a given sample, k_{33} always exceeds k_{31}, and k_{33} is almost independent of temperature, while k_{31} exhibits a rise with temperature similar to ν_{31}'s.

The temperature dependence of the piezoelectric strain constants can be inferred from the information above by combining Eqs. (2.5a) and (2.6):

$$d_{31} = k_{31}\sqrt{\epsilon_{33}s_{11}} \tag{2.7}$$

This results in a strong increase with temperature for d_{31} and d_{33}.

Temperature also has an important effect on long-term piezoelectric stability. At room temperature, the decay of the piezoelectric coefficients is negligible over periods of a year or more [54]. However, as the operational temperature increases above 60°C, the decay becomes more pronounced, *e.g.* about 20% for d_{33} at 80°C [53]. Relaxation mechanisms cause the constants to stabilize if the temperature is not increased further. The film can be annealed to increase the stable operational temperature range.

2.3 Applications of PVDF

PVDF is a very different piezoelectric material; characteristics such as flexibility, ruggedness, light weight, low acoustic impedance and high losses all contrast sharply with piezocrystals or ceramics. The fact that PVDF is relatively inexpensive and needs little in the way of auxiliary electronics is also very attractive.

In applications requiring large sheets of a piezoelectric material which can be bonded to a surface with varying curvature (*e.g.* certain submarine applications [64]), PVDF is obviously the best alternative. However, most choices are not that clear cut. A rule of thumb is that materials with high piezoelectric strain constants d make good actuators (large strain developed for a given field), and those with high piezoelectric stress constants g make good sensors (large field developed under a given stress). As can be seen in Table 2.4, this would imply PVDF is a poor actuator and an excellent sensor. But other factors must also be evaluated. The low permittivity of PVDF (Table 2.1) can lead to capacitive shunting problems at low frequencies. Because of its greater dielectric strength, much stronger fields can be applied to PVDF than can be applied to PZT, so piezo film transducers can achieve strains almost ten times larger than those achievable with PZT [54]. However, the compliance of PVDF may preclude the efficient transfer of energy in some cases.

The material does have its drawbacks. Because of its polymeric nature, PVDF is subject to mechanical relaxation, which leads to relatively poor electrical stability in piezoelectric systems. This can present problems for long-term measurements of weak signals. Another problem is the low operational temperature of PVDF. While the film can be exposed to highly aggressive chemical environments, relatively mild temperatures ($> 80°C$) will significantly degrade its piezoelectric activity. This is a serious problem if one is considering embedding the film to form an intelligent structure [65], as temperatures exceed 175°C for many hours in the normal graphite epoxy cure and post-cure cycles [66].

Once again, Sessler's review [54] is an excellent source for a discussion of a variety of PVDF applications. He cites sixty references, outlining the general concepts, and places the devices in four classes: audiofrequency transducers; ultrasonic and underwater transducers; electromechanical transducers; and pyroelectric and optical devices. Pennwalt has a bibliography [53] with almost ninety articles and patents on piezo devices. And, of course, many of the citations in Lang's bibliographies [15] deal with applications.

There is an extraordinarily wide range of transducers described in the literature. No attempt at a general summary will be made here; the discussion will be restricted to those applications of relevance to the sensors discussed in later chapters.

The use of PVDF as a strain gauge for composite materials has been examined [67]. The large difference between d_{31} and d_{32} was used to measure uniaxial strains. Quasi-static measurements (below 1 Hz) required a charge amplifier to eliminate the effects of the film's capacitive time constant. This amplifier was implemented with two op amps, and even they could be dispensed with for dynamic measurements. While the authors stressed the lack of elaborate signal conditioning electronics, they also found the piezo film was a good sensor for general in-plane strain measurements.

Recognizing that, in many ways, PVDF and PZT are complementary materials, there have recently been some investigations into the feasibility of making a piezoceramic-piezopolymer composite [68, 69]. A polymer composite film was made by adding PZT powder to PVDF resin. This film exhibited improved properties as reported in Table 2.5 [68]. As could be expected, this composite material does not approach the best qualities of either of its components, but it appears to offer a good intermediate material which may be attractive for matched sensor/actuator pairs. Newham *et al.* demonstrated an application of this type of film [69]. They constructed a trilaminate composite send-receive transducer for sonar applications. The three piezoelectric layers were PVDF backed by the PZT-polymer composite and then PZT ceramic. This arrangement features increasing acoustic impedance through the thickness of the stack. The transducer could be used to monitor the outgoing as well as the incoming ultra-

Table 2.5: Properties of composite piezoelectric materials and components.

Material	ϵ_R	d_{33} (pC/N)	g_{33} (mV·m/N)	k_t (%)
PVDF	9–15	10–15	70–170	10–15
PZT	1000–1500	200–400	25–35	30–45
PVDF/PZT	35–45	20–25	40–55	30–40

sonic signals, allowing one to correlate the two better. Such composite materials are in a very early stage of development, and much more work on factors such as the mix ratio needs to be done before any really practical applications can be expected. Based on the evolution of PVDF applications, commercial forms of the material will probably have to be available before many applications appear. At the moment, development is restricted to groups that have access to the equipment (and experience) needed to make these composites.

2.3.1 Deformable Mirrors

Several variable-focus mirrors have been tested using PVDF bimorphs as shape-controlling actuators. The first study [70] considered a bimorph with a single metallized face. This would serve as the actuator's electrical ground plane *and* as the optical surface. No coating was present on the other surface, allowing the application of arbitrary two-dimensional voltage distributions via charge deposition. The relationship between the Fourier coefficients of these voltage distributions and the resulting shape of the optical surface was analyzed. Two modes of operation were considered: the longitudinal effect was used to correct small amplitude, high (spatial) frequency aberrations, while the bending response of the bimorph was used for the larger amplitude, low frequency aberrations. Kokorowski noted that the required control voltages would determine the highest spatial frequency aberration that could be compensated for; actuator spacing was the determining factor for mirrors controlled by discrete PZT actuators. This is one of the advantages of using a single large sheet as an distributed actuator.

The details of how the electric charges would be deposited on the upper surface were not discussed in Ref. [70]. A somewhat different approach had to be adopted for an experimental demonstration [5]. A composite bimorph was proposed: a single layer of PVDF was bonded to a thin glass plate. A silver optical surface was added to the glass by vapor deposition. The piezo film was cut in the shape of the desired (one-dimensional) voltage distribution. Rectangular (uniform) and triangular electrodes were tested, resulting in

deformation curves of the form ax^2 and $a_1x^2 + a_2x^3$, respectively. A holographic spatial filter was used to compensate for some of the residual static distortion of the glass; this could be avoided by polishing the optical surface to provide a smoother finish. An optoelectrical feedback system, using a photodiode array to sense the wavefronts, was proposed but did not appear to have been implemented. Later models demonstrated the use of multiple film layers [71]. Two or three layers of PVDF were mounted on a single piece of glass; uniform and triangular actuators controlled the shape of a single mirror, providing a wider range of deformation curves. The piezoelectric anisotropy of PVDF prevented the implementation of a mirror with electrodes shaped in two dimensions.

2.3.2 Active Structural Control

Rather than trying to deal with an infinitude of modes, a number of researchers have looked at the advantages of using distributed sensors and actuators to control a distributed parameter system, such as a structure. Tzou has demonstrated the use of PVDF as both a sensor and an actuator [72,73]. He has also combined these transducers, using two layers of film on opposite sides of a beam to form a feedback system [74]. The associated analysis was performed on a multilayered thin shell [73], but this was reduced to a plate to allow the efficient implementation of a piezoelectric finite element model [75], while the experiments have typically been conducted with cantilever beams [73,74]. In all cases, the sensors and actuators were uniform pieces of PVDF. Reference [72] examined broadband active isolation, while Refs. [73,74] were concerned with increasing the damping in one or several modes. As will be seen, this is a common measure of performance.

In the case of deformable mirrors, the distributed nature of the actuators was used to increase the bandwidth of the system. It can also facilitate a design approach based on Lyapunov's second method [76]. Hubbard has used this extensively in his work. The early experiments consisted of a uniform PVDF actuator mounted on a cantilever beam [3]. Damping of the first mode was the performance index, although later work extended

this to the first three modes [77]. Two-dimensional structures were also controlled: four uniform PVDF actuators were mounted on a fiberglass cantilever beam with a square cross-section [78]. Note that the *structure* was two dimensional, not the actuators. Moving away from uniform transducers, the effects of a spatially-shaped distributed actuator were studied by expressing the loading distribution in terms of generalized functions. As with the deformable mirrors, uniform and triangular PVDF actuators were tested; the damping of the first three modes was taken as a performance metric [6].

Next, sensors were tackled. Using generalized functions, it was shown how certain sensor distributions could be used to sense point variables, *e.g.* a uniform PVDF distribution on a cantilever beam will sense the angular displacement at the free end [79]. This reference also discussed combining several generalized functions to provide observability of linear and angular displacements. The form of this combination would determine the weighting of the various modes; if the sensor's width were proportional to the modal strain distribution, for example, only a single mode would be sensed. Uniform and triangular PVDF sensors were demonstrated, and a feedback experiment was performed using a uniform sensor and actuator, both made of PVDF, on a cantilever beam [79]. The improvement in the damping ratios of the first two modes was used to evaluate the effectiveness of the controller. Noise reduction techniques were needed due to radiative cross-coupling of the actuator and the sensor. When the structurally-induced sensor output is low, this noise dominates the signal. A decoupling circuit was used to minimize the problem.

Miller and Hubbard [79] emphasized the advantages of using a matched sensor/actuator pair for vibration control and contended that, because they act as spatial integrators, the distributed sensors are less sensitive to placement errors than discrete sensors. On the other hand, Burke took advantage of the spatial filtering characteristics of distributed actuators for shape control [80]. He used PVDF actuators and "fotonic" sensors to form a closed-loop feedback system; shape control was demonstrated for the first four modes.

Another significant step in the use of PVDF transducers for structural control was

Lee's extension of classical composite theory to include piezoelectric laminates [4]. The structure was defined in terms of a number of laminae which could consist of any material, including PVDF. Even when the materials were mechanically isotropic, the directional nature of PVDF's piezoelectricity could result in twisting/bending coupling. Sensor and actuator equations were defined to study this effect. These equations give the sensor output for a given mechanical state and the mechanical deformation for a particular voltage distribution, respectively. At this stage, the surface electrode pattern was arbitrary. Lee experimentally demonstrated the effect of the skew angle between the structural principal axes and the PVDF lamina axes; the PVDF layers were all uniform but the stretch axis of the film (axis *1* in Fig. 2.4) was oriented at various angles with respect to the structural axes. Benders, twisters, bending-twisting coupled actuators, twist sensors and oscillators were tested, using up to four layers of PVDF for a single laminate. The results agreed well with the theory, and the film was found to be an excellent sensor, with a flat frequency response and almost no phase lag.

The same sensor and actuator equations were analysed to determine the effect of varying the electrode patterns [7]. Specific input/output characteristics could be implemented by properly designing the shape of the electrodes. In particular, Lee was able to derive *modal* sensor and actuator equations. The corresponding transducers would only interact with a single mode of the structure. To achieve this, the electrode width must be proportional to the second derivative of one of the structure's eigenfunctions (equivalent to the modal strain distribution). The modal nature of these transducers can be verified with the orthogonality relations. The electrode shaping was realized by etching the film's metallization. Modal sensors for the first two modes of a stainless steel cantilever beam were manufactured and tested. The response of the Mode One sensor to mode two excitation was 18% of the Mode Two sensor's response. The Mode Two sensor performed much better, with its mode one response being 3% of the Mode One sensor's response. These sensors demonstrated that the response of a sensor could be tuned by modifying its electrode pattern. The distributed sensor is "programmed" to

perform signal processing by means of spatial integration. In this case, the processing is modal filtering so as to obtain the generalized coordinates as a function of time.

The modal actuator equation had also been derived. A Mode One actuator was constructed and combined with a Mode One sensor on a stainless steel cantilever beam to form an active control system [81]. Cross-coupling effects were seen in this experiment, just as they had been in Ref. [79]. This time, however, the noise was eliminated by simply shielding the sensor. If the modal transducers were ideal, a single modal sensor or actuator could be paired with a regular actuator or sensor to eliminate spillover, *e.g.* some accelerometers and a modal actuator. But the manufactured transducers are not ideal; the loop transfer function revealed a slight degree of leakage, as had been observed during the sensor tests. By combining two identical modal transducers, the leakage becomes a second order effect [7]. The sensor output was passed through a current amplifier, resulting in a direct measurement of the mode one generalized velocity. A low pass filter (needed because of amplifier dynamics), a gain stage and the actuator's voltage amplifier completed the feedback loop. Velocity feedback was used to critically damp the first mode. The modal sensor/actuator pair eliminated any spillover phenomena during the control of this mode.

2.4 Sensor Manufacturing Techniques

Many of the attractions of using PVDF piezoelectric film as a transducer have been described above. But there are several crucial steps which must be mastered before full advantage can be taken of this material. The manufacturer can provide many fabrication tips, and Pennwalt's technical manual and application notes should be consulted [53, 82–86]. The importance of these manufacturing steps should not be underestimated; an otherwise fascinating sensor can be rendered almost useless by unreliable leads. It has been suggested that the slow development of PVDF applications may have been due to a lack of readily available, durable electrodes and contacts [87]. The following discussion

will assume that commercially manufactured piezo film is being used; electrodes may or may not be present. Also, it will be assumed that sensors, rather than actuators, are being made. The high voltages and currents associated with actuators necessitate some more elaborate procedures, *q.v.* Ref. [88]. The sensors are envisioned as laboratory prototypes, making an arrangement which allows one to "debug" the sensor more useful than one which is fully sealed and protected.

2.4.1 Patterned Electrodes

As with all these steps, there are many alternatives here. Rather than being fully metallized, the piezo film can be supplied without electrodes or with a single one. The desired electrode pattern could then be applied using an appropriate mask and silver ink. If applied thickly enough, this provides good electrical conductivity and is relatively flexible. However, this procedure may not be attractive if the sensors are large; it may be easier to remove portions of the provided uniform electrode.

If the desired pattern is fairly regular, the easiest way to remove the unwanted regions of the electrode is to simply cut the film. The triangular sensors and actuators mentioned above were obtained this way [5,6,79]. The piezo film with vacuum deposited electrodes can be cut very cleanly with a sharp razor blade. However, if this is tried with the silk screened electrodes, one must be careful of not shorting the two surfaces; the silver ink is thick enough and of a consistency such that it tends to fragment when cut. The resulting flakes attach themselves to the freshly cut edge, forming an electrical short between the two electrodes. The cut film should be examined under a magnifying glass and any suspect regions can be scraped, but a less tedious alternative is to clean the edges with a toluene-soaked cotton swab [89]. This will dissolve any fragments of silver ink. It may affect the electrodes somewhat but these edge effects can be minimized with practice.

A potential drawback of cutting the electrodes is that the film's shape is no longer uniform. This will not affect the piezoelectric properties, but it may affect the dynamic

properties of the structure to which it is mounted. This problem can be lessened by removing nothing more than regions of the metallization by using various etching techniques. As charge is only collected in regions with electrodes on both sides of the film, etching need only be done on one surface. Of course, a lot of PVDF is "wasted," in that it is not being used as a piezoelectric. Lee used etching to shape his modal sensors [7]. Once again, the details depend on the electrode type.

The vacuum deposited metallization is so thin that it can be removed quickly with standard printed-circuit-board etchant materials. Ferric chloride solution was used successfully with nickel-copper alloy and nickel-aluminum electrodes. The desired electrode pattern must first be masked. Lee created a screen by photocopying the desired pattern onto a transparency and transferred it to the film with a negative acting photo resist [89]. During some experimental work for the SIRPNT active isolation mount [90], Huntington found an effective mask could be created with enamel spray paint and a positive mask, *i.e.* one which covers the metallized areas which are to be removed [91]. The mask was then removed, and he immersed the film in a warm (50°C) ferric chloride bath. The paint was later removed with paint thinner. A simpler technique was attempted at M.I.T. during the experiments described in Chapter 4.

The bath was found to be unnecessary with the electrodes tested here (nickel and copper, whereas Huntington's had been aluminum). Satisfactory results were obtained by making a negative mask from a sheet of adhesive-backed Mylar. This was attached to the film, taking particular pains to ensure the edges of the Mylar were well bonded to the film. A paper towel was slightly dampened with the etchant and was used to "wipe away" the exposed metal. This was followed by another towel which was soaked with water; this neutralized any remaining etchant. Large areas of film could be treated relatively quickly in this manner. A final alternative consisted of using the resist ink pen provided in the etching kit to cover small areas or the border of an electrode pattern. A cotton swab or a small paint brush was then used to apply the ferric chloride. This provided somewhat more control over where the etchant was going. Water neutralized

the etchant, and isopropyl alcohol removed the resist ink. The film should then be cleaned with an electronics cleaning fluid. Note that vinyl or nylon gloves should *always* be worn when handling the film; oily fingerprints can result in local oxidation and the associated changes in electrical properties [53].

While it was not attempted, it is believed that the same procedure would work for silver ink electrodes if toluene was used as an etchant rather than ferric chloride. With either electrode type, the pattern should include regions for lead attachment. It is also a good idea to surround all electrode regions with unmetallized borders, especially at the edges of the film. This will reduce the risk of a short circuit occurring. If, for some unknown reason, one were concerned about the different dynamic behavior of the region no longer constrained by the electrode, one could use thin unmetallized stripes to separate the electrode region which is used for the sensor from the region which is retained merely for constraint purposes. Chemical etchants could be used to create these tracks, but arcing is also an alternative: one terminal of a 9 V battery is connected to one electrode and the other terminal is brought to a conductive point, *e.g.* a piece of wire, which is used to trace the desired pattern on the other electrode. The current is usually great enough to cause arcing at the point contact, vaporizing the vacuum-deposited metallization [85].

A final point with regards to electrode shaping: one must take note of any markings on the film. The manufacturer often marks one side to indicate the polarity and stretch direction; it is all too easy to remove these markings in the course of etching, or they may be cut off. The stretch axis can often be determined by examining the surface finish, particularly with vacuum deposited metallizations. If one has lost track of the film's polarity, the pyroelectric effect can be used to determine it very easily, provided a quick electrical connection can be made [86]. Breathing on the film will generate a positive voltage, *i.e.* the positive poling electrode will be at a higher potential than the negative poling electrode. A voltmeter reading will show whether the positive lead has been connected to the positive face of the piezo film.

2.4.2 Lead Attachment

This is one of the most difficult (and frustrating) aspects of making good PVDF transducers. A soldering iron is a most effective tool if one wishes to melt holes in the film. A somewhat different approach is needed to make an electrical connection to the electrodes. Pennwalt provides a number of pre-shaped elements with leads already attached to them, but this is of little help to the custom transducer manufacturer; their application notes are much more useful, especially No. 20 [85].

Penetrative methods provide good strain relief and a high degree of electrical consistency because of the well defined contact area. Offset lead-outs must be used to prevent shorting: the electrode is shaped such that the conductive tracks of the upper and lower surfaces do not overlap near the penetration region. Blind rivets, miniature nuts and bolts or crimp connectors can then be attached. These terminations are bulky compared to the film itself; when mounted directly on a structure, they can cause mass loading or add high frequency resonances to the system. The electrode patterns can be designed to incorporate PVDF leads, allowing remote connections.

Various contact techniques are also available. Copper tape backed with a conductive adhesive (3M #1181 tape, for example) makes connections simple, but the tape does not have good long-term properties. The adhesive tends to lose its tack, reducing or even eliminating the electrical connection more quickly than the mechanical one. There is also a risk of shorting the two electrodes if unmetallized borders have not been created; the pressure applied to ensure a good bond can cause the adhesive to flow across the film's edge. If stressed, the tape appears to be susceptible to micro-cracking. This type of connection is improved by using conductive epoxy (Tra-Con Tra-Duct BA-2902). Wires can be epoxied directly to the sensor, but it is a better idea to provide a stronger connection by soldering the wires to copper contact pads, which can be made from copper tape or shim stock. Because copper is also an excellent thermal conductor, this soldering should be done *before* the contact pads are epoxied to the film. The epoxy must be given enough time to cure before being used. The pads can be placed on the

piezoelectrically active region of the sensor (certainly a good idea with actuators), but a more flexible arrangement is to use conductive tracks to connect the active region with a contact point. The size and location of this point can be chosen to facilitate a good connection rather than being restricted by the sensor's design. If these tracks were not included in the electrode pattern, they can be added with silver ink.

Most of these connections are best made after the sensor is attached to the structure, but it is important to consider them beforehand; electrical connections must be made with both of the film's electrodes. The leads are not only for electronics interfacing, as the attached leads can be used to make a multi-segment sensor. It is then important that all the electrodes are wired together properly.

2.4.3 Bonding

The bond between the structure and the sensor must be such that the structure's surface strains are smoothly transferred to the entire active region of the piezo film. The thickness and stiffness of the adhesive layer are two very important characteristics. Convenience should also be considered when handling large pieces of film. As the bond tends to be rather permanent, one should check the orientation and polarity of a sensor before starting to mount it.

The most common adhesive is some form of epoxy. A wide range is available; Ref. [84] has suggestions for various combinations of surfaces, and addresses of the suppliers are provided. A five-minute epoxy (*e.g.* Devcon) results in a strong bond without a long cure. If an epoxy requires a long cure, the bonding process can be accelerated by applying some heat, but the temperature must be carefully controlled to avoid weakening the piezoelectricity of the film. A thin adhesive layer can be obtained by applying the epoxy resin to the structure and the hardener to the sensor. Both surfaces are then wiped, leaving a thin residue. Pressure should be applied, and any air bubbles should be squeezed out. Toda and Osaka claimed to be able to obtain bonds about 0.3 microns thick with this technique [92].

Rather than using a regular epoxy, conductive epoxies are useful if the structure itself is conductive. As these epoxies are expensive, and somewhat unreliable as bonding agents, a good practice is to use several drops of conductive epoxy to establish the electrical connection and then use regular epoxy to secure the rest of the sensor to the structure. The structure can be used as an electrical ground, with a connection established wherever practical. This makes it easier to establish a common ground for all equipment associated with an experiment.

If multiple layers of piezo film are to be applied, some form of insulation will be required between the layers, unless adjacent electrode pairs are supposed to be at the same potential, as in multimorph designs. A thin layer of epoxy is not a reliable insulator. Epoxy-soaked fiberglass was found to be a good insulator, but the thickness (~ 0.4 mm) was a problem and the stiffness gradient across the sensor layers disrupted the transfer of strain at high frequencies [93]. A less intrusive insulating layer was made with Mylar. This is available as thin as 25 microns, and some forms already have an acrylic adhesive applied to both sides. If this cannot be found, acrylic spray adhesive (3M #77 Super Spray) or epoxy can be used to coat the Mylar. By only exposing one adhesive layer at a time, this insulation was quite easy to work with, and it has mechanical properties that are quite similar to PVDF's. If the structure were not being used as a ground, and one wished to insulate the sensor from it, a layer of Mylar could be placed between the sensor and the structure.

The spray adhesive can also be used to bond the sensor to the structure. The adhesive can be applied much more quickly than epoxy, the whole process is much cleaner and sensor placement is somewhat easier. But the bond is weaker, and not as uniform as with epoxy. The adhesive is more tacky, making it difficult to remove small bubbles, although the sensor can be removed during the first few minutes and placement attempted again. On the whole, the extra time and effort associated with using epoxy is worthwhile.

2.4.4 Electronic Interfaces

When using piezoelectrics, the electrical boundary conditions are just as important as the mechanical ones. So the circuit used with the sensor will affect how the sensor operates. Complicated electronics are not required to produce useful signals, but some thought must be given to the electronics to ensure the sensor is acting as desired.

An equivalent circuit for piezoelectric film is shown in Fig. 2.5a. The induced charge Q is linearly proportional to the applied strain, and the capacitance C_f is proportional to the electrode's surface area and inversely proportional to the film thickness. PVDF has a very high volume resistivity ($1.5 \times 10^{13}\,\Omega \cdot \mathrm{m}$), so the film's internal resistance R_f can usually be ignored [53]. The simplified Thévenin equivalent circuit is shown in Fig. 2.5b.

The input resistance R_i and capacitance C_i of the electronics interface should be known. The effect of this load can then be determined. The open circuit output voltage will be given by $V_o = Q/(C_f + C_i)$, and the circuit will have a time constant of $\tau = R_i(C_f + C_i)$. The corresponding corner frequency f_c should lie below the frequency range of interest; this will determine the minimum input impedance of the electronics interface.

The film can be used in either "short circuit" or "open circuit" mode. A high input impedance interface will result in the open circuit mode. If the measurement device

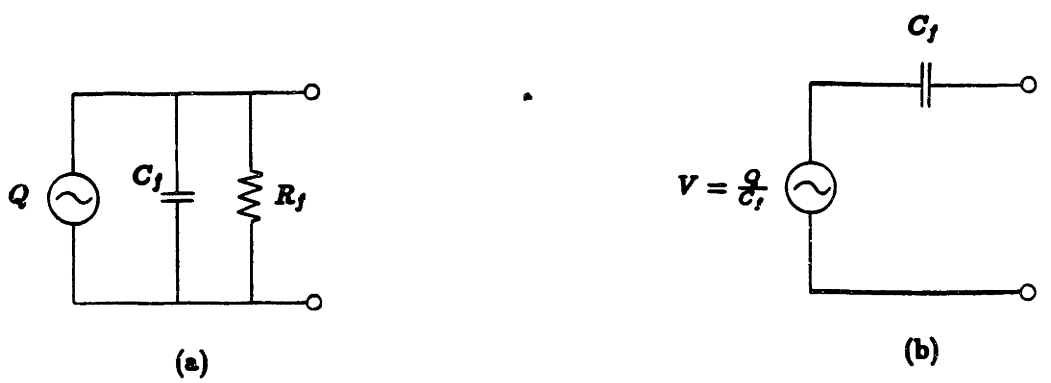

Figure 2.5: PVDF film's equivalent circuits. (a) Charge mode; (b) Voltage mode.

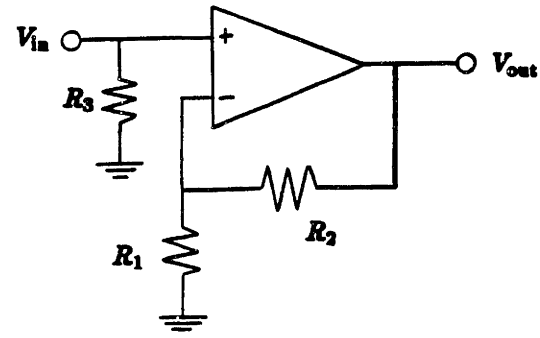

Figure 2.6: Buffer amplifier.

does not have a high enough impedance, a buffer amplifier (Fig. 2.6) can used to lower f_c [94]. The input impedance is R_3 and the gain is $1 + R_2/R_1$. The alternative, the short circuit mode, is recommended for small signals and uses a charge amplifier to eliminate the effects of the film's time constant by absorbing all the charge developed on the electrodes; there is no voltage generated across the film. This mode measures the current $I = dQ/dt$. A charge amplifier [83] can be used to integrate this signal, producing an output voltage $V_o = Q/C_2$ with a time constant $\tau = R_2C_2$ (Fig. 2.7). This circuit allows the designer to choose the corner frequency, but it is susceptible to noise, so guarded inputs grounded to the op amp's casing are recommended [83]. It has been found that 3140 FET op amps work well for these circuits.

More extensive shielding may be required. This will depend on the electromagnetic environment the sensor is operating in; several studies have reported cross-coupling

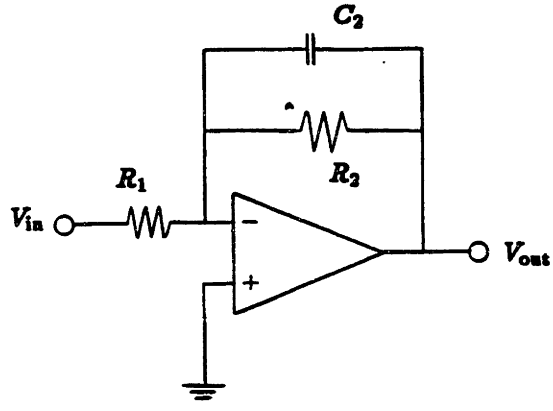

Figure 2.7: Charge amplifier.

when using PVDF sensors with actuators operated with voltages of several hundred volts [79,81]. As noted by Lee *et al.*, good shielding can eliminate this. Metallized film can be used to shield the transducer by folding a piece of PVDF in half or by laminating two pieces together [82]. Folding should be restricted to film with silver ink electrodes; this shielding method has the advantage that the "two" ground electrodes are already connected. In any case, the ground should be larger than the internal "hot" electrodes so as to completely enclose them. If the electrodes are to be shaped, care must be taken to align the patterns properly; this has been done with a modal sensor [81].

Obviously, more sophisticated electronic interfaces can also be combined with PVDF film to produce useful devices. Switches, counters and level detectors are but a few examples [53]. However, the simple circuitry presented above sufficed for sensing structural vibration.

Chapter 3

Modal Sensors

The previous chapter described the piezoelectric polymer polyvinylidene fluoride (PVDF) and some of the ways that useful transducers can be fabricated from this material. The sensor designer has a great deal of control over the piezoelectricity of the film, allowing sensors with special characteristics to be created. Modal sensors are a good example of such tailoring.

Some of the schemes used to implement modal control will be reviewed in this chapter. The modal sensor equation will be developed in general and then for a specific structure. The modal sensors described here consist of a layer of piezoelectric film. This produces a charge when strained, and the charge is proportional to the strain integrated over the surface of the film. In the case of one-dimensional structures, the width of the film can be thought of as a strain weighting factor that varies along the length of the structure. Modal sensors are generated by selecting specific distributions for this weighting function, *i.e.* by shaping the width of the film proportional to the strain mode shape. Four modal sensors were fabricated to verify the modal sensor equation, and experimental results from these piezo sensors will be discussed.

3.1 Observers, Filters and Sensors

Structural flexibility has become an important issue when designing control systems for modern spacecraft or robotic manipulators. To achieve future mission objectives, broadband control of structural flexibility may be required. But many of the structural elements in which in which the flexibility is an important consideration for control design can be well characterized by a manageable number of modes. Some examples are solar arrays, instrumentation booms and flexible robotic links. This leads to the concept of modal control, whereby one attempts to control the motion of any point of the structure by controlling a reasonably small number of the lower modes of vibration [95]. Direct feedback can be used with modal control if the modal displacements and velocities are known. But that can pose somewhat of a problem, as most sensors do not measure the modal states. There are several ways to obtain these states from conventional measurements.

Observers are a standard modern control technique for this type of problem. A wide variety are available; the Luenberger observer is one which is applicable to a general dynamic system and can be used to extract the modal states [106, 107]. An observer takes the measurements of several physical states and calculates the corresponding modal states based on a model of the system. The more detailed this model, the better the estimates of the modal states will be. Important modelling information can include general properties like orthogonality and specifics like nonlinearities. Of course, more detail will result in a more computationally intensive observer, so one must trade off speed and accuracy. As Luenberger observers do not make use of the mode's orthogonality, unmodelled modes can contaminate the estimates of the modal states; this observation spillover is capable of causing instability [96].

The modal displacements and velocities can be thought of as the structure's response at its natural frequencies. So an intuitively obvious way of obtaining these states is temporal filtering. Balas has proposed the use of comb filters: each tooth is a narrow

bandpass filter designed to comb out a particular mode [96]. Phase-locked loops are used to handle slight modelling errors. This approach is difficult to implement if the structure is modally dense, as high order filters must be used due to the narrow frequency bands between modes.

Modal filters are a more computationally efficient method of extracting these states. These are spatial, rather than temporal, filters. As spatial integration is a smoothing operation, the problem of observation spillover leading to instability is reduced [97]. The modal expansion theorem states

$$q_i(t) = \int_D M(P)\phi_i(P)w(P,t)\,dD \tag{3.1a}$$

$$\dot{q}_i(t) = \int_D M(P)\phi_i(P)\dot{w}(P,t)\,dD \tag{3.1b}$$

where M is a mass operator and ϕ_i is an eigenfunction of the system. As the integration is carried out over the entire domain D of the structure, the displacement w and velocity $\dot{w}$ of every point P must be known in order to calculate the modal states q_i and $\dot{q}_i$. If distributed measurements are not available, modal filters can be implemented with discrete sensors by using interpolation functions, as in the finite element method [8]. The discrete sensor measurements are interpolated to yield a displacement profile, which is then spatially integrated to determine the modal states. The sensor measurements are functions of time, not space, so they can be taken outside the spatial integral. The interpolation functions depend on the type of sensors being used, the system model and the position of the sensors, but not on the temporal signals of the sensors, *i.e.* the interpolation functions are not a function of time, so they need only be integrated once. This can be done offline, reducing the real-time processing to a summation of weighted sensor measurements.

An attractive option is the use of a spatially distributed piezoelectric sensor. Then the material itself performs the spatial integration, and, as there is now only one sensor per modal state, no summing is required; modal sensors measure modal coordinates directly [7]. The sensor's electrodes must actually be shaped so as to reflect the strain

mode shape. This results in the drawback that modal sensors cannot be "reprogrammed" easily to account for changes in the mode shapes or to sense other modes. However, Lee proposed an online modal coordinate analyzer [89] using spatial multiplexing to allow a single layer of film to sense several modes: a number of electrically isolated electrode segments are created, and various combinations of the outputs will give the modal states for different modes. The logical extension of this idea is to cover the structure with an array of PVDF point sensors and sum the outputs, weighing them differently to sense different modes, but that is just a step back to modal filters with many discrete sensors.

Just as the bandwidth of temporal filters using discretely sampled measurements is restricted by aliasing considerations, modal filters using discrete sensors are affected by spatial aliasing. Interpolation functions cannot be used to account for modes with wavelengths smaller than the sensor spacing, so the averaging effect of spatially integrating these functions does not help to cancel these high (spatial) frequency signals. If the modal filters were truly orthogonal in space, this would not be a problem. But, for example, at high frequencies beams can no longer be modelled as Bernoulli-Euler beams; advanced models, such as the Timoshenko beam [108, 109], must be adopted. These beam models have different modes which are not necessarily orthogonal to the Bernoulli-Euler modes. On the other hand, modal *sensors* are continuously distributed, so spatial aliasing does not affect them. There is still the possibility that the high frequency modes are not orthogonal to the sensor's mode, but the spatial integration will now capture these high frequency modes, smoothing them and greatly reducing their contribution to the sensor's response. This makes modal sensors more robust than modal filters.

Modal sensors have been demonstrated by work discussed in the previous chapter [7, 81, 93]. These studies have tested PVDF sensors on cantilever beams; the research described in this chapter sought to demonstrate modal sensors on a structure with more complicated dynamic behavior. The Martin Marietta Large Space Manipulator (LSM) testbed was selected as a sample structure. Modal sensors were designed for the LSM

and then were tested in it, comparing the results with a similar test conducted with strain gauges. The LSM itself consists of a 1.8 m horizontal planar arm formed by two aluminum links with rectangular cross-sections. Shoulder and elbow actuators are used to drive the manipulator, while elbow and tip airpads support the links and the payload. These can be changed, permitting manipulators with a wide variety of dynamic properties to be tested. A more complete description of the LSM and the associated sensors and electronics is given in Ref. [98].

3.2 The Sensor Equation and Modal Decomposition

Lee derived an equation relating the charge generated by a piezoelectric lamina to the mechanical deformation of a two-dimensional structure—this is the sensor equation [4]. The generality of this equation was reduced by assuming: the lamina is made of PVDF and is mechanically isotropic; the material axes of this lamina are aligned with the principal axes of the structure; the structure has constant properties along its length and is slender enough to neglect the deformation variations across its width.

The sensor output is a function of the effective electrode width $\mathcal{F}(x)$, which includes the physical width of the electrode and the polarization of the film, making negative widths possible. To define $\mathcal{F}(x)$ for an arbitrary sensor shape, let $F(x,y)$ denote the spatial pattern of the electrode (1 or 0, depending on whether the point (x,y) is covered by an electrode or not). Let $P(x,y)$ be the polarization profile of the piezopolymer. Allowing any orientation of the poling axis, P is the dot product of the film's poling axis (the 3 axis) and the axis of mechanical deformation (the z axis)

$$P(x,y) = \mathbf{p}_z \cdot \mathbf{p}_3(x,y) \tag{3.2}$$

where $\mathbf{p}_i$ is the unit normal aligned with axis i. But we have assumed the piezo film's axes are aligned with the principal structural axes, and we know that commercial PVDF

is always poled through the thickness, so P indicates whether the poling axis has the same sign as the deformation axis, *i.e.* P will be ± 1 for poled PVDF. In Eq. (3.2), notice that p_3 can vary from point to point on the film. Integrating the product of F and P across the width of the beam b, the effective electrode width is

$$\mathcal{F}(x) = \int_{-b/2}^{b/2} F(x,y)P(x,y)\,dy \tag{3.3}$$

If the PVDF lamina has a single continuous electrode on each side and is of uniform polarity, Eq. (3.3) reduces to $\mathcal{F}(x) = \pm b_{pz}(x)$, where b_{pz} is the width of the piezoelectric film's electrode.

Having defined the effective electrode width $\mathcal{F}(x)$, the sensor equation for a PVDF sensor on a uniform beam can be expressed using the piezoelectric e coefficient, which is the ratio of the charge per unit electrode area to the mechanical strain. The strain in the x direction is determined by multiplying the moment-curvature relation for a symmetric beam subjected to pure bending by the moment arm z [99]

$$\epsilon(x,t) = -\frac{\partial^2 w(x,t)}{\partial x^2} z \tag{3.4}$$

where z is the distance from the beam's neutral axis to the lamina's midplane. Then, the effective electrode width is integrated along the length of the sensor to obtain the electrode area, resulting in the sensor equation

$$Q(t) = -e_{31} z \int_0^l \mathcal{F}(x) \frac{\partial^2 w(x,t)}{\partial x^2}\,dx \tag{3.5}$$

where $Q(t)$ is the charge generated by the PVDF lamina, l is the sensor's length and $w(x,t)$ is the transverse displacement of the beam. The piezoelectric field intensity constant e_{31} can be expressed in terms of the piezoelectric strain coefficients by using Eq. (2.5c):

$$e_{31} = (d_{31} + \nu_{pz} d_{32}) \frac{E_{pz}}{1 - \nu_{pz}^2} \tag{3.6}$$

where the subscript pz indicates a property of the piezoelectric lamina.

The transverse deformations $w(x,t)$ can be decomposed into an infinite series of time-dependent generalized coordinates multiplied by spatial basis functions. The basis

functions can be, for example, the solutions of the associated eigenvalue problem, *i.e.* the eigenfunctions. Then, separating the temporal and spatial dependence of w, the modal expansion is

$$w(x,t) = \sum_{i=1}^{\infty} \phi_i(x) q_i(t) \tag{3.7}$$

where $\phi_i(x)$ are the eigenfunctions and $q_i(t)$ are the generalized coordinates.

The general eigenproblem can be written

$$L[w] = \lambda M[w] \tag{3.8}$$

where L and M are linear homogeneous differential operators. Assume the system is self-adjoint, *i.e.*

$$\int_D u L[v]\, dD = \int_D v L[u]\, dD \tag{3.9a}$$

$$\int_D u M[v]\, dD = \int_D v M[u]\, dD \tag{3.9b}$$

Let λ_i and λ_j be two distinct eigenvalues and ϕ_i and ϕ_j be the corresponding eigenfunctions. Then the generalized orthogonality conditions [100] are

$$\int_D \phi_i L[\phi_j]\, dD = 0 \tag{3.10a}$$

$$\int_D \phi_i M[\phi_j]\, dD = 0 \tag{3.10b}$$

for $\lambda_i \neq \lambda_j$. If the eigenfunctions are normalized with respect to M,

$$\int_D \phi_i M[\phi_i]\, dD = 1 \quad \text{for all } i, \tag{3.11}$$

the eigenfunctions are called normal modes, and Eqs. (3.10b) and (3.11) can be written

$$\int_D \phi_i M[\phi_j]\, dD = \delta_{ij} \tag{3.12}$$

where δ_{ij} is the Kronecker delta.

In the case of a uniform single-span beam, using the method of separation of variables, Eq. (3.7), to convert partial derivatives to ordinary derivatives, the operators are

$$L[\phi(x)] = EI \frac{d^4\phi(x)}{dx^4} \tag{3.13a}$$

$$M[\phi(x)] = \omega^2 \rho \phi(x) \tag{3.13b}$$

These operators are substituted into the orthogonality conditions, Eqs. (3.10), and integration by parts is carried out. The boundary terms vanish for a wide range of boundary conditions [101], so for normal modes, Eq. (3.10a) becomes

$$EI \int_0^L \frac{d^2\phi_i}{dx^2} \frac{d^2\phi_j}{dx^2} dx = \omega_i^2 \delta_{ij} \tag{3.14}$$

where L is the length of the beam.

The eigenfunctions need not be mass normalized. For example, Blevins [101] describes the mode shapes of a uniform cantilever beam as

$$\phi_i(x) = \left(\cosh \lambda_i \frac{x}{L} - \cos \lambda_i \frac{x}{L}\right) - \sigma_i \left(\sinh \lambda_i \frac{x}{L} = \sin \lambda_i \frac{x}{L}\right) \tag{3.15}$$

where λ_i is a solution of the transcendental equation

$$\cos \lambda \cosh \lambda + 1 = 0 \tag{3.16}$$

and the weighting factor σ_i is given by

$$\sigma_i = \frac{\sinh \lambda_i - \sin \lambda_i}{\cosh \lambda_i + \cos \lambda_i} \tag{3.17}$$

These mode shapes result in a modified orthogonality condition:

$$\int_0^L \frac{d^2\phi_i}{dx^2} \frac{d^2\phi_j}{dx^2} dx = \frac{\lambda_i^4}{L^3} \delta_{ij} \tag{3.18}$$

Of course, Eqs. (3.15–3.18) will vary with the boundary conditions.

Either of these orthogonality conditions can be exploited to design a modal sensor. If a PVDF sensor covers the length of the beam, *i.e.* $l = L$, and its effective electrode width $\mathcal{F}(x)$ is proportional to the second derivative of one of the displacement eigenfunctions $\phi_i(x)$, then the charge developed by the sensor $Q(t)$ will be proportional to the corresponding generalized coordinate $q_i(t)$. To see this, substitute the modal expansion, Eq. (3.7), into the sensor equation, Eq. (3.5). Let the effective electrode width be

$$\mathcal{F}(x) = \alpha_i \frac{d^2\phi_i(x)}{dx^2} \tag{3.19}$$

where α_i is a scaling constant. The sensor equation will have the form of an orthogonality condition, Eq. (3.18), so the summation of terms in the modal expansion can be eliminated, leaving the modal sensor equation:

$$Q(t) = -e_{31} z \alpha_i \frac{\lambda_i^4}{L^3} q_i(t) \tag{3.20}$$

As desired, the modal sensor measures one of the generalized coordinates. Measurements with a high input impedance device provide direct access to modal displacements, while modal velocities are given by measurements with a low input impedance device (see Section 2.4.4).

It should be noted that the eigenfunction used to determine the shape of the modal sensor need not be a solution of the structure's eigenproblem. This might be a deliberate choice, or it might arise because of modelling errors. Assume the sensor is shaped such that

$$\mathcal{F}(x) = \alpha_i \frac{d^2 \hat{\phi}_i(x)}{dx^2} \tag{3.21}$$

while the structure's eigenfunctions remain ϕ_j. The orthogonality relation can no longer be used, so the modal sensor equation is given by

$$Q(t) = -e_{31} z \alpha_i \sum_{j=1}^{\infty} q_j(t) \int_0^L \frac{d^2 \hat{\phi}_i}{dx^2} \frac{d^2 \phi_j}{dx^2} \, dx \tag{3.22}$$

If both $\hat{\phi}_i$ and ϕ_j are known, Eq. (3.22) can be used to construct modal filters for a finite number of modes: a matrix of modal gains is assembled and inverted. Rather than being diagonal, as was the case when $\hat{\phi}_i = \phi_j$, the gain matrix will be fully populated, but all terms, including the off-diagonal ones, can be computed with Eq. (3.22). Of course, it is still possible to select sensors that are orthogonal to one another:

$$\int_0^L \frac{d^2 \hat{\phi}_i}{dx^2} \frac{d^2 \hat{\phi}_j}{dx^2} \, dx = 0 \quad \text{for } i \neq j. \tag{3.23}$$

Orthogonal measurements represent the least duplication of effort, in that each measurement is independent of the others. It also helps make any numerical processing of the signals more robust by keeping matrices well-conditioned [102]. It may be possible

to create standard modal sensors for a particular class of structures, as in component mode synthesis [103], and then use Eq. (3.22) to correct for differences between the assumed mode shapes and the structure's eigenfunctions; this idea and the associated error analysis require further research.

3.3 Manipulator Link Modal Sensors

The LSM at Martin Marietta provided an excellent opportunity to test modal sensors on a more complicated structure. The links can be replaced, making it easy to influence the dynamic properties of the manipulator. It also meant that all of the sensors to be tested (strain gauges and several modal sensors) did not have to be mounted on a single link. Tests had already been conducted on a rigid-elastic arm using strain gauges placed at the strain nodes of some of the lower modes [104]. This was a reasonable approach as there were only three modes below 50 Hz, and they dominated the response.

At M.I.T., four modal sensors were designed for the LSM. The objective was to measure the modal coordinates of the link during certain maneuvers. Some preliminary tests were conducted on the sensors before they were delivered to Martin Marietta, where their ability to measure the modal coordinates was compared to the performance of strain gauges mounted so as to minimize the contribution from some of the other modes.

3.3.1 Basis Function Selection

The modal sensors can be shaped once a set of basis functions is chosen. Due to the rigid-elastic nature of this LSM configuration (Fig. 3.1), the eigenfunctions used were those of the outer link with the inner link locked (shoulder actuator clamped, elbow airpad deflated, leaving elbow actuator free to rotate). The outer link was modelled as a pinned-free Bernoulli-Euler beam with a root inertia and a tip mass and inertia (Fig. 3.2). The mass and inertias represented the payload and the rigid elbow rotor.

elastic beam's point of attachment, m_t is the mass of the rigid payload mounted at the tip of the beam, I_t is the payload's moment of inertia about its attachment point and a_t is the distance from this point to the payload's center of mass. These parameters can be nondimensionalized against the beam's mass $M = \rho L$

$$\ell_e = \frac{a_e}{L} \tag{3.26a}$$

$$k_e = \frac{I_e}{ML^2} \tag{3.26b}$$

$$\mu_t = \frac{m_t}{M} \tag{3.26c}$$

$$\ell_t = \frac{a_t}{L} \tag{3.26d}$$

$$k_t = \frac{I_t}{ML^2} \tag{3.26e}$$

To solve for the basis functions, we make use of separation of variables in Eq. (3.24) assuming harmonic vibrations

$$w(x,t) = \sum_{i=0}^{\infty} \phi(x) q_i \cos \omega_i t \tag{3.27}$$

The eigenproblem is then

$$EI\,\phi''''(x) = \omega^2 \rho \phi(x) \tag{3.28}$$

where $()'$ indicates differentiation with respect to x. The general solution of this equation is

$$\phi(x) = A_1 \cos \lambda \frac{x}{L} + A_2 \cosh \lambda \frac{x}{L} + A_3 \sin \lambda \frac{x}{L} + A_4 \sinh \lambda \frac{x}{L} \tag{3.29}$$

where

$$\lambda = L \left(\frac{\rho \omega^2}{EI} \right)^{\frac{1}{4}}$$

By substituting Eq. (3.27) into the boundary conditions, Eqs. (3.25), we can derive a system of equations for the coefficients A_i

$$\begin{bmatrix} 1 & 1 & -\lambda \ell_e & -\lambda \ell_e \\ -1 & 1 & \lambda(\ell_e + k_e \lambda^2) & \lambda(-\ell_e + k_e \lambda^2) \\ \beta_1 & \beta_2 & \beta_3 & \beta_4 \\ \beta_5 & \beta_6 & \beta_7 & \beta_8 \end{bmatrix} \begin{bmatrix} A_1 \\ A_2 \\ A_3 \\ A_4 \end{bmatrix} = \begin{bmatrix} 0 \\ 0 \\ 0 \\ 0 \end{bmatrix} \tag{3.30}$$

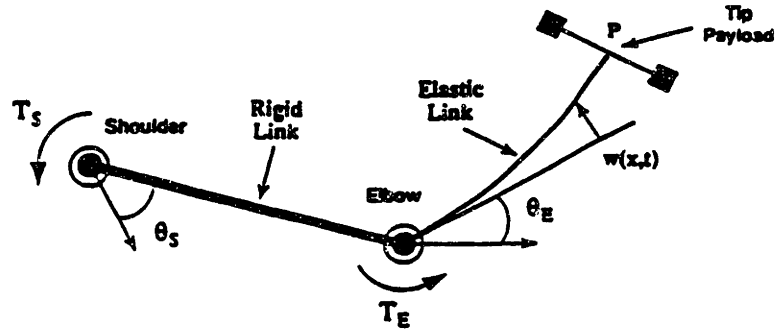

Figure 3.1: Planar rigid-elastic arm.

The pinned root was considered to be fixed in inertial space.

The partial differential equation for a Bernoulli-Euler beam is

$$EI\frac{\partial^4 w(x,t)}{\partial x^4} + \rho\frac{\partial^2 w(x,t)}{\partial t^2} = 0 \tag{3.24}$$

where EI is the beam's flexural rigidity and ρ is the mass per unit length. In the absence of external torques or forces, the boundary conditions, as derived using forces balances or Hamilton's principle, are

$$w(0,t) = a_e\frac{\partial w(0,t)}{\partial x} \tag{3.25a}$$

$$EI\frac{\partial^2 w(0,t)}{\partial x^2} = I_e\frac{\partial^3 w(0,t)}{\partial t^2 \partial x} + a_e EI\frac{\partial^3 w(0,t)}{\partial x^3} \tag{3.25b}$$

$$EI\frac{\partial^3 w(L,t)}{\partial x^3} = m_t\frac{\partial^2 w(L,t)}{\partial t^2} + m_t a_t\frac{\partial^3 w(L,t)}{\partial t^2 \partial x} \tag{3.25c}$$

$$-EI\frac{\partial^2 w(L,t)}{\partial x^2} = I_t\frac{\partial^3 w(L,t)}{\partial t^2 \partial x} + m_t a_t\frac{\partial^2 w(L,t)}{\partial t^2} \tag{3.25d}$$

The subscripts e and t represent elbow and tip, respectively. So I_e is the moment of inertia of the elbow rotor about the rotation axis, a_e is the distance from this axis to the

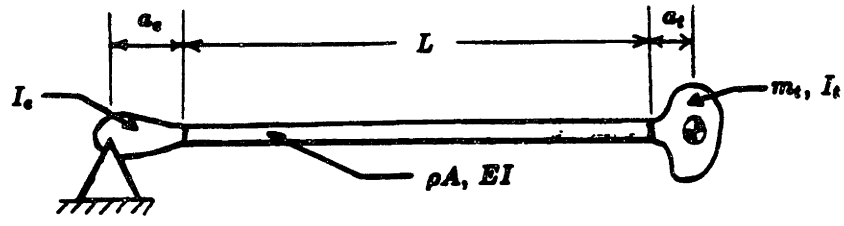

Figure 3.2: Model of outer link and payload.

where

$$\begin{aligned}
\beta_1 &= \sin\lambda + \lambda\mu_t(\cos\lambda - \lambda\ell_t\sin\lambda) \\
\beta_2 &= \sinh\lambda + \lambda\mu_t(\cosh\lambda + \lambda\ell_t\sinh\lambda) \\
\beta_3 &= -\cos\lambda + \lambda\mu_t(\sin\lambda + \lambda\ell_t\cos\lambda) \\
\beta_4 &= \cosh\lambda + \lambda\mu_t(\sinh\lambda + \lambda\ell_t\cosh\lambda) \\
\beta_5 &= \cos\lambda + \lambda^2(\mu_t\ell_t\cos\lambda - \lambda k_t\sin\lambda) \\
\beta_6 &= -\cosh\lambda + \lambda^2(\mu_t\ell_t\cosh\lambda + \lambda k_t\sinh\lambda) \\
\beta_7 &= \sin\lambda + \lambda^2(\mu_t\ell_t\sin\lambda + \lambda k_t\cos\lambda) \\
\beta_8 &= -\sinh\lambda + \lambda^2(\mu_t\ell_t\sinh\lambda + \lambda k_t\cosh\lambda)
\end{aligned}$$

The nontrivial solution is found by setting the determinant of the matrix to zero. This produces a transcendental equation in λ.

An eight-element finite element model of the beam and endbodies was constructed using numerical values from Martin Marietta's characterization [104]. This model was used to provide estimates of the first three natural frequencies of the beam. These estimates were used as initial guesses in a root-finding routine based on the Van Wijngaarden-Dekker-Brent method [105]. The routine called a MATRIXx function which evaluated the transcendental equation in λ. Once the numerical values of λ_i for $i = 1, 2, 3$ had been determined to the desired tolerance ($\Delta f_i/f_i \leq 10^{-6}$), the eigenfunctions ϕ_i could be found. Rather than mass normalizing the eigenfunctions, the corresponding second derivatives were evaluated:

$$\phi_i''(x) = \left(\frac{\lambda_i}{L}\right)^2\left(-A_1\cos\lambda_i\frac{x}{L} + A_2\cosh\lambda_i\frac{x}{L} - A_3\sin\lambda_i\frac{x}{L} + A_4\sinh\lambda_i\frac{x}{L}\right) \qquad (3.31)$$

and the maximum value of $\phi_i''(x)$ along the length of the beam, $(\phi_i'')_{max}$, was found. The sensor had to be narrower than the beam, so a width of $b_{pz} < b$ was used. The normalization factor was then

$$\alpha_i = b_{pz}/(\phi_i'')_{max} \qquad (3.32)$$

The electrode shape required to produce a modal sensor for this beam was given by Eq. (3.19).

3.3.2 Test Article Description

The modal sensors were to be tested on Martin Marietta's LSM, which defined the structural parameters involved in Eqs. (3.24) and (3.25). An aluminum beam was cut to the required dimensions ($L \times b \times t$) to form the link. The values in Table 3.1 were used to derive the mode shapes using the procedure described above. The first three natural frequencies were computed to be 2.015, 9.829 and 35.03 Hz. The corresponding modal displacement shapes and modal strain shapes are shown in Fig. 3.3. In this figure, the elastic beam starts at $x = 0$; the initial portion of the curve ($x = -0.153$ m to $x = 0$ m) is the rigid member connecting the beam to the rotation axis, namely the elbow rotor.

Two M.I.T. undergraduates had previously tested four modal sensors on a single beam [93]. Each sensor covered the full width of the beam, and they were layered two to a side. Some difficulties were encountered with the outermost sensors. The work described in this chapter sought to improve the manufacturing techniques and to demonstrate an alternative to the layered sensors. In particular, fullwidth and halfwidth sensors were

Table 3.1: Physical properties of test article.

Link	L	0.736 m
	b	0.076 m
	t	3.18 mm
	EI	14.23 N $\cdot$ m^2
	ρ	0.653 kg/m
Elbow rotor	a_e	0.153 m
	I_e	0.0253 kg $\cdot$ m^2
Tip payload	m_t	4.398 kg
	a_t	0.03 m
	I_t	0.324 kg $\cdot$ m^2

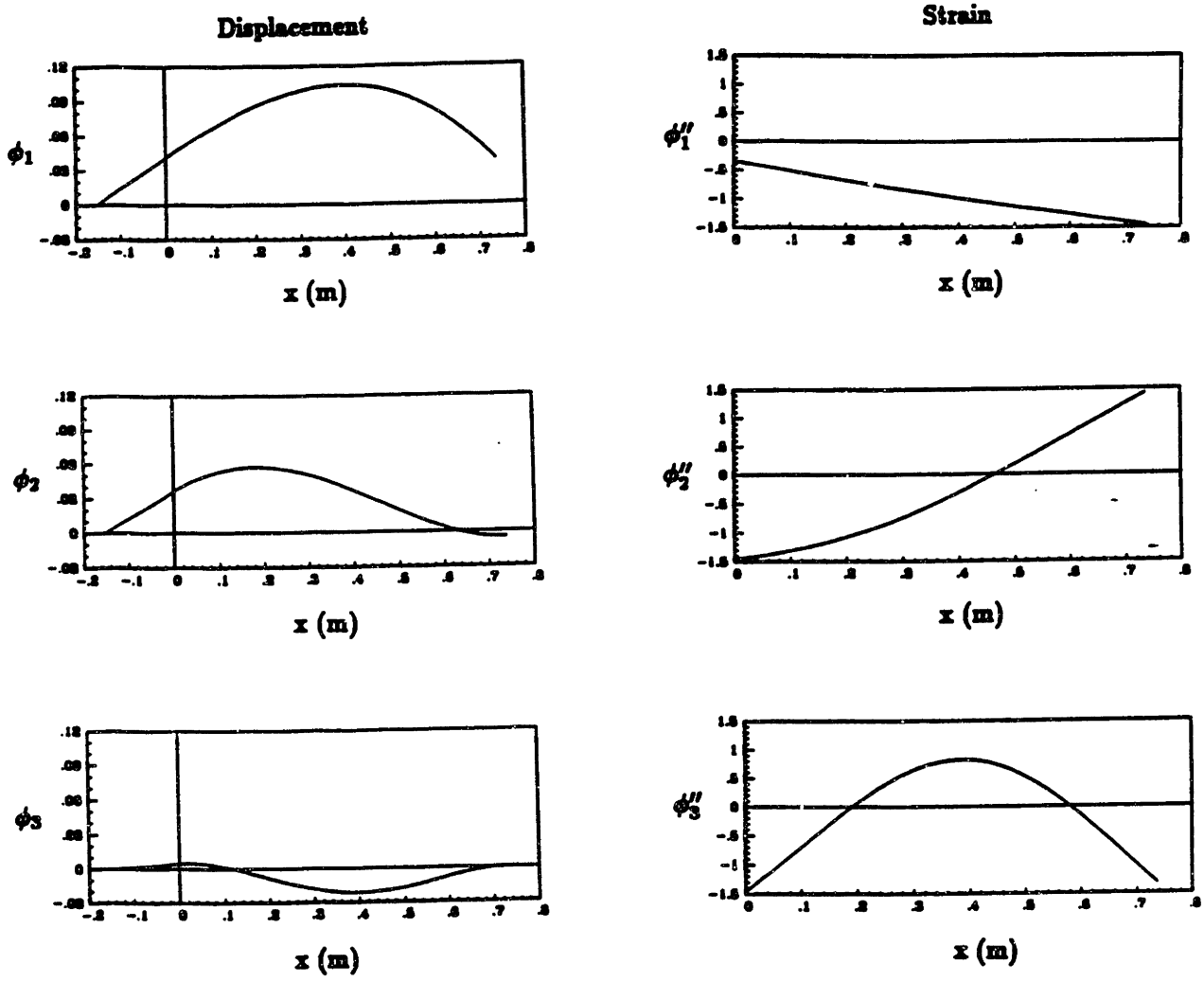

Figure 3.3: $\phi_i(x)$ and $\phi_i''(x)$ for the first three modes.

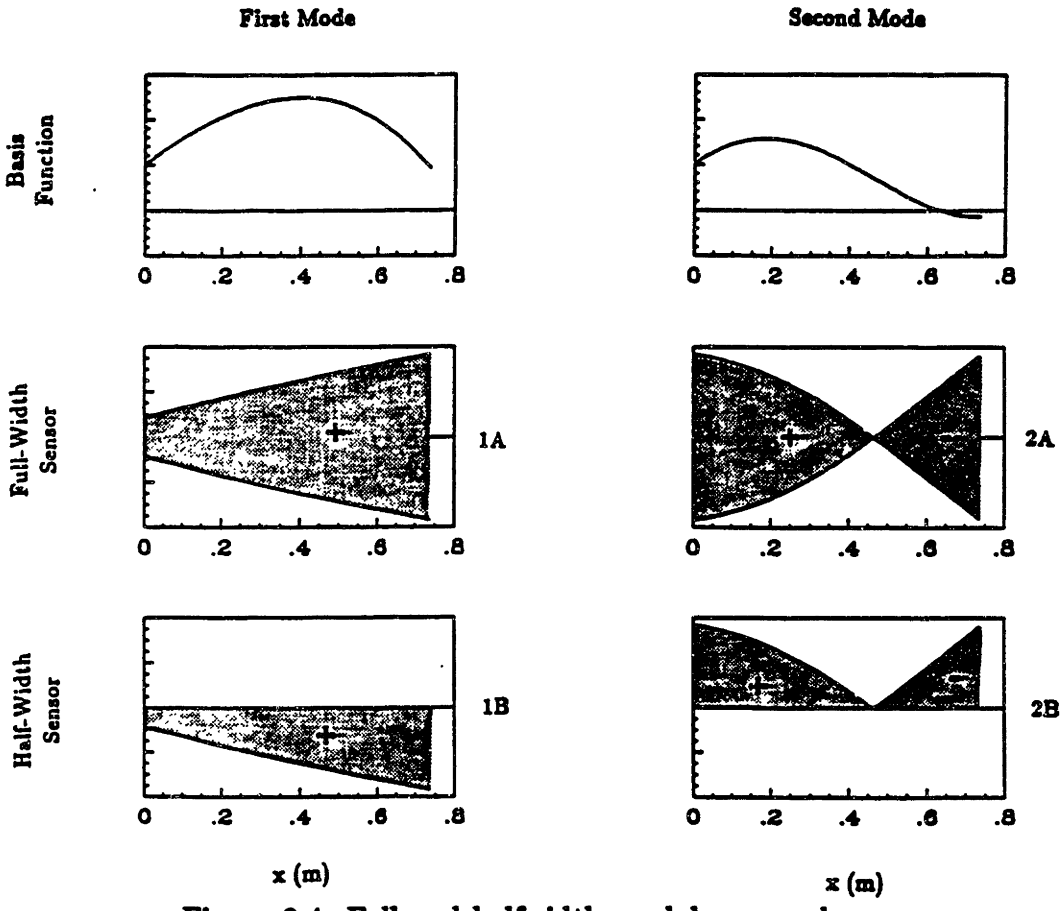

Figure 3.4: Full and halfwidth modal sensor shapes.

compared during the tests described below. Four sensors were designed: Mode One and Two sensors in both the half- and fullwidth formats. Figure 3.4 illustrates the four sensor shapes. In the following discussion, the fullwidth sensors will be designated by an A, while the halfwidth sensors will be designated by a B. The mode number the sensor was designed for will precede this designation, so Sensor 1A is a fullwidth sensor designed to measure the modal coordinate of mode one.

The fullwidth sensors (1A and 2A) were layered, using a layer of adhesive-backed Mylar as insulation; the previous study had used epoxy-soaked fiberglass (see the discussion in Section 2.4.3). Sensor 1A was placed on the beam first and then covered by Sensor 2A. The halfwidth sensors (1B and 2B) were placed beside each other on the other side of the beam. Notice in Fig. 3.4 that Mode Two sensors have a region

requiring negative effective width. This was implemented by manipulating P; the piezo film was turned over for this segment, giving it a negative polarity with respect to the other segment. Another option would be to cross the leads, but this would require four separate leads, two from each electrode. The same effect could have been achieved by repoling the second segment in a large (negative) electrical field; turning a piece of film over was much easier.

The sensors were fabricated as described in Section 2.4. The PVDF used was 52 μm thick KYNAR piezo film with nickel/copper vapor-deposited electrodes. The pieces were cut (rather than etched) to the required shapes and bonded to the aluminum link with adhesive-backed Mylar (25 μm thick). As the PVDF film was provided in sheets 15 cm by 30 cm, and the beam was over 70 cm long, each sensor was made of several segments. Copper tape with conductive adhesive was used to form the electrical connections. In the case of the Mode Two sensors, the two PVDF pieces of opposite polarity were mounted and the upper surfaces were wired together, as had already been done with the lower surfaces. This created the required negative effective width.

The electrical continuity and capacitance of each sensor was checked at several stages of manufacture. The capacitance of 52 μm film is nominally 204 nF/cm^2 [53]. The measured capacitances of Sensors 1B, 2B and 2A were 31 nF, 27 nF and 56 nF, respectively. These values are all about 10% lower than the estimated capacitances based on the area of the sensors. However, these estimates did not account for the gaps in the electrodes due to the segmented construction. More importantly, the film was found to be thicker than advertised. Recall capacitance is inversely proportional to the thickness of the dielectric, so a 5 micron error here would account for the discrepancy in the capacitance measurements.

Reliable readings could not be obtained for Sensor 1A; it appeared to have suffered damage after Sensor 2A was mounted on it, possibly due to excessive pressure on the copper tape and the lack of unmetallized borders. The conductive adhesive could have shorted the two electrodes of this sensor. Another indication of this was that the resis-

tance between the electrodes was only 2000 Ω for Sensor 1A whereas the resistance was over 10 MΩ for the other three.

3.3.3 Experimental Procedure

Two sets of tests were conducted with the PVDF modal sensors. The first series, carried out at M.I.T., consisted of measuring transfer functions from the structural excitation to the sensor output; these results were intended to ensure the sensors were working properly before the complete link was shipped to Martin Marietta. Then, transfer functions would be taken with the link mounted in the LSM. A similar link with strain gauges had been tested in the same manipulator configuration. One of the strain gauges had been placed at a strain node of the second mode, making this mode almost unobservable. Testing both links in the LSM allowed a direct comparison of the ability of these two sensing methods to measure modal coordinates.

A large manipulator was not available at M.I.T. for the initial trials, so a test rig was assembled (Fig. 3.5). This featured steel blocks which could be attached to the link to simulate the LSM's elbow rotor and the payload. These blocks could be interchanged and the position could be varied to obtain various mass and moment of inertia combinations. Shim stock was used to create a flexure providing the pinned boundary condition. Finally, a stinger, a force transducer and a shaker provided the excitation of the structure when calculating transfer functions.

It should be noted that the LSM is a horizontal planar manipulator, while the M.I.T. rig suspended the link vertically. This put the beam under tension, so the partial differential equation, Eq. (3.24), was modified, and gravity effects were added to the boundary conditions, Eqs. (3.25). There was a slight increase in the computed natural frequencies due to gravity (Table 3.2), but the effect of the gravity load could only be seen in the first modal displacement shape (Fig. 3.6); the other two mode shapes were so close to the 0-g case that they overplotted. Even in the case of the first mode, gravity did not have a noticeable influence on the modal strain shape, and it was the modal strain

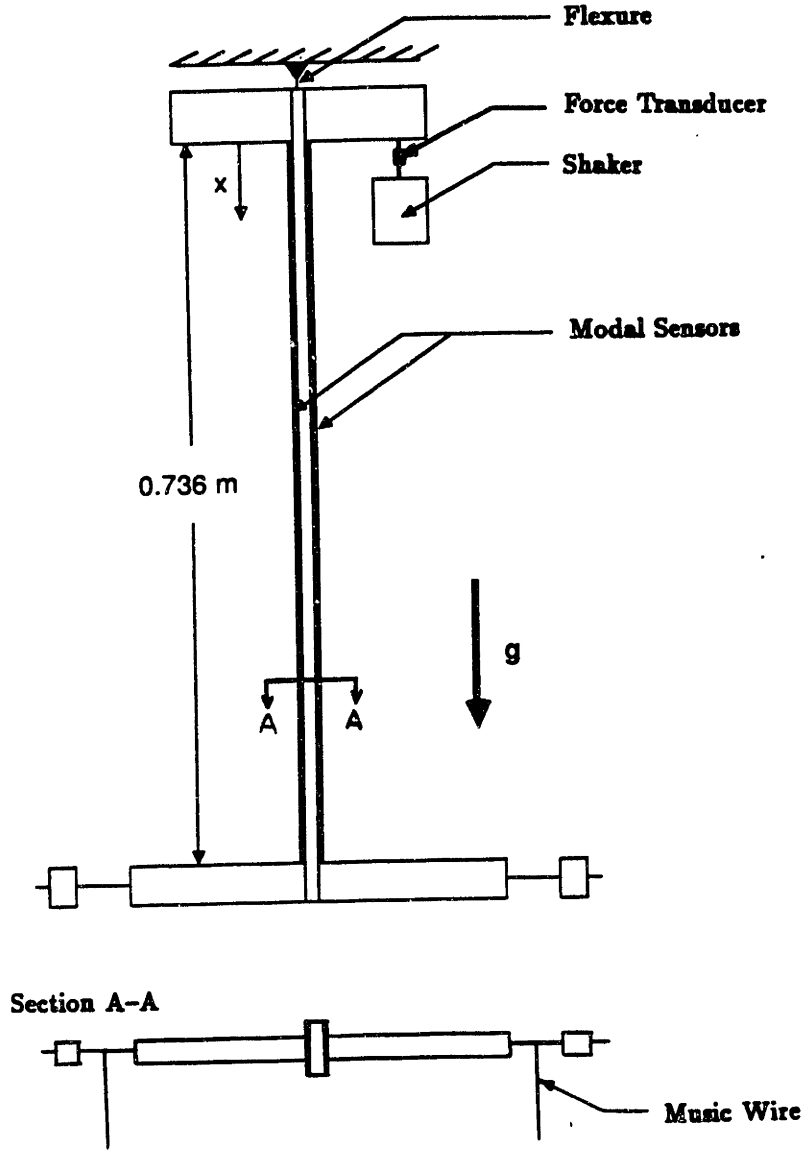

Figure 3.5: Test rig for the M.I.T. link.

Table 3.2: Effect of gravity on the natural frequencies.

	f_1 (Hz)	f_2 (Hz)	f_3 (Hz)
Without gravity	2.015	9.829	35.03
With gravity	2.079	9.832	35.03

shapes that determined the sensor's electrode pattern. So it seemed reasonable to claim that the sensors designed with the 0-g modal strain shapes were virtually orthogonal to the structure's 1-g modal strain shapes.

The gains of the sensors were calculated at several modal frequencies to verify the modal nature of these sensors. The equipment involved is shown schematically in Fig. 3.7. Two basic techniques were used to collect the data. First, the Tektronix 2630 Fourier Analyzer was used to generate a broadband (0–50 Hz) excitation signal. Transfer functions from the force transducer to the modal sensor were computed and natural frequencies of the system were identified. Then a Wavetek 11 MHz Stabilized Function Generator was used to analyze the response at the natural frequencies more closely. Harmonic excitation signals were used in these tests.

Measurements with a high input impedance device were used to obtain the film's signal (*q.v.* Section 2.4.4). The first mode was around 2 Hz and the lowest sensor capacitance was around 25 nF, so the relationship $f_c = 1/(2\pi RC)$ indicated an input impedance of at least 3.2 MΩ would be required to capture the low frequency portion of

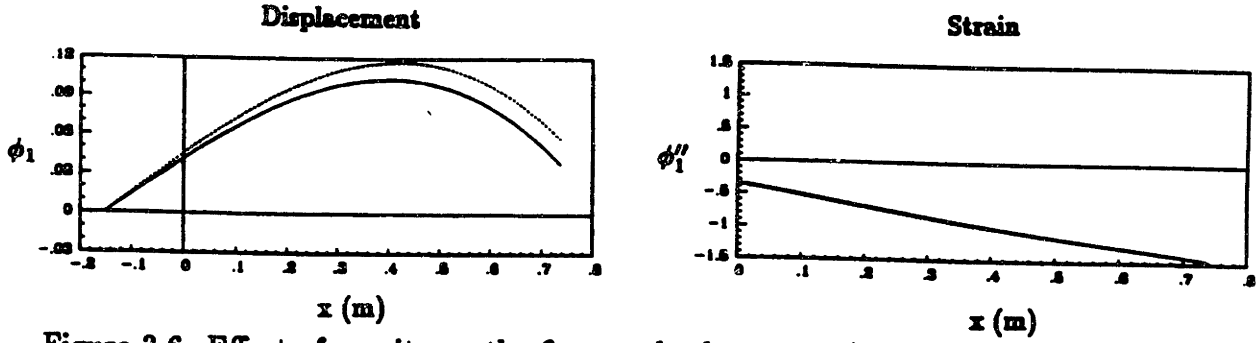

Figure 3.6: Effect of gravity on the first mode shape. 0-g (solid) and 1-g (dashed) cases are shown.

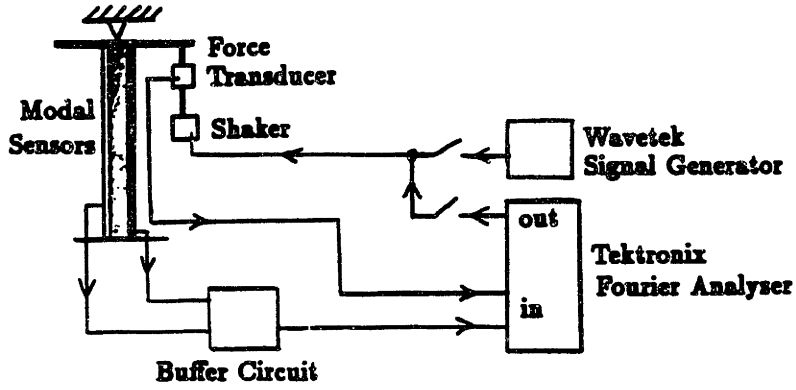

Figure 3.7: Schematic of experimental arrangement.

the signal without significant attenuation. A standard inverting op amp circuit was used to buffer the input as the Fourier Analyzer's input impedance was only 100 kΩ. Moderate forces produced substantial voltages (0.5 V near resonance), so little amplification was needed. The amplifier had a gain of -1.8 and an input impedance of 12 MΩ, giving a highpass corner frequency of 0.53 Hz.

The LSM's payload is supported by airpads on a flat table. Originally the M.I.T. rig did not provide this constraint, allowing out-of-plane motion. The low frequency torsional modes were easily excited during testing, so music wire was attached to the payload to restrain out-of-plane motion (see Fig. 3.5). The torsional modes were suppressed, and the natural frequencies of the flexural modes did not change after the addition of the wires, indicating the flexural modes were not significantly affected.

Random noise was used to excite the shaker for broadband measurements; the noise was pseudo-white when generated by the Fourier Analyzer, but would have been colored by the amplifier and the shaker dynamics. Rather than analytically accounting for these dynamics, a force transducer placed between the shaker and the structure measured the excitation actually seen by the structure. The buffered sensor output was the other signal used for transfer function computations. The transfer functions had units of volts per volt. It would have been fairly easy to calibrate the force transducer, but absolute measurements were not required for these tests. During the sinusoidal tests, the force

transducer output and the sensor signals were also measured, and the gain (V/V) for a given natural frequency was calculated.

The instrumented link was then tested in the LSM at Martin Marietta Space Systems. The ability to shape a piezo film sensor such that it only observes one mode was compared with the ability to place strain gauges so as to make some modes unobservable.

Apart from the actual Large Space Manipulator, there were two factors which affected the sensors' performance at Martin Marietta. The M.I.T. tests had been conducted in June 1989, while the LSM ones were not completed until February 1990. During this time the copper tape lost much of its effectiveness, both as a conductor and as an adhesive. This necessitated the repair of some of the leads. Also, the pulse-width modulated amplifiers used to drive the torque actuators produced quite a lot of electromagnetic (EM) radiation. But once the loose connections were fixed, there was little EM interference, and more extensive shielding was not necessary. Large clean signals were produced for moderate tip displacements, about 5 V for 5 cm displacements.

The Martin Marietta (M.M.) link was structurally identical to the M.I.T. link. The similarity of the dynamic properties is illustrated in Fig. 3.8, which shows the transfer function from elbow torque to elbow angular rate for both links. The M.I.T. beam exhibited higher damping in all three modes, especially the third one. This is attributed to the many layers of piezo film and Mylar attached to the M.I.T. beam.

Rather than modal sensors, the M.M. link was instrumented with two strain gauges. The first one was mounted at $x = 0.127$ m, near the shoulder actuator in the hope that the sensor and the actuator would be collocated at low frequencies. The second one was placed at $x = 0.459$ m, slightly past the center of the beam. This point was chosen because ϕ_2'' is almost zero here (see Fig. 3.3), making the second mode almost unobservable for this sensor.

A Hewlett-Packard 3462 FFT Dynamic Signal Analyzer was used to measure the transfer functions from elbow torque to various sensor outputs. The units of these transfer functions are $V/N \cdot m$. Strain gauge conditioners were used with the strain

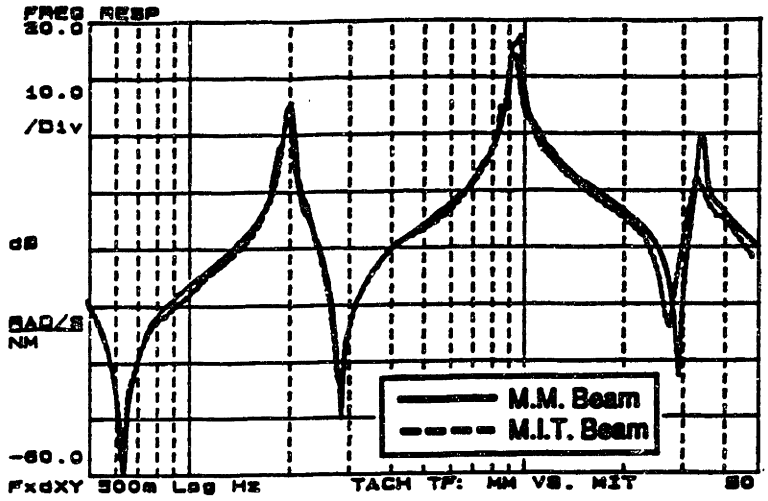

Figure 3.8: Elbow torque to elbow angular rate transfer functions.

gauges on the M.M. link, and a unity gain buffer amplifier (Fig. 2.6) was used to condition the output of the modal sensors on the M.I.T. link. The transfer functions included the first three modes, covering a frequency range of 0–50 Hz.

3.3.4 Experimental Results

The sensor gains for the first three modes and the corresponding natural frequencies are presented in Table 3.3. This data was collected in the M.I.T. test rig. The experimental natural frequencies in Table 3.3 are within 5% of the 1-g natural frequencies presented in Table 3.2, so the endbodies on the MIT rig are reasonable substitutes for the LSM bodies described in Table 3.1. These sensor gains were obtained from the harmonic excitation tests. While the general modal nature of the sensors could be seen in the transfer functions developed using the random excitation, the broadband nature of this method precluded the accurate calculation of sensor gains.

The Mode One sensor (1B) had its greatest gain at the first natural frequency of the beam. While this could have been due to a variation in the damping of the first three modes, the large difference between the response to the first mode and the other modes indicates that other factors, namely the sensor's modal filtering aspects, were at work. At the first natural frequency, the Mode One sensor also had the greatest gain of the

Table 3.3: Experimental gains for the modal sensors.

Sensor	$f_1 = 2.18\,\text{Hz}$	$f_2 = 10.31\,\text{Hz}$	$f_3 = 34.1\,\text{Hz}$
1B	346	5.69	4.89
2B	13.7	310	0.714
2A	34.8	325	2.12

three sensors, as it had been designed to sense this mode. Both Mode Two sensors (2A and 2B) had their greatest gains at the second natural frequency, and the gain of either Mode Two sensor at this frequency was greater than the gain of the Mode One sensor. So the modal filtering characteristics of modal sensors were verified experimentally.

The gains for the half- and fullwidth Mode Two sensors (2A and 2B) indicate comparable modal filtering is being achieved with the two sensor formats. Use of halfwidth sensors makes it possible to measure the modal coordinates of several modes on a single (one-dimensional) structure without having to deal with the extra complexity of layered sensors. However, the lack of symmetry in the halfwidth sensors makes them susceptible to torsion.

The performance of the modal sensors can be quantified by normalizing. For example, Sensors 1B and 2B are compared in Table 3.4. The normalization was done down the columns of Table 3.3, which corresponds to exciting the structure at a natural frequency and then comparing the output of the two modal sensors. The damping of each mode must be known to calculate the theoretical values of the off-diagonal entries. Half power

Table 3.4: Normalized gains for the halfwidth modal sensors.

Sensor	$f_1 = 2.18\,\text{Hz}$	$f_2 = 10.31\,\text{Hz}$
1B	100%	1.8%
2B	4.0%	100%

measurements revealed that the first two modes had similar damping ratios. Thus, if Table 3.4 were measured for two sensors without modal filtering characteristics, the four gains would all be roughly equal. The highly diagonal nature of the gain matrix for the modal sensors indicates they have good modal filtering properties. While the residuals r_{ij} (the normalized mode j gain of a sensor designed to observe mode i) cannot be used for a detailed comparison of the sensors—we cannot conclude Sensor 1B is a better modal sensor than Sensor 2B—their general values do help characterize the sensor's performance. The residuals obtained in these tests are in the same range as reported by previous studies: Lee's residuals were $r_{12} = 18\%$ and $r_{21} = 3\%$ [7], while all the residuals from the 16.62 project were below 5% [93].

The tests at Martin Marietta involved two links: the M.M. link with strain gauges and the M.I.T. link with modal sensors. Both links were tested in the LSM as described above. The natural frequencies of the links with the elbow locked are shown in Table 3.5; the theoretical natural frequencies for the 0-g case in Table 3.2 are repeated here for convenience. This data provides further proof of the similarity of the two links, and it shows that the model used above is accurate for this frequency range. The measured frequencies are within 1% of the predictions, with the sole exception of f_2 for the M.I.T. beam. The cause of this softening is unknown.

The M.M. link's transfer functions from elbow torque to strain gauge output are shown in Fig. 3.9 [110]. Note the alternating pole-zero structure for strain gauge 1, indicating that this strain gauge is effectively collocated with the elbow actuator over the frequency range being studied (0–50 Hz). Checking Fig. 3.3, we see ϕ_i'' is nonzero

Table 3.5: Comparison of natural frequencies.

	f_1 (Hz)	f_2 (Hz)	f_3 (Hz)
M.I.T.	2.02	9.40	34.8
M.M.	2.03	9.93	34.6
Model (0-g)	2.02	9.83	35.0

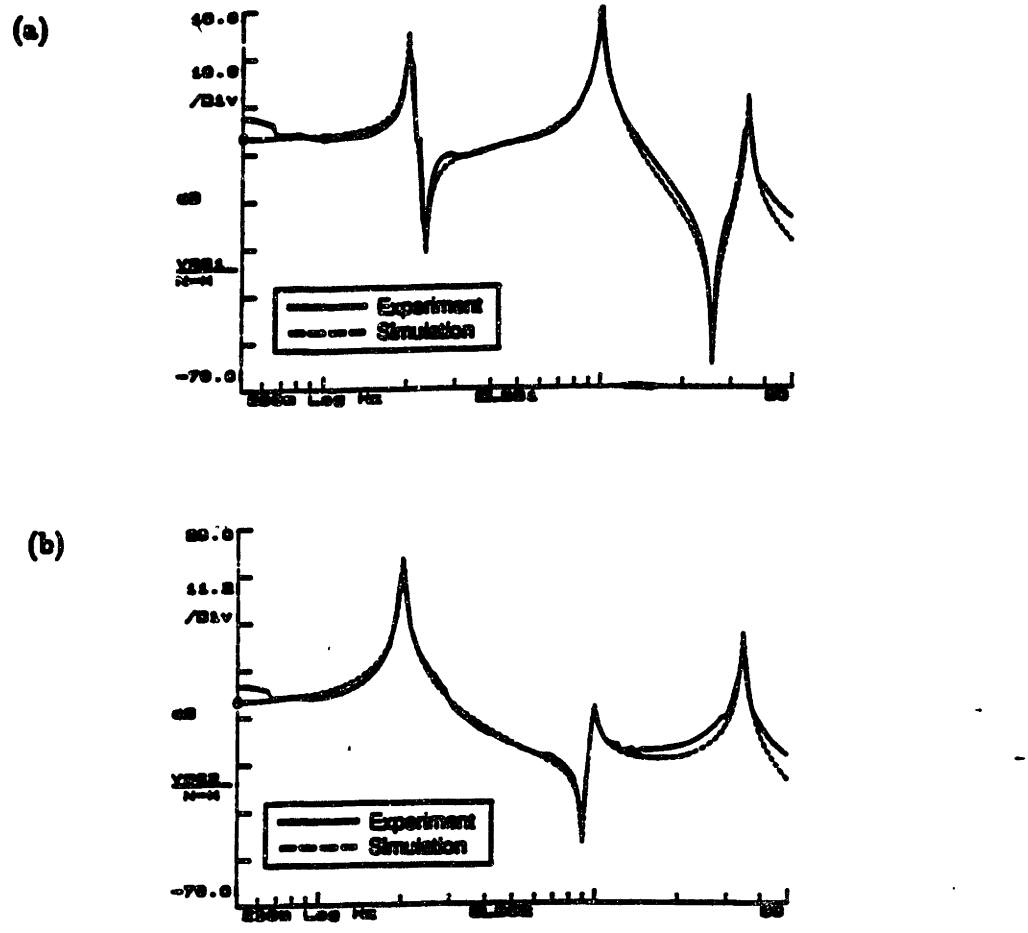

Figure 3.9: Transfer functions from elbow torque to strain gauge output. (a) Strain gauge 1, at $x = 0.127$ m; (b) Strain gauge 2, at $x = 0.459$ m.

for $i = 1, 2, 3$ at this strain gauge's location, $x = 0.127$ m. The response to the second mode is somewhat greater than the response to the other two modes, but all modes are observed by this sensor. On the other hand, strain gauge 2 is placed near a node of ϕ_2''. The reduced sensitivity to this mode is seen in Fig. 3.9. Note that the response of this strain gauge to mode three is just as great as the response to this mode by the other strain gauge. When comparing these two transfer functions, be careful of the vertical axes, as the scales differ.

The transfer functions from elbow torque to buffered modal sensor output are shown in Fig. 3.10. Take note that the vertical range changes yet again. The Mode One sensor has a large peak at the first natural frequency, whereas the Mode Two sensors display

little response here, indeed, there is a zero at this point rather than a pole. The second and third modes can be seen in all three transfer functions, but these modes certainly do not contribute equally to the response. In the case of the Mode One sensor, the response at the second and third natural frequencies is much smaller in magnitude than the response to the first mode, and the Mode Two sensors are most sensitive to the second mode, as hoped. The transfer functions also demonstrate the similarity between the response of the full- and halfwidth sensors 2A and 2B. Another interesting point in this figure is the way that the off-design response is often associated with a fairly tight pole-zero pair: examine, for example, the response to mode two for the Mode One sensor and the response to modes one and three for the Mode Two sensors. But there is no zero in the immediate vicinity of the design mode for any of these sensors. This observation will be picked up again in the next chapter.

Both the Mode One sensor and the second strain gauge show reduced sensitivity to mode two: the modal sensor's response is down 30 dB from the mode one response, and the strain gauge's is down about 20 dB. But the modal sensor also exhibits very low sensitivity to mode three, while the strain gauge picks up this mode quite well. This demonstrates the advantage of choosing a sensor that is orthogonal to a whole set of eigenfunctions, as opposed to positioning a sensor to reduce the response to one particular component.

In addition to these demonstrations, Ref. [98] describes some tests conducted at Martin Marietta which used the modal sensors as a means of verifying the accuracy of assorted estimators. This was quite successful for "mild" manuevers; it remains to be tested with manuevers involving angular rates large enough to excite several flexible modes.

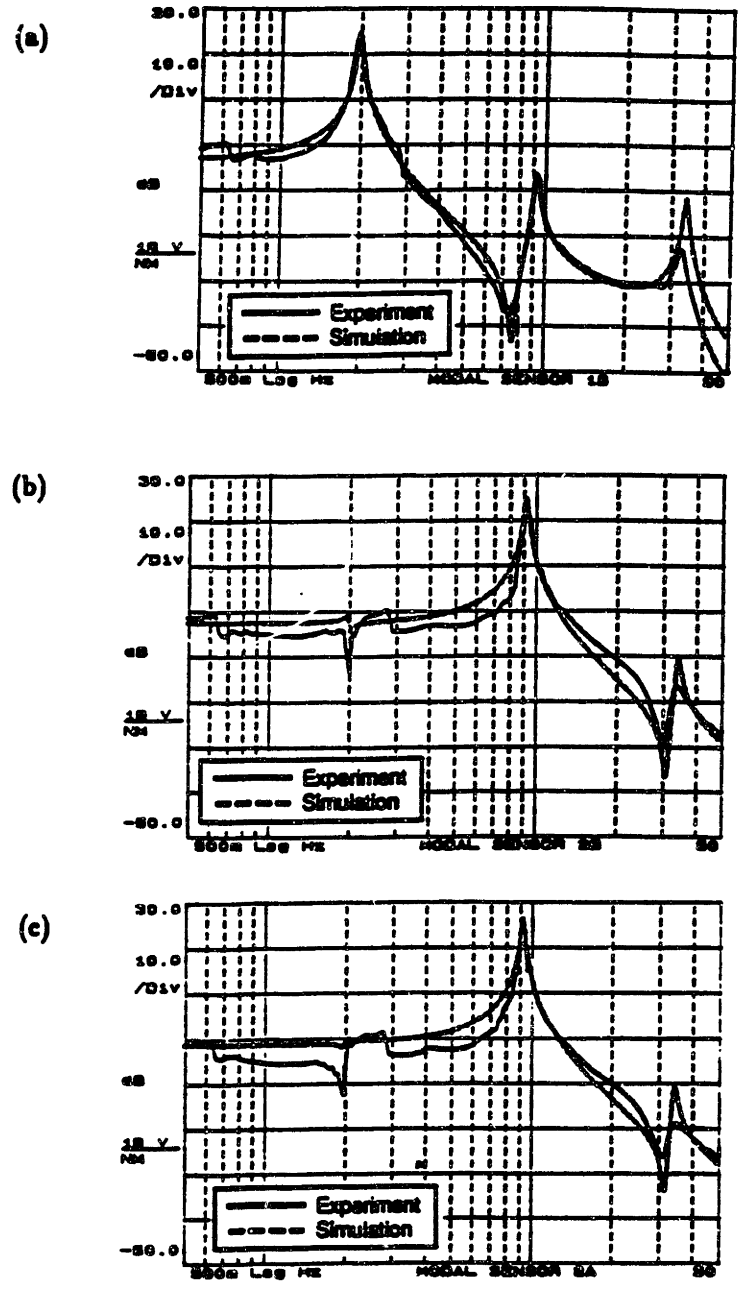

Figure 3.10: Elbow torque to buffered modal sensor output transfer functions. (a) Sensor 1B; (b) Sensor 2B; (c) Sensor 2A.

3.4 Summary

A single link of Martin Marietta's Large Space Manipulator was used to demonstrate modal sensors. These sensors can be useful for modal control, as they provide direct access to the modal states. They can be used as part of the feedback loop, or they can be used to check the accuracy of modal state estimators. The partial differential equation for a Bernoulli-Euler beam was combined with the piezoelectric sensor equation to reveal that modal sensors can be created by making the effective electrode width proportional to the second derivative of the modal displacement shape. The polarity of the film is used to implement negative effective widths.

Four modal sensors were mounted on an aluminum link. Full- and halfwidth sensors for modes one and two were tested in the Large Space Manipulator. Previously, modal sensors had only been tested on cantilever beams, a much simpler structure dynamically. Future tests should take advantage of the ability to change the LSM's payload to test the sensitivity of modal sensors to boundary conditions. Three sensors performed well, with the response to other modes being between 2% and 10% of the response to the design mode. One sensor was lost during manufacture. Good signals were obtained using only a high input impedance buffer circuit to condition the modal sensor output.

An identical link was instrumented with strain gauges. While a strain gauge could be positioned so as to reduce the sensitivity to one mode, the modal sensor reduced the sensitivity to all modes except the design mode. Modal sensors can be implemented using the continuously distributed measurements provided by means of piezo film, thereby avoiding the problem of spatial aliasing.

Chapter 4

Spatial Filters

The modal sensors developed in Chapter 3 are a dramatic demonstration of the way that a transducer designer can dictate the characteristics of a PVDF piezo film sensor. These sensors combine measurements which are spatially distributed along a structure into a single temporal signal, with the weighting function being determined by the geometry of the film's electrodes. The ability to specify this geometry, and thereby specify the sensor's response, inspired a search for sensors which would be useful for structural control applications but are not realizable with traditional transducers. Distributed PVDF sensors with spatially shaped electrode patterns were then studied to try to implement some of these unusual designs. In this chapter, several examples are discussed in detail and experimental demonstrations are presented.

Before proceeding, however, some terminology must be explained. As was explained in Section 3.2, the relationship between the mechanical deformation of a uniform beam and the charge generated by a layer of PVDF is

$$Q(t) = -e_{31} z \int_0^l \mathcal{F}(x) \frac{\partial^2 w(x,t)}{\partial x^2} \, dx \tag{4.1}$$

where $Q(t)$ is the charge generated by the piezo film, z is the distance from the beam's neutral axis to the PVDF's midplane, e_{31} is a piezoelectric constant, l is the length of the sensor, $\mathcal{F}(x)$ is the effective electrode width and $w(x,t)$ is the transverse displace-

ment of the beam. The assumptions behind this equation, and the definitions of the variables, are given in Chapter 3. This can viewed as a weighted average of the structure's strain profile, where the weighting function is determined by the geometry of the film's electrode. So piezo film sensors are area-averaging strain (or strain-rate) sensors. Note that this averaging implies spatial integration, which is known to be a smoothing operation. In the following discussion, these sensors will be called averaging sensors or spatial filters.

4.1 A Sensor Wish List

There are many examples of structural control applications where desired objectives could be achieved if it were possible to implement noncausal compensators in real time. These applications come from both the world of the control theoretician and the world of the control engineer.

Modelling errors and high-frequency noise are common problems in feedback systems, forcing sensor gains to be rolled off well before these frequencies. However, point sensors are causal, *i.e.* they can only sense past and present information—they cannot anticipate future information. Because the sensors are causal, the Bode gain-phase theorem [111] governs the relation between the sensed quantity and the sensor output. This theorem relates the magnitude and the phase of the sensor's transfer function from excitation to response. An implication of this theorem is that there will always be phase lag associated with any gain rolloff. The phase lag reduces the feedback control system's phase margin, possibly creating an instability. Reference [112] provides a good example of this behavior. An attempt was made to feed back strain rate on a free-free beam using piezoceramic sensors and actuators. An instability was noted at 3500 Hz, so an elliptic filter with a corner frequency of 325 Hz was added to gain-stabilize the system. However, because of the phase lag associated with the filter, the closed-loop system now had an instability at 210 Hz. A noncausal sensor would allow the gain to be rolled

off above, say, 325 Hz, without introducing additional phase lag, thereby avoiding the addition of new instabilities to the closed-loop system.

A somewhat more exotic example arises when optimal power absorption at structural junctions is studied. It has been shown that *all* the resonances of a Bernoulli-Euler beam could be eliminated using one actuator and its dual sensor if it were possible to implement the noncausal compensator $\sqrt{-s}$, where s is the temporal Laplace variable [12,113]. Compensators for use with a dual sensor/actuator pair were developed using optimal control theory to minimize a cost functional involving control effort and power flow. It was also proved that the resulting compensator will be noncausal unless the dereverberated mobility is constant [11]. The rod is the only simple structural system with a constant dereverberated mobility—the rod's transfer function from applied force to velocity has a flat backbone curve. These optimal noncausal compensators cannot be implemented in real time with a single point sensor. But the compensator can often be separated into a causal and noncausal portion: $\sqrt{s}$ and $\sqrt{-1}$ in the beam example. The optimal compensators could be realized if it were possible to handle the noncausal dynamics with a spatially distributed sensor, leaving the causal dynamics to be implemented with analogue or digital electronics.

We have seen there are a number of good reasons to try to implement noncausal compensators. The problem is that some portion of their singularities lies in the right half of the Laplace plane. These singularities can be interpreted in one of two ways: they represent dynamics which are stable in negative time, or they represent dynamics which are unstable in positive time. If the dynamics are unstable, any input would cause the sensor's signal to tend to infinity, and it would continue to increase even when the input has returned to zero. Such a sensor is not much use for making measurements and obviously could not be used in a feedback loop. So the negative-time interpretation is more helpful when considering sensors. It corresponds to convolving future information negatively in time to yield a present sensor output.

It has already been noted that future information is not available to a lone point

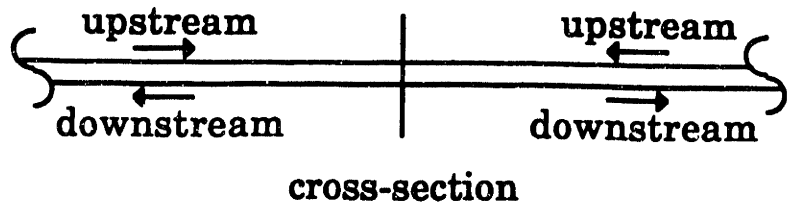

Figure 4.1: Upstream and downstream signals.

sensor. But consider the situation from a travelling wave perspective. We are interested in the deformation at a particular cross-section of the structure. The future deformation of that cross-section will be determined by the spatial Fourier components which are presently propagating towards it. Similarly, the spatial Fourier components which created the past deformations are now propagating away from the cross-section. So future and past information can be obtained by looking upstream and downstream from the cross-section of interest. These stream directions are not distinguished on the basis of their location, as a single physical cross-section can be both upstream and downstream. Rather, they are determined by the direction in which a signal is travelling with respect to the original cross-section (Fig. 4.1). If measurements are made both upstream and downstream, it should be possible to determine the past and future structural deformation at this cross-section as long as there is no forcing present between the cross-section of interest and the measurement locations. So, spatially distributed structural measurements would make the implementation of compensators with both causal and noncausal dynamics possible.

4.2 Implementation of Spatial Filters

A spatial filter can be created in two basic ways. Both combine spatially distributed structural measurements using a weighting function, but one uses discrete point sensors (*e.g.* strain gauges) while the other uses a continuously distributed area-averaging sensor (*e.g.* a piezo film sensor).

The first method utilizes an array of discrete point sensors which are distributed along

the structure. These sensors measure the deflection (or strain, etc.) profile at discrete locations. The signals can then be weighted by interpolation functions to obtain an estimate of the complete deflection profile. The implementation of modal filters with discrete sensors is an example of this type of spatial filter [8].

A similar result can be achieved with a single distributed sensor. The weighting function is now determined by the sensor's geometry. No interpolation is required; the continuously distributed sensor measures the actual deflection profile over the sensor's entire length.

In practice, the array has the advantage that a wide range of point sensors are available: strain gauges, accelerometers, LVDTs, etc. If the distributed sensor is made of piezoelectric film, strain and strain rate are the only measurements easily accessible, although an accelerometer could be fashioned by covering the entire electrode with a mass. The array is considerably easier to apply to complex geometries than the distributed sensor. It is also reasonably easy to modify the interpolation functions, permitting a different averaging sensor to use the same hardware. In the case of the distributed sensor, such a change is much more involved, as sensor's actual geometry must be altered.

The distributed sensor reduces the signal processing required to obtain the desired measurement; the sensor itself performs the weighted averaging. This could be important for digital controllers, where all calculations have to be completed in one sampling period. It could also mean local loops can be closed with much simpler processors. The real advantage of this type of averaging sensor is that it avoids spatial aliasing. The continuous deflection profile along the length of the sensor is measured; discrete measurements are not interpolated. Note that both the array and the distributed sensor will suffer from truncation effects if they are restricted to a portion of the structure rather than covering the full structural domain.

4.3 Familiar Examples of Spatial Filters

The PVDF sensors discussed in previous chapters can be viewed as spatial filters. This emphasizes the frequency response of the sensor, whereas the modal response of the modal sensors was highlighted in Chapter 3. It has been noted that the response of a uniform sensor (one of constant width) on a cantilever beam is the same as the response of a point angular-displacement sensor mounted at the tip of the beam [79,81]; looking at the uniform sensor as a spatial filter yields a rather different interpretation. A travelling wave approach is used to study the response of the both these sensors; Ref. [9] provides a good explanation of this analysis technique.

4.3.1 Modal Sensor

The modal sensors of Chapter 3 consisted of a strain-sensing piezo film layer mounted on a beam. For simplicity's sake, in this section we will consider a displacement-sensing layer mounted on a rod. This will demonstrate several features of modal sensors.

The even and odd mode shapes for a free-free rod are

$$\phi_m(x) = A_1 \cos\left(\frac{2m\pi}{L}x\right) \tag{4.3a}$$

$$\phi_n(x) = A_2 \sin\left(\frac{(2n+1)\pi}{L}x\right) \tag{4.3b}$$

where L is the length of the rod. As our hypothetical material is displacement-sensitive, the modal sensor must be shaped proportional to $\phi(x)$ in order to take advantage of the orthogonality condition. If an even mode sensor is made, the sensor equation is

$$\begin{aligned} \bar{u} &= \alpha \int_{-L/2}^{L/2} u(x)\cos(k_0 x)\,dx \\ &= \alpha \int_{-L/2}^{L/2} u(x)\frac{1}{2}\left(e^{ik_0 x} + e^{-ik_0 x}\right)\,dx \end{aligned} \tag{4.3}$$

where $u(x)$ is the longitudinal displacement of the rod, $\bar{u}$ is the output of the modal sensor, α is a gain, k_0 is the mode's wavenumber and i is $\sqrt{-1}$.

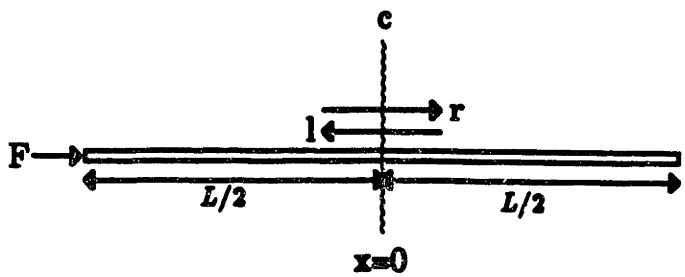

Figure 4.2: Free-free rod with a force applied at the left end.

Assume a force $F(\omega)$ is applied at the left end of the rod (Fig. 4.2). It can be shown [9] that the displacement is given by

$$u(x,\omega) = \frac{F(\omega)}{ikEA}\frac{\xi}{1-\xi^4}\left(\xi^2 e^{ikx} + e^{-ikx}\right) \tag{4.4}$$

where E is the rod's modulus of elasticity, A is the rod's cross-sectional area, ξ is the transmission factor $e^{-ikL/2}$, E is the rod's modulus of elasticity, A is the rod's cross-sectional area and k is the wavenumber. The wavenumber can be thought of as the spatial frequency and is related to the temporal frequency through the dispersion relation. For a rod, this is

$$k^2 = \frac{\rho}{E}\omega^2 \tag{4.5}$$

Substituting the expression for the rod's displacement, Eq. (4.4), into the sensor equation, Eq. (4.3), and integrating over the length of the rod, we obtain the transfer function from the applied force to the modal sensor signal:

$$\frac{\bar{u}}{F} = \frac{1}{ikEA}\frac{\xi}{1-\xi^2}\left\{\frac{\sin\left([k+k_0]\delta\right)}{k+k_0} + \frac{\sin\left([k-k_0]\delta\right)}{k-k_0}\right\} \tag{4.6}$$

Some insight into this sensor's behavior can be gained by considering the output of a point sensor u_c located at the center of the rod. Substituting $x = 0$ into Eq. (4.4)

$$u_c(\omega) = \frac{F(\omega)}{ikEA}\frac{\xi}{1-\xi^2} \tag{4.7}$$

This can be combined with the transfer function from the applied force to the modal sensor signal, Eq. (4.6), to yield the transfer function from the displacement at the center

to the output of the modal sensor, $\bar{u}/u_c$. Calculated as the ratio of transfer functions, $\bar{u}/M : u_c/M$, the resulting transfer function effectively eliminates the structural dynamics, leaving the filter dynamics of the distributed sensor with respect to the point sensor. For example, if the sensor is designed for the fourth even mode, $m = 4$, then $k_0 = 8\pi/L$ and the filter dynamics are

$$\frac{\bar{u}}{u_c} = \frac{2k}{k^2 - (8\pi/L)^2} \sin(kL/2) \tag{4.8}$$

The magnitudes of these transfer functions are shown in Fig. 4.3. The dotted curve is the transfer function from the applied force to the displacement at the center of the rod, the dashed curve is the transfer function from the applied force to the output of the modal sensor, and the solid curve is the transfer function from the displacement at the center of the rod to the output of the modal sensor. A unit rod ($EA = 1$, $\rho A = 1$ and $L = 1$) was used in the computations, and the modal sensor was shaped to detect the fourth even mode ($k_0 = 8\pi$). The dispersion relation, Eq. (4.5), has been used to present the data as a function of temporal frequency.

The point displacement sensor at the midpoint of the rod can only detect even modes. The sine function in the transfer function from this sensor to the modal sensor, Eq. (4.8), is zero at all wavenumbers corresponding to an even mode. But at the design wavenumber, k_0, the denominator also goes to zero, so the magnitude of the transfer function at k_0 is $L/2$. This can be seen in Fig. 4.3: $\bar{u}/u_c$ has a zero at each resonance of u_c/F, except at the fourth even mode—the mode the sensor was designed to detect. The first even mode is at 1 Hz and the fourth even mode is at 4 Hz. The result of the zero structure of $\bar{u}/u_c$ is that the modal sensor is only able to observe one mode. A similar analysis with the point sensor at some location other than the midpoint could be used to demonstrate why the modal sensor cannot observe any odd modes.

Imagine that the sensor's shape was changed slightly. This would shift the zeros of $\bar{u}/u_c$ in Fig. 4.3. If the shift were small, near pole-zero cancellation would be exhibited; the modal sensor would respond to all mode shapes, but with the greatest sensitivity to its design mode. This was indeed the behavior exhibited by the experimental modal

sensors. The pole-zero pairs can be seen in the transfer functions too (see Fig. 3.10).

So the modal sensors can be interpreted as being equivalent to point sensors followed by filters which have zeros near all the structural poles except one, namely the sensor's design mode. The "filter" is determined by the sensor's geometry, so if the modal sensor isn't shaped properly, the other modes will also be observable. Other electrode geometries will produce different "filters."

4.3.2 Uniform Sensors

Most experiments with distributed PVDF sensors have used uniform piezo layers [72,74, 79,4]. The output from these sensors can also be interpreted as being the filtered output from a point sensor. The filter characteristics can be determined almost intuitively.

The film's electrode pattern can be described as a distribution of constant amplitude and infinite extent multiplied by a rectangular window with an aperture l, where l is the length of the sensor. These functions can be transformed into the wavenumber domain using the Fourier transform. Then, rather than multiplying two functions of x, two functions of k are convolved together. The constant remains a constant, and the rectangular window is transformed into a sinc function. The sinc function, $\frac{\sin(\pi kl)}{\pi kl}$, is shown in Fig. 4.4. The first node of this function occurs at $kl = 1$, so the longer the sensor is, the lower the corner wavenumber and frequency.

This filtering process has long been recognized in transducer arrays and optical diffraction gratings. In the 1960s, pressure transducers were used to form a wave-vector filter to study the low-wavenumber components of the pressure field in turbulent boundary layers [114]. Later, flexible beams and membranes [115,116] were used rather than tranducer arrays—this was the second method of implementing an averaging sensor discussed above. These studies demonstrated that these spatial filters can be a very useful measurement tool. But the sinc function has two drawbacks when using it for active control: it does not roll off very quickly, and there is a sign change at each node, which can destroy any phase margin that may have been preserved up to this point. The

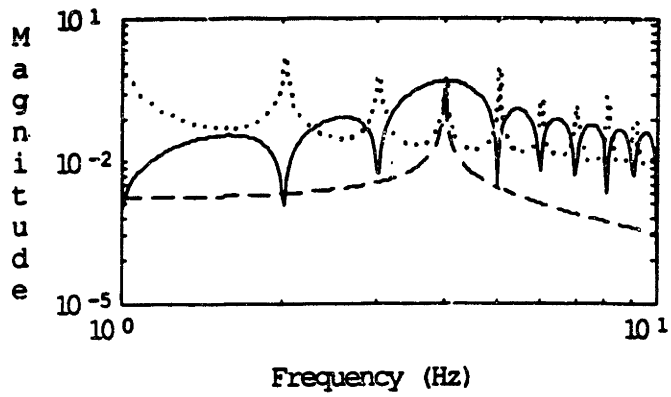

Figure 4.3: Transfer functions from applied force to midpoint displacement (dotted), to modal sensor output (dashed), and from midpoint displacement to modal sensor output (solid).

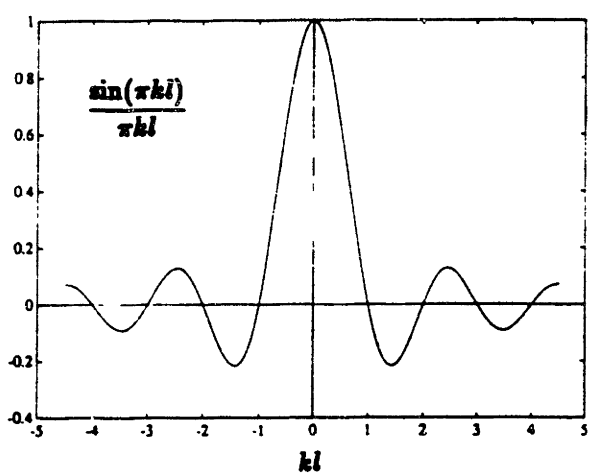

Figure 4.4: The sinc function.

remainder of this chapter explores the effects and possible benefits of using nonuniform PVDF sensors.

4.4 Exponential Sensor

As discussed above, a sensor with magnitude rolloff but without phase lag would be very useful for structural control applications. Such a sensor was designed using the idea of a spatial filter.

If the sensor dynamics include a left half plane (LHP) pole, we have the classic situation of rolloff and phase lag. But if we add the symmetric right half plane (RHP) pole, we will have twice the rolloff, but the phase contributions from the two poles will cancel, leaving no net phase lag. The RHP pole is noncausal, but the distributed sensor should allow us to deal with this.

Before proceeding with the analysis of such a sensor, an intuitive design is presented. Figure 4.5 can be thought of as a roadmap to the design of an exponential sensor for a Bernoulli-Euler beam. The pictorial notation used by Bracewell [117] allows a great deal of information to be presented in a fairly compact form. The map starts with the desired frequency response—this is specified by the designer. It is converted into the wavenumber domain through the use of the beam's dispersion relation. The resulting spatial frequency response is still an exact representation of the desired filter characteristics, so the inverse Fourier transform is used to convert the spatial frequency response into the corresponding spatial distribution. For the case shown in Fig. 4.5, the required spatial electrode pattern is an exponential function. This function is infinite in extent, and any physically-realizable sensor must be of finite size, so the spatial distribution is multiplied by a window to truncate it—a rectangular window is demonstrated here. The product of these functions is the electrode pattern actually applied to the piezo film. The effect of the window on the wavenumber response can be found by transforming the product of the two spatial functions (the infinite distribution and the window) into

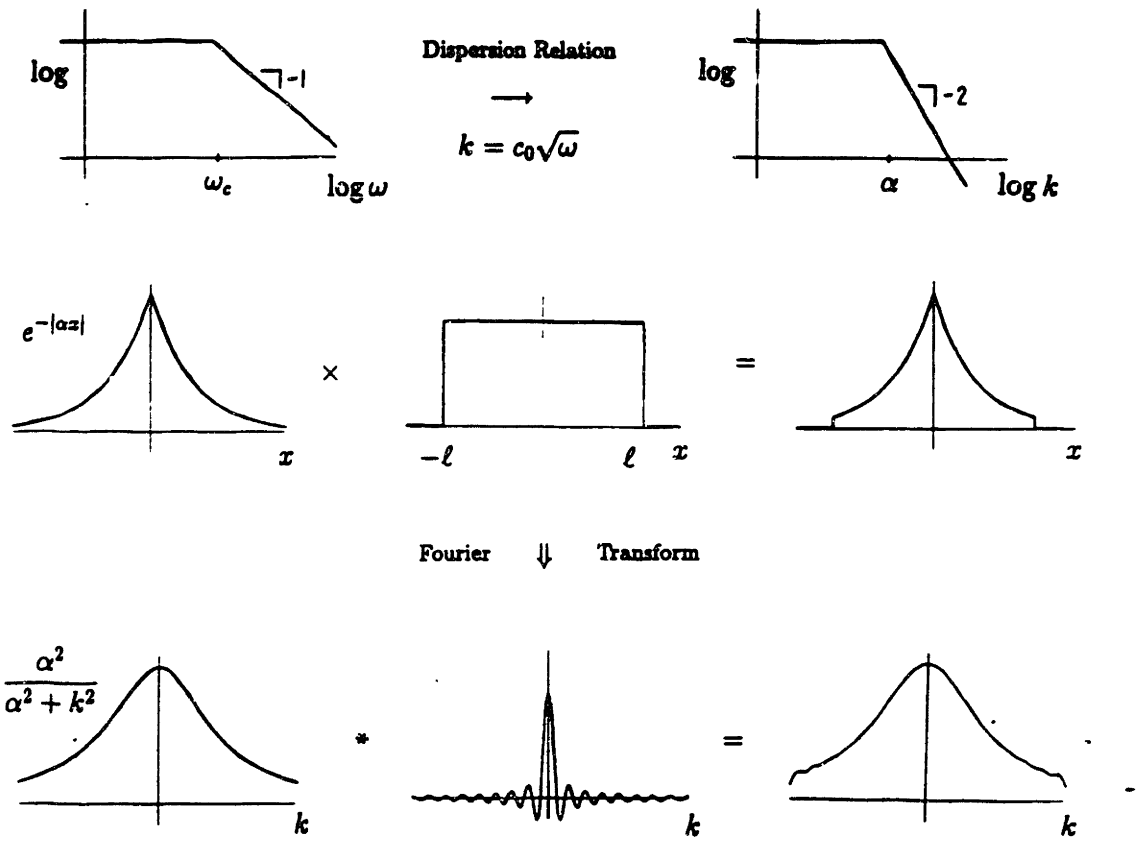

Figure 4.5: Exponential sensor design.

the convolution of two wavenumber functions. We see some leakage is introduced by the windowing operation; the desired wavenumber response is convolved with a sinc function rather than the dirac delta function which corresponds to an infinite "window". As the sinc function has negative sidelobes, we should not be surprised to find the actual sensor's wavenumber response includes some sign reversals. The dispersion relation can be used again to obtain the temporal frequency response of our exponential sensor. The analytical derivation associated with this figure will now be carried out somewhat more slowly.

The sensor dynamics, given the combination of a LHP pole and a RHP pole needed to achieve rolloff without phase lag, are of the form

$$\bar{u}(0,s) = \frac{-\omega_c}{s-\omega_c}\frac{\omega_c}{s+\omega_c}u(0,s) \tag{4.9}$$

where $\bar{u}(0,s)$ is the temporal Laplace transform of the output of a spatial filter centered

at $x = 0$, $u(0,s)$ is the transform of a particular structural degree of freedom at $x = 0$ and ω_c is the corner frequency of the distributed sensor. We wish to determine the spatial weighting function needed to obtain such sensor dynamics.

Spatial and temporal variables are related through the dispersion relation. This depends on the structural medium in which the wave exists. We shall first investigate the case of a uniform rod.

4.4.1 The Uniform Rod

Equation (4.5) gave the rod's dispersion relation for the Fourier variables k and ω. There is a corresponding relation for the Laplace variables p and s

$$p^2 = \frac{\rho}{E}s^2 = c_0^2 s^2 \tag{4.10}$$

where $1/c_0$ is the speed of sound in the rod. Substituting this dispersion relation for the Laplace variable in Eq. (4.9) yields

$$\bar{u}(0,s) = \frac{-c_0\omega_c}{p - c_0\omega_c}\frac{c_0\omega_c}{p + c_0\omega_c}u(p,0) \tag{4.11}$$

We know that the inverse Laplace transform of $1/(p+\alpha)$ is $e^{-\alpha x}$ for $x \geq 0$ [117], so the spatial weighting function decays exponentially in both the positive and negative x directions. Defining the scale length as the length required for a function to decay by a factor of one neper (e^{-1}), we see the scale length of the weighting function is $1/c_0\omega_c$. The attenuation factor α is the inverse of the scale length.

To demonstrate that this spatial weighting function produces rolloff without phase lag, we must evaluate the sensor equation:

$$\bar{u} = \frac{\alpha}{2}\int_{-\infty}^{\infty} u(x,\omega)e^{-\alpha|x|}\,dx \tag{4.12}$$

This calls for an expression for $u(x,\omega)$. The governing partial differential equation for a rod is

$$EA\frac{\partial^2 u(x,t)}{\partial x^2} - \rho A\frac{\partial^2 u(x,t)}{\partial t^2} = 0 \tag{4.13}$$

As there are two roots of the dispersion relation, Eq. (4.5), there are two wave modes supported at each frequency, one leftward propagating and one rightward propagating:

$$u(x,\omega) = u_l(\omega)e^{ikx} + u_r(\omega)e^{-ikx} \tag{4.14}$$

Substituting these wave modes into the sensor equation, Eq. (4.12), yields

$$\bar{u} = \frac{-(\alpha/c_0)^2}{(s-\alpha/c_0)(s+\alpha/c_0)}\left[u_l(\omega) + u_r(\omega)\right] \tag{4.15}$$

Based on Eq. (4.14), note that the point displacement sensor at $x = 0$ will observe

$$u_c = u(0,\omega) = u_l(\omega) + u_r(\omega) \tag{4.16}$$

Combined with Eq. (4.15), this shows that the output of a distributed sensor with an exponentially decaying spatial weighting function will be a filtered version of the signal from a point sensor located at the rod's midpoint. In this case, the filter consists of a second-order rolloff without any phase lag. A problem with this scheme is that the sensor, and the structure, has to extend from $+\infty$ to $-\infty$.

The first step in making this analysis more realistic is to use a finite length rod. The unit rod used to demonstrate the modal sensor in Section 4.3.1 can be used here too (Fig. 4.2). Given an applied force on the left end of the rod, the expressions for the displacement at a general point, Eq. (4.4), and at the midpoint of the rod, Eq. (4.7), are still valid.

Now add a finite length sensor to the structure. The sensor need not cover the entire rod: let the rod be of length L and let the sensor be of length 2ℓ. This corresponds to the windowing operation described earlier. The sensor is centered about $x = 0$. The sensor equation is now integrated between $\pm\ell$ rather than $\pm\infty$.

$$\bar{u} = \frac{\alpha}{2(1-e^{-\alpha\ell})}\int_{-\ell}^{\ell} u(x)e^{-\alpha|x|}\,dx \tag{4.17}$$

The constant in front of the integral gives the distributed sensor the same low frequency gain as the point sensor. Carrying out the integration, using Eq. (4.4) for $u(x)$, the

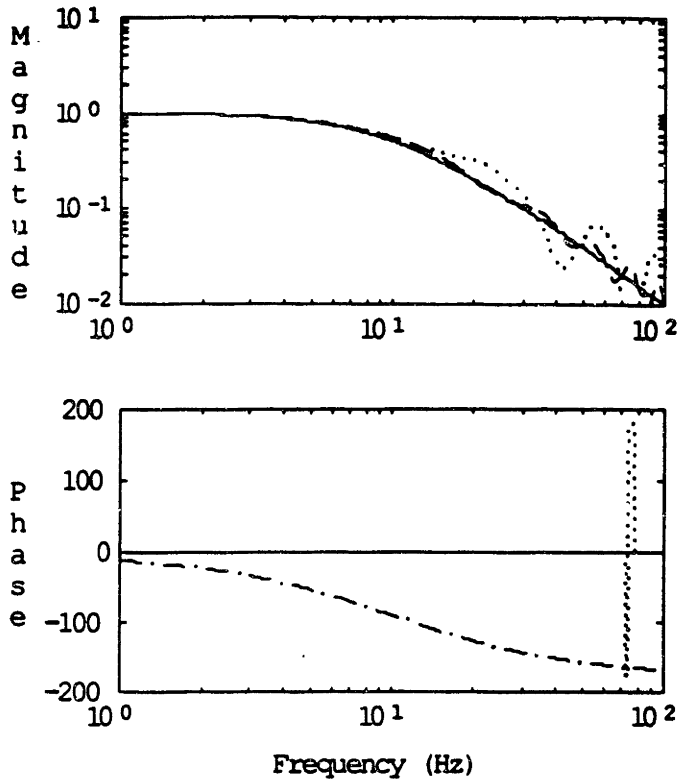

Figure 4.6: Transfer function from displacement to exponential sensor output, and transfer function from displacement to output of double real pole temporal filter. Mounted on a rod.

transfer function from the applied force to the exponential sensor output can be determined:

$$\frac{\bar{u}}{F} = \frac{1}{ikEA}\frac{\xi}{1-\xi^2}\left(\frac{\alpha - e^{-\alpha\ell}[\alpha\cos(k\ell) + k\sin(k\ell)]}{1-e^{-\alpha\ell}}\right)\left(\frac{\alpha}{k^2+\alpha^2}\right) \qquad (4.18)$$

The transfer function from a point measurement at the center of the rod to the output of a exponential sensor is shown in Fig. 4.6. Three different sensor lengths were used for this figure. The solid curve is the transfer function for a sensor which covers the entire length of the rod ($\ell = 0.5$ m), the dashed curve is for a sensor which covers 10% of the rod ($\ell = 0.05$ m) and the dotted curve is for sensor which covers 6% of the rod ($\ell = 0.03$ m). All three sensors were designed to have a corner frequency of 10 Hz. Since $c_0 = 1$ sec/m, the corresponding attenuation factor, $\alpha = 1/c_0\omega_c$, is 62.83 m^{-1}. The inverse of this is the scale length: 0.016 m.

The factor $\alpha\ell$ indicates *half* the number of scales lengths included in the sensor, as the length of the sensor is 2ℓ. But the sensor is symmetric about $x = 0$, so $\alpha\ell$ characterizes the sensor better than $2\alpha\ell$. This factor gives a good indication of how serious truncation errors will be, with the errors becoming less significant as $\alpha\ell$ increases. In Fig. 4.6, the sensor which covers the entire rod has a clearly visible second-order rolloff, as predicted by the infinite domain analysis above. There is also no phase lag. This sensor is 31 scale lengths long, while the other two sensors are 3.1 and 1.9 scale lengths long. Both of the smaller sensors display truncation-induced leakage in the magnitude of their transfer functions above 10 Hz, and the smallest one exhibits a sign change near 75 Hz. The leakage comes about because of the width of the sinc function's main lobe. The sinc function is the Fourier transform of the rectangular window. The Fourier transfor similarity theorem shows that this lobe will be narrower as the windowing function is broadened [117], so leakage will be less significant as more scale lengths are included in the sensor.

Figure 4.6 also suggests that truncation effects will become serious at lower frequencies as the number of scale lengths is reduced. This is apparent in Eq. (4.18) too. The term which is multiplied by $e^{-\alpha\ell}$ can be thought of as the error. The larger $\alpha\ell$ is, the larger k has to be for this term to be significant. So longer sensors look infinitely long at higher wavenumbers. The transition to sensors which are clearly finite is marked by the onset of sinusoidal oscillations. At wavenumbers much greater than α, *i.e.* at high frequencies, the sensor transfer function, Eq. (4.18), becomes

$$\frac{\bar{u}}{F} = \frac{-1}{ikEA}\frac{\xi}{1-\xi^2}\left(\frac{e^{\alpha\ell}\sin(k\ell)}{1-e^{-\alpha\ell}}\right)\frac{\alpha}{k} \tag{4.19}$$

The $1/k$ factor here, when combined with the dispersion relation for the rod, Eq. (4.5), indicates that the second-order rolloff of the infinite sensor has been reduced to a first-order rolloff by truncation effects. This is a worst-case rolloff, determined by the logarithmic slope of a line through the peaks of the leakage in the magnitude plot. So to avoid sign changes, which cause 180° phase reversals, and to maintain a high-order rolloff, it is necessary to provide a reasonable length sensor.

In the case of the smallest exponential sensor, the phase was disrupted by a sign change around 75 Hz. But compare the phase of this sensor with the result of passing a point sensor's output through a second-order temporal filter. As shown by the dash-dot curve in Fig. 4.6, significant phase lag has already been incurred by 5 Hz, and it approaches $-180°$ near 75 Hz. The improved phase characteristics offered by the distributed exponential sensor are clear.

4.4.2 The Uniform Bernoulli-Euler Beam

The demonstration of these sensors will be conducted on a uniform beam, so it is also important to analyse this structure. The partial differential equation for a uniform Bernoulli-Euler beam,

$$EI\frac{\partial^4 w}{\partial x^4} + \rho A\frac{\partial^2 w}{\partial t^2} = 0, \tag{4.20}$$

leads to the dispersion relations

$$k^4 = \frac{\rho A}{EI}\omega^2 = c_0^4\omega^2 \quad \text{and} \quad p^4 = -\frac{\rho A}{EI}s^2 \tag{4.21}$$

which support four wave modes (two propagating and two evanescent)

$$w(x,\omega) = w_{lp}(\omega)e^{ikx} + w_{le}(\omega)e^{kx} + w_{rp}(\omega)e^{-ikx} + w_{re}(\omega)e^{-kx} \tag{4.22}$$

Notice that the wavenumber k is now related to the square root of the frequency ω, whereas k had been a linear function of ω with the rod. The influence of this dispersive behavior will be observed below.

To investigate the behavior of an exponential sensor on a uniform beam, we evaluate the sensor equation using the exponential weighting function:

$$\bar{w}(\omega) = \frac{\alpha}{2}\int_{-\infty}^{\infty}\frac{\partial^2 w(x,\omega)}{\partial x^2}e^{-\alpha|x|}\,dx \tag{4.23}$$

The curvature of the beam as a function of X is given by

$$\frac{\partial^2 w(x,\omega)}{\partial x^2} = k^2\left(-w_{lp}(\omega)e^{ikx} + w_{le}(\omega)e^{kx} - w_{rp}(\omega)e^{-ikx} + w_{re}(\omega)e^{-kx}\right) \tag{4.24}$$

Substituting this into the sensor equation, Eq. (4.23), yields

$$\bar{w} = \frac{-\alpha^2 k^2}{k^4 - \alpha^4} \left\{ \left(k^2 - \alpha^2\right) \left[w_{lp} + w_{rp}\right] + \left(k^2 + \alpha^2\right) \left[w_{le} + w_{re}\right] \right\} \tag{4.25}$$

This can be related to a point curvature measurement at $x = 0$ by using Eq. (4.24) to obtain

$$\frac{\partial^2 w_c}{\partial x^2} = k^2 \left(-w_{lp} + w_{le} - w_{rp} + w_{re}\right) \tag{4.26}$$

So at wavenumbers much larger than α, *i.e.* at high frequencies, the distributed sensor's magnitude is related to the point sensor's magnitude by $1/k^2$.

While this corresponded to a second-order rolloff with a rod, the beam's wavenumber is proportional to the square root of the frequency, as shown by the dispersion relation, Eq. (4.21). So the rolloff in the frequency domain is only first order for an exponential sensor on a beam. For example, if no evanescent waves exist ($w_{le} = w_{re} = 0$), the transfer function from the output of the point sensor at the center of the beam to the output of the exponential sensor can be determined by substituting the dispersion relation, Eq. (4.21), for k in Eq. (4.25), giving

$$\frac{\bar{w}}{\partial^2 w_c / \partial x^2} = \frac{\alpha^2 / c_0^2}{\left(\sqrt{s} + i\alpha/c_0\right)\left(\sqrt{-s} - i\alpha/c_0\right)} \tag{4.27}$$

As was suggested by the limits of integration in Eq. (4.23), the analysis above was conducted in the infinite domain. The truncation effects are studied on a finite beam using a sensor of finite length, Fig. 4.7. Rather than a unit beam, the beam's properties are selected so as to correspond with the experimental arrangement used later. The length L is 7.32 m, the flexural rigidity EI is 31.1 N $\cdot$ m^2 and the mass per unit length ρA is 2.85 kg/m. In order to simplify the following analysis, pinned-pinned boundary conditions will be assumed, as there are no near fields associated with these. The excitation is assumed to be a moment M applied to the left end.

It can be shown [9] the curvature along the beam is given by

$$\frac{\partial^2 w(x,\omega)}{\partial x^2} = \frac{M}{EI} \left\{ \frac{\xi_p \left(e^{-ikx} - \xi_p^2 e^{ikx}\right)}{1 - \xi_p^4} + \frac{\xi_e \left(e^{-kx} - \xi_e^2 e^{kx}\right)}{1 - \xi_e^4} \right\} \tag{4.28}$$

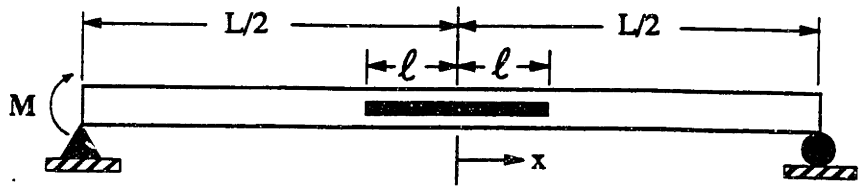

Figure 4.7: Pinned-pinned beam with a moment applied at the left end.

where

$$\xi_p = e^{-ikl/2} \quad \text{and} \quad \xi_e = e^{-kl/2}$$

The steady-state curvature at the center of the beam ($x = 0$) is given by

$$\frac{\partial^2 w_c(\omega)}{\partial x^2} = \frac{M}{EI} \frac{\xi_p \left(1 + \xi_e^2\right) + \xi_e \left(1 + \xi_p^2\right)}{\left(1 + \xi_p^2\right)\left(1 + \xi_e^2\right)} \tag{4.29}$$

The sensor equation is now integrated over a sensor of length 2ℓ.

$$\bar{w}(\omega) = \frac{\alpha}{1 - e^{-\alpha\ell}} \int_{-\ell}^{\ell} \frac{\partial^2 w(x,\omega)}{\partial x^2} e^{-\alpha|x|}\, dx \tag{4.30}$$

This gives the steady-state sensor output as a function of the applied moment M at the left end of the beam as

$$\bar{w} = \frac{M}{EI} \frac{1}{\left(1 + \xi_p^2\right)\left(1 + \xi_e^2\right)} \frac{\alpha}{1 - e^{-\alpha\ell}} \frac{\chi_1 + \chi_2}{\alpha^4 - k^4} \tag{4.31}$$

where

$$\begin{aligned} \chi_1 &= \xi_p \left(1 + \xi_e^2\right)\left(\alpha^2 - k^2\right)\left(\alpha - e^{-\alpha\ell}\left[\alpha\cos(k\ell) - k\sin(k\ell)\right]\right) \\ \chi_2 &= \xi_e \left(1 + \xi_p^2\right)\left(\alpha^2 + k^2\right)\left(\alpha - e^{-\alpha\ell}\left[\alpha\cosh(k\ell) + k\sinh(k\ell)\right]\right) \end{aligned}$$

The transfer function from the point curvature sensor to the exponential sensor can be calculated with Eqs. (4.29) and (4.31). Figure 4.8 shows the magnitude and phase of this transfer function for three different sensor lengths. The dashed curve is for a sensor with $\ell = 0.71$ m, the solid curve is for $\ell = 0.36$ m and the dotted curve is for $\ell = 0.18$ m. In all three cases, the sensor's corner frequency is 23 Hz, so the attenuation factor is $\alpha = 6.7\,\mathrm{m}^{-1}$, and the three sensors cover 4.8, 2.4 and 1.2 scale lengths, respectively.

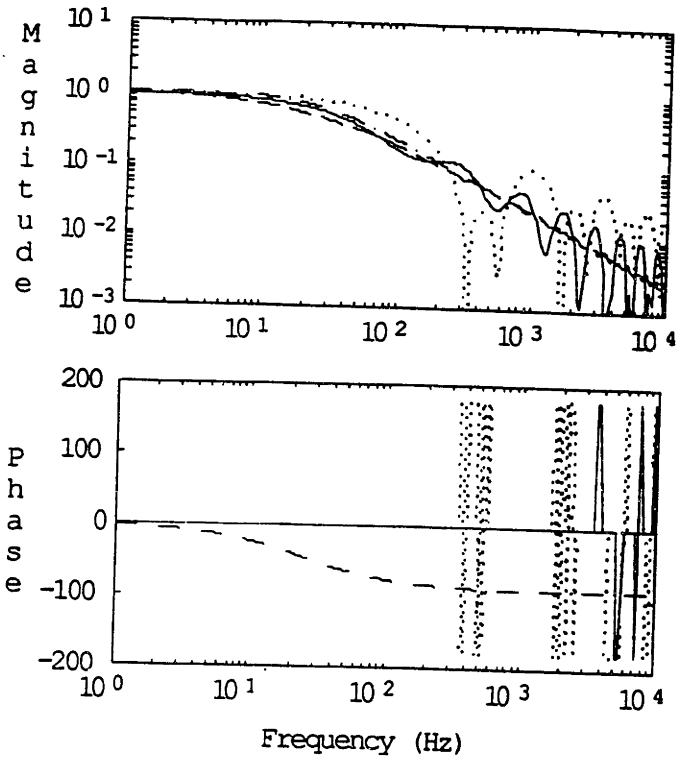

Figure 4.8: Transfer function from curvature to exponential sensor output, and transfer function from displacement to output of first order temporal filter. Mounted on a beam.

This figure shows that the magnitude starts to roll off at the corner frequency with a logarithmic slope of -1. But there is no phase lag associated with this rolloff; the temporal filter (the dash-dot curve) which achieves the same first-order rolloff already has 45° of phase lag at the corner frequency.

The growing sinusoid at higher frequencies (and fewer scale lengths) is an artifact of the truncation of the distributed sensor. Notice in Eq. (4.31) that χ_1 contains a term which grows as a linear function of wavenumber k. For k much larger than α, this equation becomes

$$\tilde{w}\,|_{k\to\infty} = \frac{M}{EI}\frac{e^{-\alpha\ell}}{1+\xi_p^2}\frac{\xi_p \sin(k\ell)}{k} \tag{4.32}$$

So the magnitude rolls off as $1/k$ at higher frequencies; the dispersion relation converts this to a half-order temporal rolloff. As with the rod, this degraded rolloff is determined by the logarithmic slope of a line through the peaks of the truncation-induced sinusoid

in the magnitude plot.

The leakage effects behave in much the way they did on the rod: a sensor with fewer scale lengths will suffer from leakage at a lower frequency. Eventually, the leakage causes a sign change—the sine term in Eq. (4.32) will be negative for some wavenumber. The phase then shifts by 180° periodically because of the sinusoid. Most control systems would be hard-pressed to handle the sharp phase transitions, so the exponential sensor must incorporate "enough" scale lengths to ensure the magnitude of the sensor's transfer function has dropped enough to gain-stabilize the system before the onset of these sign changes.

The exponential sensor offers the unusual combination of magnitude rolloff with zero phase lag over a broad frequency range. The order of the rolloff is reduced by truncation effects, and phase reversals occur at high frequencies. These problems can be lessened by using a long enough sensor. While control designers should welcome the lack of phase lag, they may not satisfied with the rolloff order—faster rolloff may be required if the modes of the structure are closely spaced.

4.5 Sinc Function Sensor

The design of the exponential sensor was not driven by anything unique about the exponential function. As always, the next step was to try to improve the performance of the filtering characteristics of the distributed sensor. So rather than starting the design process (Fig. 4.5) with a first- or second-order rolloff, we can start with an ideal lowpass filter (with no phase lag). The steps described in Section 4.4 were then repeated. This is portrayed in Fig. 4.9. The resulting spatial electrode pattern is a sinc function. Truncation effects prevent the piezo sensor from being an ideal lowpass filter, *i.e.* one that passes all frequencies below ω_c and blocks all those greater than ω_c.

Many of the equations presented in Section 4.4 can be carried directly over to the design of the sinc function sensor. The difference is in the spatial weighting function in

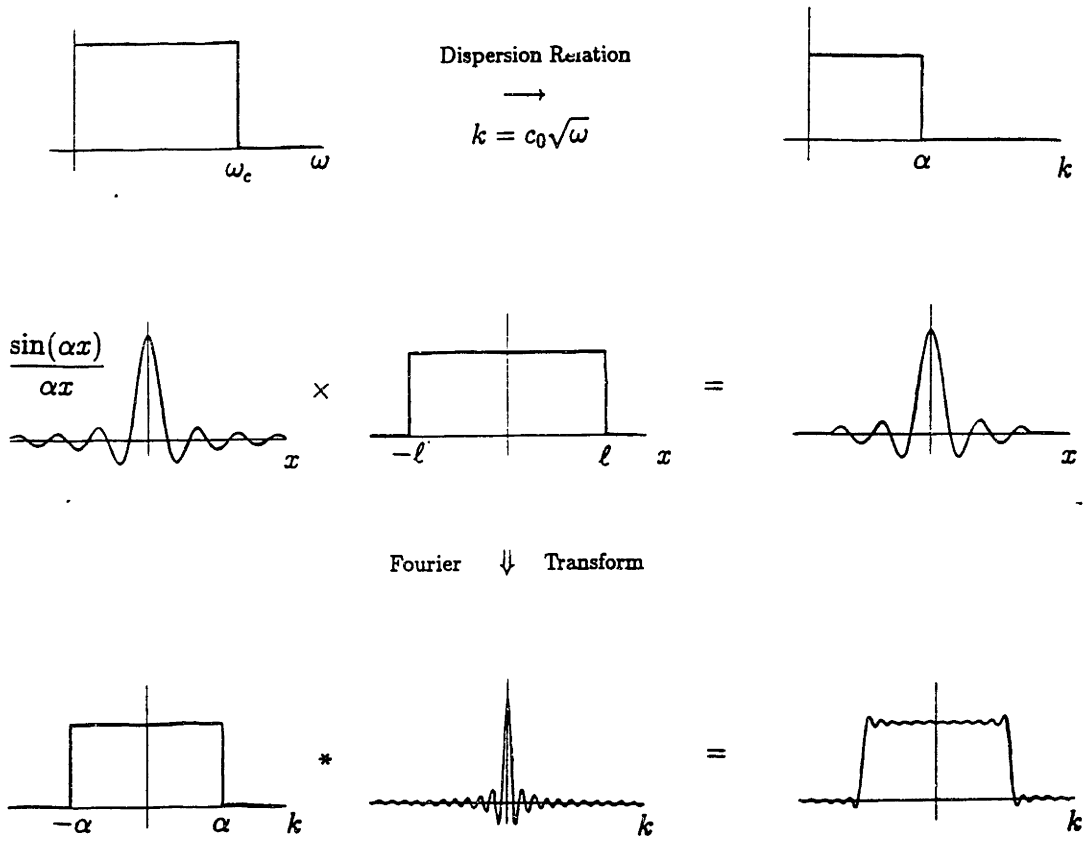

Figure 4.9: Sinc function sensor design.

the sensor equation. Let the effective electrode width be given by

$$b_{px}(x) = \frac{\sin(\pi\alpha x)}{\pi\alpha x} \tag{4.33}$$

Note that similar notation is used. While α is no longer an attenuation factor, it still has an important wavenumber interpretation: this is twice the corner wavenumber. The distance between nodes in the spatial domain is given by $1/\alpha$, but the main lobe is $2/\alpha$ wide (see Fig. 4.4). The distance between the nodes can be considered a scale length, so $\alpha\ell$ represents half the number of lobes in a sensor.

4.5.1 The Uniform Rod

The ideal filter characteristics are exhibited by an infinite sinc function sensor on an infinite rod. The displacement of the rod is still described by Eq. (4.15), so

$$\bar{u}(\omega) = \frac{\alpha}{2}\int_{-\infty}^{\infty}\left(u_l(\omega)e^{ikx} + u_r(\omega)e^{-ikx}\right)\frac{\sin(\pi\alpha x)}{\pi\alpha x}\,dx \tag{4.34}$$

If the rightward and leftward travelling wave mode amplitudes are equal, *i.e.* $u_l = u_r = u(\omega)$, the sensor output is given by

$$\bar{u}(\omega) = \frac{1}{2}u(\omega)\left[1 - \mathrm{sgn}(k - \alpha/2)\right] \tag{4.35}$$

This sensor has a flat response for wavenumbers below $\alpha/2$ has no response above this point. There is no phase lag associated with the infinite sensor. This sensor would be invaluable in many structural control applications. But the truncation effects must be considered.

Using the free-free rod again, the transfer function from the force applied at the left end of the rod to the output of a sinc function sensor is found by evaluating

$$\frac{\bar{u}}{F} = \frac{1}{ikEA}\frac{\alpha}{2}\left(\frac{\xi}{1-\xi^4}\right)\int_{-\ell}^{ell}\left(\xi^2 e^{ikx} + e^{-ikx}\right)\frac{\sin(\pi\alpha x)}{\pi\alpha x}\,dx \tag{4.36}$$

The solution of this integral is an infinite series, so Eq. (4.36) was evaluated numerically.

Figure 4.10 shows the magnitude and phase of the transfer functions from the displacement of the rod's midpoint to the output of the truncated sinc function sensor

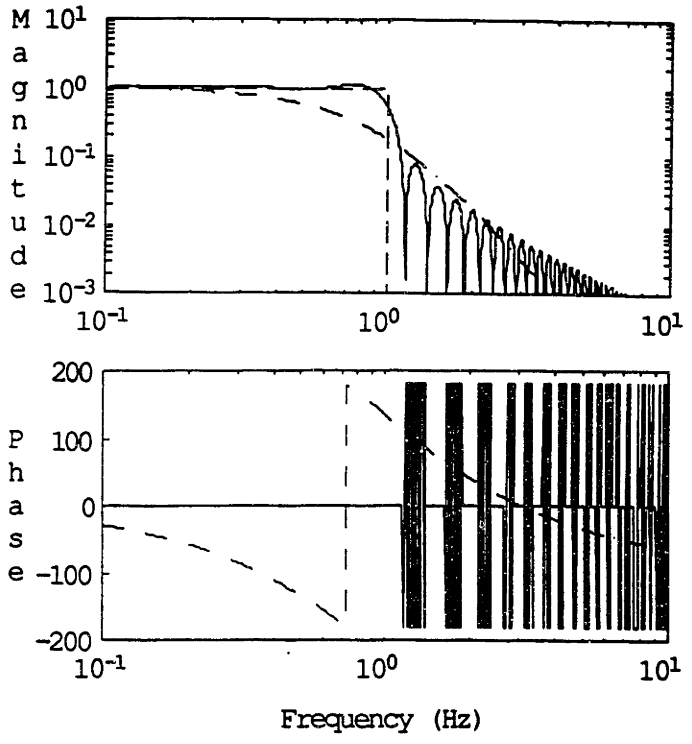

Figure 4.10: Transfer function from displacement to sinc function sensor output, and transfer function from displacement to output of fifth-order temporal filter. Mounted on a rod.

(solid curve) and to the ideal infinite extent sinc function sensor (dashed curve). The rod was lengthened to $L = 16\pi$ m to lower the frequencies. Notice that each sidelobe brings about a sign change, but the magnitude has attenuated about a decade before the first phase shift occurs. If more scale lengths are included, the rolloff becomes sharper.

It is difficult to assign an order to this rolloff, as it varies with frequency. For comparitive purposes, the transfer function from the midpoint displacement to the ouput of a temporal filter is shown in Fig. 4.10. The filter consisted of five real poles at $s = -6.283$ rad/sec. Note the large phase lag associated with this temporal filter.

4.5.2 The Uniform Bernoulli-Euler Beam

Carrying out the by-now-familiar series of operations and making use of Eq. (4.24) to evaluate the strain, the sensor equation is

$$\tilde{u} = \frac{\alpha}{2}\int_{-\infty}^{\infty} k^2\left(-w_{lp} + w_{le} - w_{rp} + w_{re}\right)\frac{\sin(\pi\alpha x)}{\pi\alpha x}\,dx \tag{4.37}$$

Assuming that there are no evanescent waves, *i.e.* $w_{le} = w_{re} = 0$, and that the propagating waves have equal amplitude, *i.e.* $w_{lp} = w_{rp} = w_p(\omega)$, then the solution is

$$\tilde{w} = -\frac{1}{2}w(\omega)\left[1 - \mathrm{sgn}(k - \alpha/2)\right] \tag{4.38}$$

This demonstrates that an ideal filter can be implemented with an infinite sinc function sensor on either an infinite rod or an infinite beam.

In the finite domain, the transfer function from the applied moment at the left end to the output of the truncated sinc function sensor is

$$\begin{aligned}\frac{\tilde{w}}{M} &= \frac{1}{EI}\frac{\xi_p}{1-\xi_p^4}\frac{\alpha}{2}\int_{-\ell}^{\ell}\left(e^{-ikx} - \xi_p^2 e^{ikx}\right)\frac{\sin(\pi\alpha x)}{\pi\alpha x}\,dx \\ &\quad + \frac{1}{EI}\frac{\xi_e}{1-\xi_e^4}\frac{\alpha}{2}\int_{-\ell}^{\ell}\left(e^{-kx} - \xi_e^2 e^{kx}\right)\frac{\sin(\pi\alpha x)}{\pi\alpha x}\,dx\end{aligned} \tag{4.39}$$

This too must be evaluated numerically.

Figure 4.11 shows the magnitude and phase of the transfer functions from the output of a point strain sensor at the beam's midpoint to the output of the truncated sinc function sensor (solid curve) and to the ideal infinite extent sinc function sensor (dashed curve). Notice that the sidelobes still cause phase problems. As mentioned above, the rolloff cannot be quantified easily, but qualitatively the rolloff here does not seem as great as the rolloff of the rod. Given the difference between the dispersion relations of the rod and the beam, this is to be expected.

The sinc function sensor has better rolloff than the exponential sensor, but the sign changes occur much closer to the corner frequency, which doesn't allow much room to gain-stabilize the system. Another way to handle this problem is to eliminate the

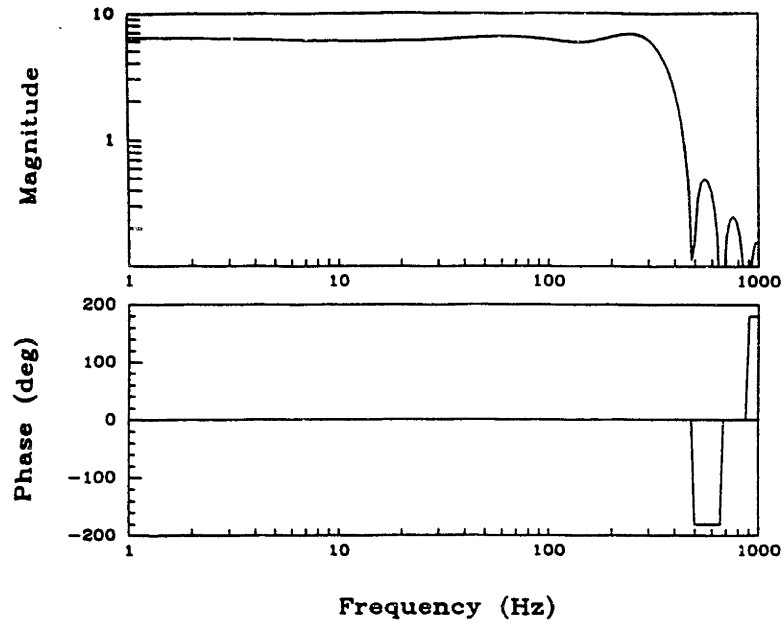

Figure 4.11: Transfer function from curvature to sinc function sensor output. Mounted on a beam.

sign changes. Then we would have a sensor with high-order rolloff and no phase lag whatsoever.

This is not as difficult as it might seem. The sign changes are due to the rectangular window which is applied to the infinite spatial weighting function to make it possible to implement the sensor. This is merely the simplest window, not the only one. Many windows have been developed for various signal processing applications. Most represent an optimal method of concentrating the window around $\omega = 0$ in the frequency domain. Consider the examples shown in Fig. 4.12 [118]: the main lobe and the side lobes are modified in various ways, but most windows also have negative regions in the frequency domain. Two exceptions are the Bartlett and Parzen windows, which remain positive at all frequencies. The Parzen has a wider main lobe, which is a drawback—we are trying to approximate the dirac delta function that arises in the infinite domain analysis. So we will examine the effect of using a Bartlett window on a sinc function sensor mounted on a beam.

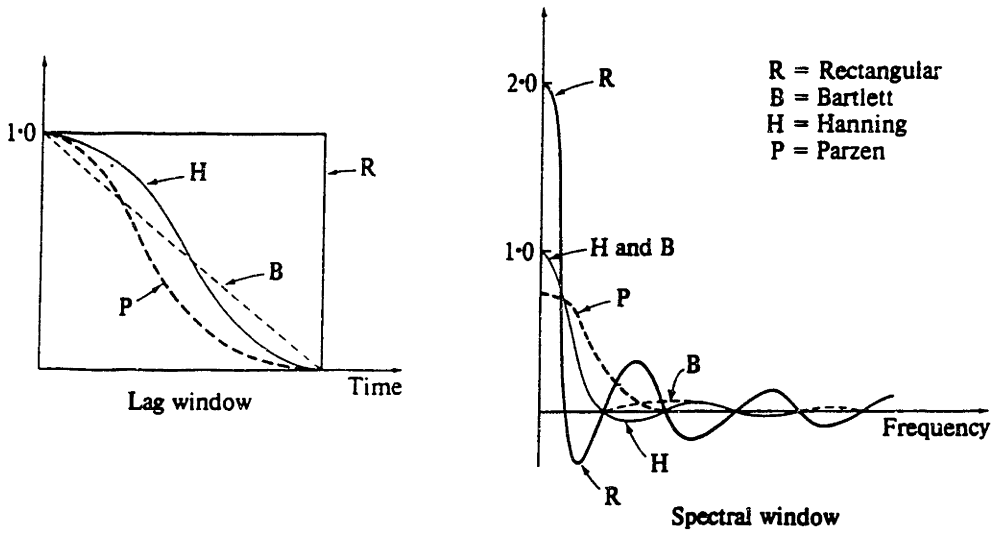

Figure 4.12: Various windows in time and frequency domains.

If we make the Bartlett window—really just a triangle—of the same width as the rectangular window, the Fourier transforms of the Bartlett window is $\text{sinc}^2 k$ and the transform of the rectangular window is $\text{sinc}(2k)$. Note that the Bartlett window results in a wavenumber response which is twice as broad as that from the rectangular window. This has a smoothing effect on the final frequency domain response. There are no sign changes because the sinc function is squared, ensuring that this part of the wavenumber-domain convolution is always positive.

The Bartlett window adds another term to the spatial weighting function, which changes the physical shape of a sinc function sensor as shown in Fig. 4.13. The sensor equation, Eq. (4.39), becomes

$$\begin{aligned}\frac{\bar{w}}{M} &= \frac{1}{EI}\frac{\xi_p}{1-\xi_p^4}\frac{\alpha}{2}\int_{-\ell}^{\ell}\left(e^{-ikx}-\xi_p^2 e^{ikx}\right)\left(1-\frac{x}{\ell}\right)\frac{\sin(\pi\alpha x)}{\pi\alpha x}\,dx \\ &\quad + \frac{1}{EI}\frac{\xi_e}{1-\xi_e^4}\frac{\alpha}{2}\int_{-\ell}^{\ell}\left(e^{-kx}-\xi_e^2 e^{kx}\right)\left(1-\frac{x}{\ell}\right)\frac{\sin(\pi\alpha x)}{\pi\alpha x}\,dx \qquad (4.40)\end{aligned}$$

This was evaluated numerically to compare it to the rectangular window.

The transfer function from the point strain sensor to the sinc function sensor is shown in Fig. 4.14. Two sinc function sensors are shown; they are both of equal length, but one uses a rectangular window (solid curve) and the other uses a Bartlett window (dashed

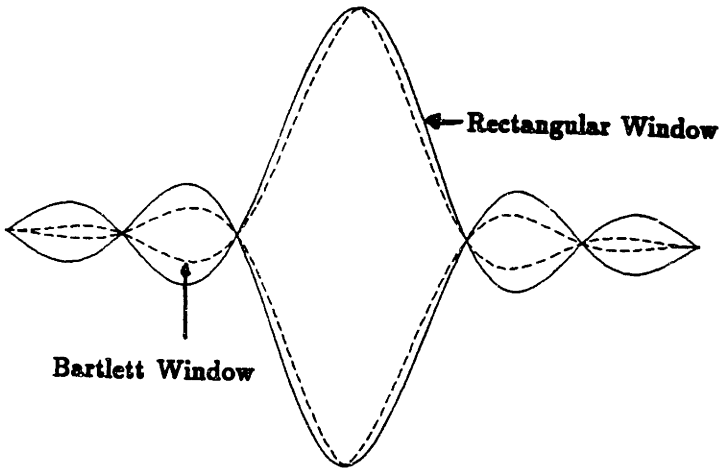

Figure 4.13: Effect of Bartlett window on the shape of a sinc function sensor.

curve). Note the smoothness caused by the Bartlett window, not only across the side lobes, but near the edge of the main lobe, too. The phase remains zero for the entire frequency range, indeed, it would so for any frequency range.

The smoothness of the sinc function sensor with Bartlett windowing is not a drawback. The lobe structure created by the rectangular windowing is fairly sensitive to small changes in the spatial weighting function, making it difficult to try to actually use the deep zeros as notch filters. The idea of a worst-case rolloff, introduced above with the truncated exponential sensor, is somewhat similar to this smoothing, although it did not actually change the frequency response above.

When a Bartlett function is used for truncation, the sinc function sensor seems like a promising sensor for structural control applications, as it provides high-order rolloff without phase lag. Even with the rectangular window, the sinc function sensor can be useful if the system can be gain-stabilized before being subjected to the 180° phase reversals of the sidelobes.

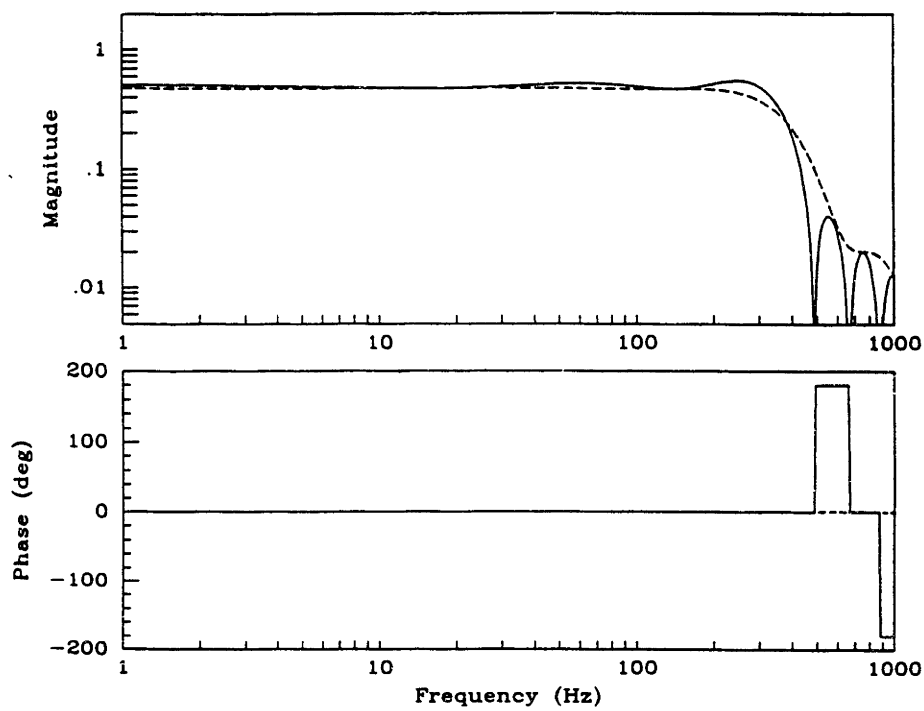

Figure 4.14: Transfer function from point strain sensor to sinc function sensor. Rectangular window (solid) and Bartlett window (dashed).

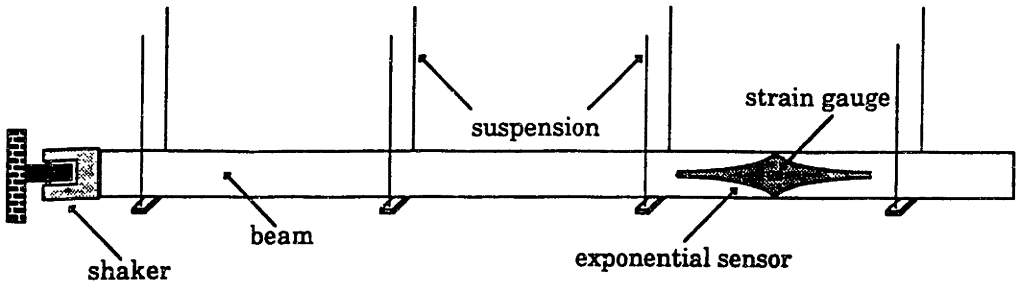

Figure 4.15: Beam set-up.

4.6 Experimental Demonstration

The exponential and sinc function sensors discussed above seem like important contributions to the toolbox of sensors available to a control system designer. Their combination of magnitude rolloff and constant phase cannot be achieved with regular point sensors, even after temporally filtering the output of these sensors. But before the spatially distributed sensors can be of any use to a control engineer, they have to be demonstrated experimentally. This section presents the manner in which the sensors were made, how they were tested and a discussion of the results.

4.6.1 Experimental Arrangement

The tests were conducted on a 7.32 m brass beam, composed of four 1.8 m sections bolted together end to end and suspended by six pairs of cables (Fig. 4.15). The beam was 0.10 m wide, 3.175 mm thick, had a flexural rigidity EI of 31.1 $\mathrm{N \cdot m^2}$ and a mass per unit length ρA of 2.85 kg/m. This beam can be modelled as a pinned-free Bernoulli-Euler beam up to frequencies of about 1 kHz.

Two distributed piezoelectric sensors were mounted on the beam. The exponential sensor was mounted 1.35 m from the free end of the beam, and the sinc function sensor was mounted 2.46 m from the free end. Rectangular windows were used for both sensors, and they were both symmetric with respect to a horizontal and a vertical centerline (Fig. 4.16). They were mounted on the centerline of the beam. Further details can be

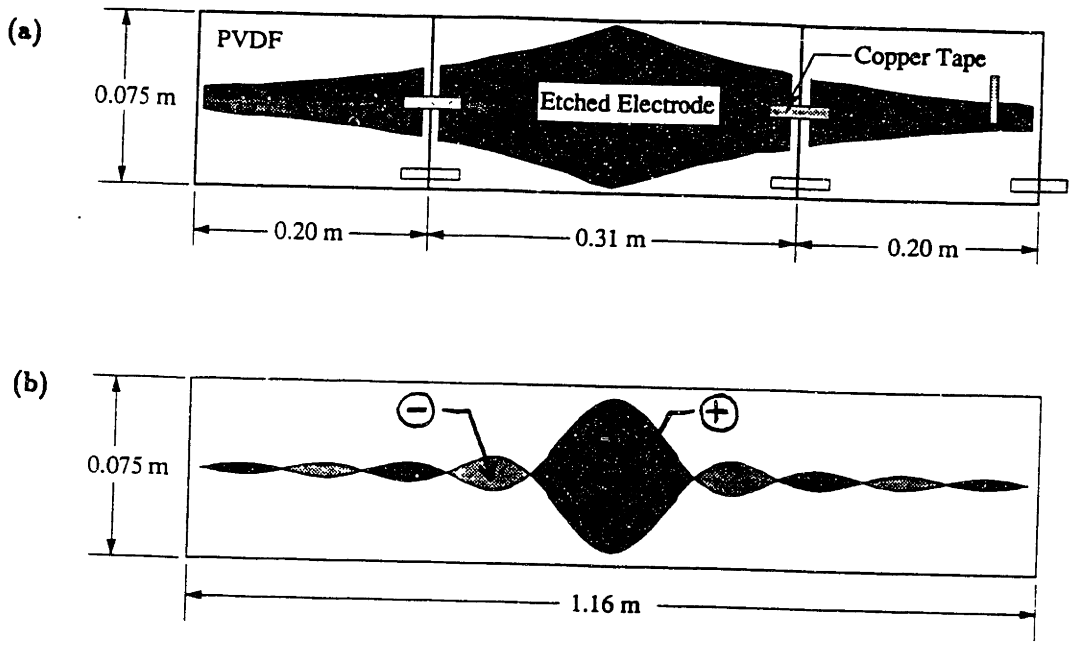

Figure 4.16: Electrode patterns: (a) exponential sensor; (b) sinc function sensor.

found in Table 4.1.

Strain gauges were mounted on the opposite side of the beam—one was placed at the centerpoint of each PVDF sensor. Foil gauges with a resistance of 120 Ω and a gauge factor of 2.050 were used.

The strain gauge signal was conditioned with a standard quarter-bridge arrangement. A buffer circuit (Section 2.4.4) was used to condition the PVDF sensors' signals.

Table 4.1: Sensor details

	Exponential Sensor	Sinc Function Sensor
Electrode Pattern	$e^{-\alpha\|x\|}$	$(\sin(\pi\alpha x))/(\pi\alpha x)$
	$\alpha = 6.7\,\mathrm{m}^{-1}$	$\alpha = 8.6\,\mathrm{m}^{-1}$
Corner Frequency	23 Hz	386 Hz
Width at $x = 0$	0.075 m	0.075 m
Sensor Length	0.71 m	1.16 m
No. of Segments	3	9

The exponential sensor was the smaller of the two sensors, so it would have the lower capacitance (40 nF). The first natural frequency of the beam was around 1 Hz, so the highpass corner frequency introduced by the film's capacitance should be placed at least a decade below 1 Hz. Using a buffer circuit with an input impedance of 66 MΩ resulted in a $1/RC$ corner frequency of 0.06 Hz for the exponential sensor and less for the sinc function sensor.

To help eliminate noise, the sensors were grounded to the beam, as was the shielded cable used for the strain gauges.

4.6.2 Sensor Fabrication

The sensors were made of 52 μm thick KYNAR piezo film with nickel/copper vapor-deposited electrodes. The properties of this film and transducer manufacture details were provided in Chapter 2. The spatial weighting functions described above were realized by spatially shaping the film's electrodes (see Fig. 4.16). The shaping was done by means of the ferric chloride etching technique described in Section 2.4.1. Other fabrication details include the use of spray adhesive and layers of Mylar to bond the sensors to the beam, and the use of conductive-adhesive backed copper tape to make all electrical connections. The ease with which these connections could be made and tested was more important than longterm reliability in this case.

Both sensors required several segments. The segment length was constrained by the size of the piezo film sheets: 0.30 m by 0.15 m. The sinc function sensor's segments were as long as a lobe: 0.116 m for the side lobes and 0.232 m for the main lobe. The width of the sensors was scaled to be half the width of a sheet, *i.e.* 0.075 m.

The lobes of the sinc function sensor alternate in sign (Fig. 4.16), so segments with a negative effective width were required. These segments were made the same way the Mode Two sensors were made in the last chapter, namely, the film was turned over before wiring the segment into the sensor, thereby giving it a negative polarity with respect to the rest of the sensor.

4.6.3 Experimental Procedure

The objective of these tests was to verify the spatial filtering characteristics of these sensors. So the transfer functions presented in Figs. 4.7 and 4.10 were to be measured.

There was a PMI torque motor mounted at the pinned end of the beam. This was driven using a power amplifier and the signal generator in a Tektronix 2630 Fourier Analyzer. Band-limited pseudo-white noise was genreated by the Fourier Analyzer, providing a moment excitation to the beam. The signal generator voltage level was such that a root-mean-square torque of $0.0794\,\mathrm{N}\cdot\mathrm{m}$ was applied in each test.

Three channels of data were collected with the Fourier Analyzer during each test: the excitation voltage, the strain gauge signal and the distributed sensor signal. Transfer functions were calculated from moment to strain gauge signal, from moment to distributed sensor signal and from strain gauge signal to sensor signal. The data was taken over a frequency band from 1 Hz to 1 kHz. This showed several structural resonances below the corner frequency of the exponential sensor (23 Hz), and it showed the distributed sensor behavior after the sinc function corner frequency (386 Hz).

4.6.4 Discussion of Results

Exponential Sensor

Figure 4.17 shows the magnitude and phase of the transfer function from the strain gauge signal to the exponential sensor signal. Examination of the coherence function (a ratio of cross-power spectra [119]) indicated that the two signals were poorly correlated at the sharp peaks in Fig. 4.17. These correspond to the low level signals obtained at the zeros of the transfer function from moment to either the exponential sensor signal or strain gage signal shown in Fig. 4.18. In order to highlight the general behavior of the sensor, the experimental transfer function was smoothed by taking a moving average of the experimental data.

Note the overall agreement with theory in Fig. 4.17. Below 100 Hz, the experimental

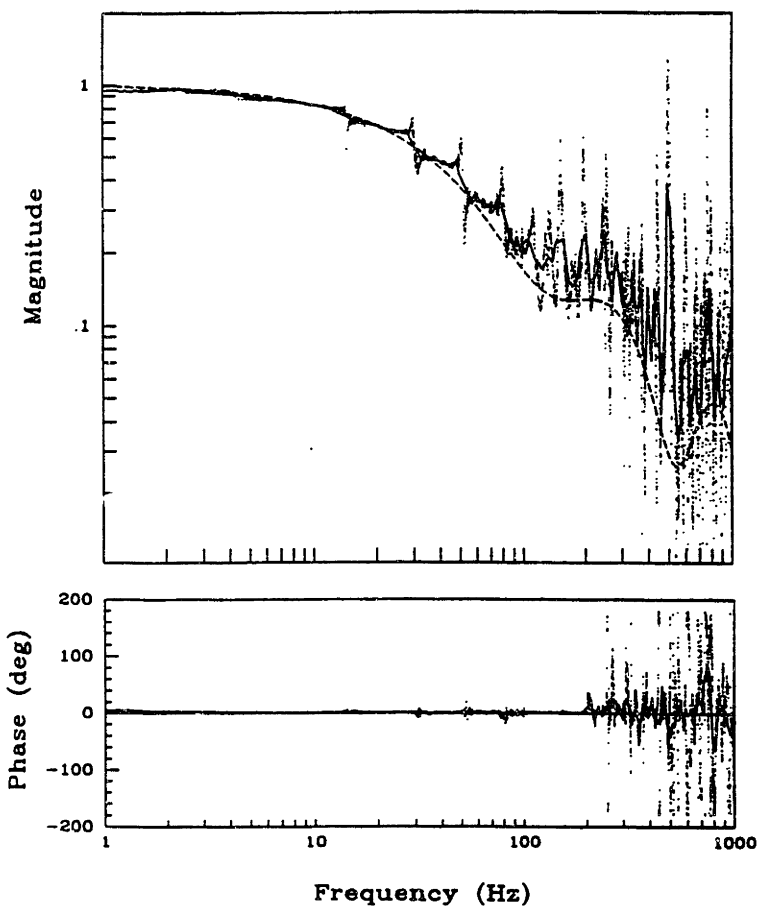

Figure 4.17: Transfer function between strain gauge and exponential sensor signals for three cases: predicted (dashed); actual (dotted) and smoothed (solid).

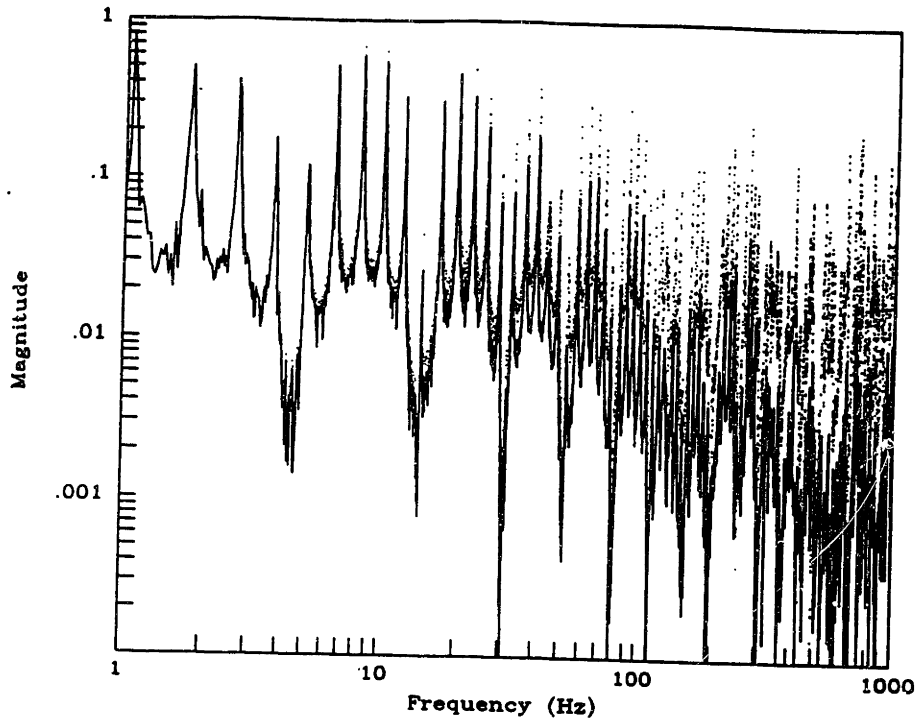

Figure 4.18: Transfer function from moment to strain gauge signal (dotted), and from moment to exponential sensor signal (solid).

data exhibits a roughly first order rolloff with a corner frequency of 23 Hz and no phase lag. As predicted in Fig. 4.7 for $\ell = 0.36$ m, the truncation effects become evident in the data above 100 Hz. The first significant phase transition, around 250 Hz, occurs after the magnitude has been attenuated by about one decade. Figure 4.18 shows almost perfect overlay of the two transfer functions below the corner frequency of 23 Hz and attenuation of the exponential sensor signal above this frequency.

Deviations between the data and theory are of two kinds. The first corresponds to the rapid fluctuation, with frequency, of the magnitude and phase. This could arise from several sources. As stated previously, the coherence was poor at these frequencies. This implies that either the strain gage or exponential sensor signals were below their noise floors. Alternately, the two sensor gains may not be linear with amplitude, or the assumption of a Bernoulli-Euler beam may be inappropriate at higher frequencies. Nonlinearity in amplitude could cause the two signals to differ significantly near the

poles or zeros where the transfer functions are changing rapidly. The introduction of torsion and plate modes in the beam could also affect the two sensors differently.

Two factors indicate that these spikes are of little concern. Detailed inspection of the two transfer functions in Fig. 4.18 revealed there was good agreement between the frequencies of the poles and zeros. In other words, the two sensors appear to be observing the same phenomenon. In addition, Fig. 4.18 verifies that the magnitude of the exponential sensor signal drops, and stays, below that of the strain gauge. Therefore, these spikes most likely result from poor signal to noise ratio near the zeros of the system.

The second kind of deviation corresponds to the observation that the magnitude of the experimental data is greater than that predicted at higher frequencies. This may be the result of a slower rolloff rate than predicted by the dispersion relation. An alternate explanation is that the actual and predicted corner frequencies are different causing the same rolloff as predicted but at higher frequency. These differences could be caused by modelling errors such as incorrectly identifying c_0. The theoretical predictions calculated c_0 based on the beam properties alone, *i.e.* $EI = 31.1\,N \cdot m^2$ and $\rho A = 2.85$ kg/m. An analysis of the composite beam could be carried out, but the adhesive layer is probably the one that changes the properties the most, and it is the hardest one to model.

Sinc Function Sensor

The data for the sinc sensor is presented in Figs. 4.19 and 4.20 in the same format as above.

Notice in Fig. 4.19 that the magnitude exhibits a roughly fifth order rolloff between 300 and 500 Hz. This is in good agreement with the predicted rolloff near 386 Hz (Table 4.1). As would be expected from the analysis, the first significant phase shift occurs at 500 Hz, after attenuation of one decade, at the first side lobe of the spatial filter. A couple of these truncation-induced lobescan be distinguished in the magnitude plot. The two 180 degree phase reversals at 520 Hz and 710 Hz support this observation.

Figure 4.20 shows almost perfect overlay of the two transfer functions below 300 Hz.

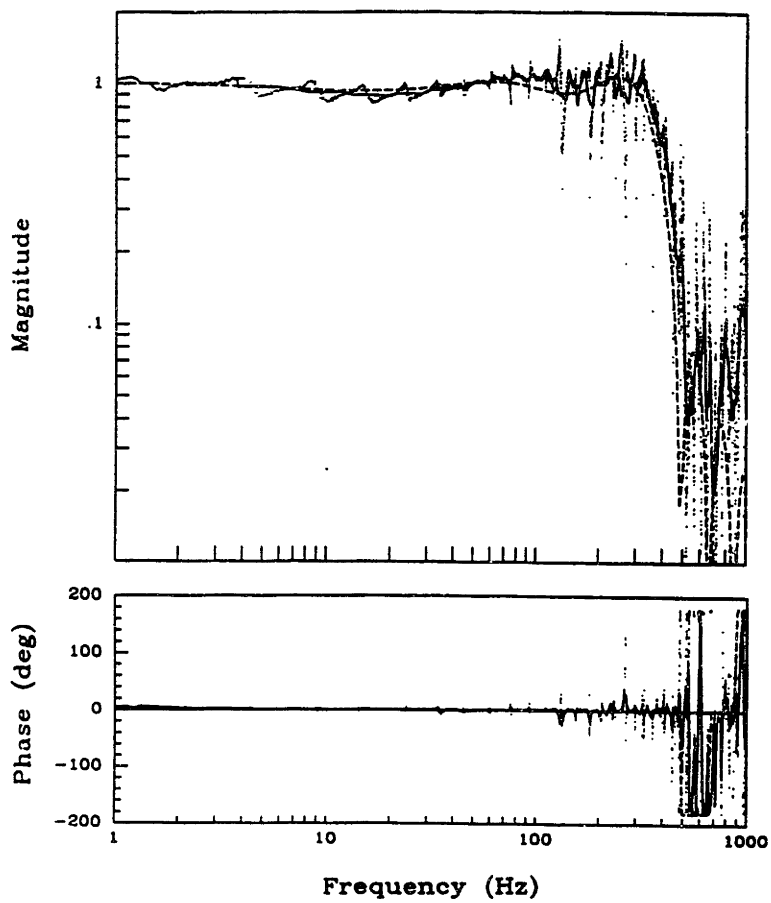

Figure 4.19: Transfer function between strain gauge and sinc function sensor signals for three cases: predicted (dashed); actual (dotted) and smoothed (solid).

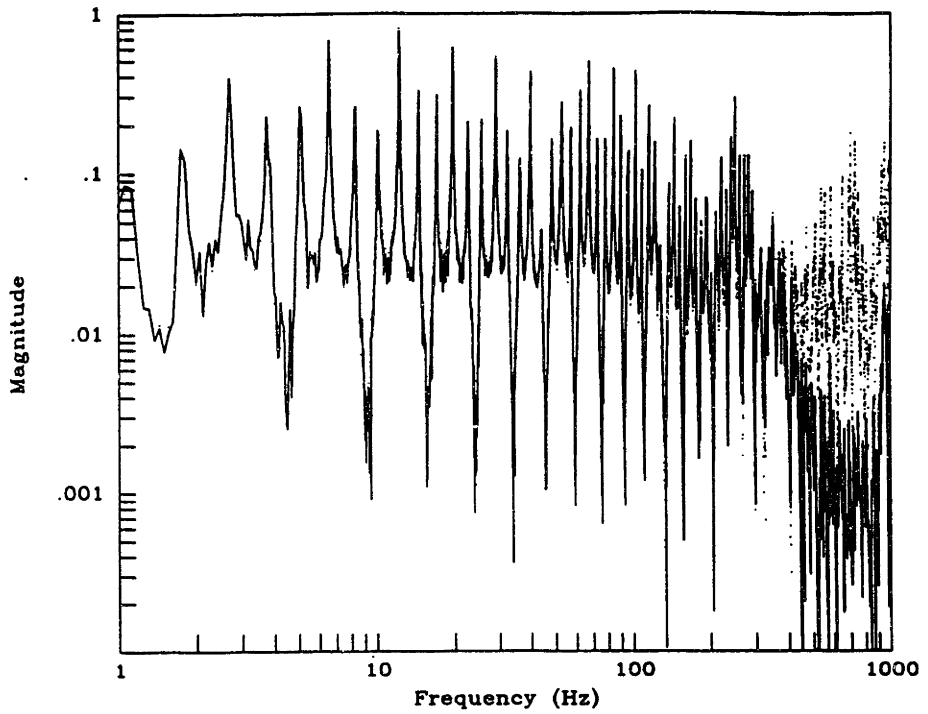

Figure 4.20: Transfer function from moment to strain gauge signal (dotted), and from moment to sinc function sensor signal (solid).

Above 300 Hz, the sinc function sensor signal attenuates rapidly with frequency.

When comparing the exponential and sinc function sensor data, note that the latter exhibits greater fluctuation in magnitude below the corner frequency of the sensor. This may result from the greater number of zeros in the transfer function of the sinc function sensor (compare Figs. 4.18 and 4.20). The two sensor transfer functions have different zeros because they are located at different positions on the beam. This indicates that a sensor located at the center would provide the best coherence because it has no zeros in its transfer function.

It may also be possible to improve the coherence of the data by preshaping the excitation signal. The results above used pseudo-white noise, so the noise was evenly distributed in a frequency band when it was left the signal generator. But this noise is filtered by the structure when measuring the transfer function from the strain gauge to the distributed sensors. If the autospectrum of the generated noise were shaped as the

inverse of Fig. 4.18 or 4.20, the strain gauge signal would be approximately constant at all frequencies. This could eliminate some of the noise floor problems, improving the coherence of the data.

4.7 Summary

Measurement of a structure's spatial deflection pattern can be used to generate sensor signals which possess dynamic characteristics that are beneficial to real-time structural control applications. By using the sensor shape as a spatial weighting function for the averaging of the distributed measurements, the sensor filters the spatial harmonics of the deflection pattern. Since these harmonics are uniquely related to temporal frequencies through that structural medium's dispersion relation, the resulting sensor signal becomes dynamically compensated. Since causality is not an issue in the spatial domain, the resulting dynamically compensated sensor signals can possess particular characteristics which are unobtainable through direct dynamic compensation. In particular, it was shown that magnitude rolloff could be achieved with no phase lag.

Two area-averaging sensors were implemented on a beam. The output closely matched that predicted by the analyses. The effect of truncating the sensors was quantified, suggesting that the effects could be shifted to higher frequencies by incorporating more scale lengths into the sensor. It was also shown analytically that the use of a Bartlett window to truncate the sensor would eliminate the sign changes that arise from other windows, especially the rectangular one. The use of a sinc function sensor truncated with a Bartlett window would produce a spatial filter which has high-order rolloff but has no phase lag. The use of such a sensor in a closed-loop structural control experiment is currently being studied.

Chapter 5

Conclusions and Recommendations

This work has shown that a wide variety of unusual characteristics can be imparted to distributed piezopolymer sensors, making them of great interest for structural control applications. Some of the particular findings of this thesis are as follows.

The material polyvinlyidene fluoride (PVDF) was found to be a good sensor for structural control applications because of its large piezoelectric stress coefficient ($g_{31} = 216\,mV \cdot /N$), its flexibility ($E = 2$ GPa) and its low density ($\rho = 1.8 \times 10^3\,kg/m^2 \cdot sec$). Additionally, it is quite easy to work with, with a wide variety of applicable fabrication techniques. The best results were achieved by using etching to shape the film's electrode wjile leaving a uniform layer of the polymer for bonding. Epoxy was preferable to other adhesives, and good electrical connections good be made with prepared copper strips and regular and conductive epoxy. Complicated conditioning electronics were not required; simple op amp circuits provided large signals that were relatively free of noise. While other researchers had made use of this material for structural control experiments, the material's versatility has not been fully exploited.

An application that had been demonstrated previously was modal sensors. These avoid the spatial aliasing problem of modal filters based on an array of discrete point sensors. Modal sensors are realized by shaping the width of the electrode proportional to the second derivative of the displacement mode shapes. Four modal sensors were

designed for the Large Space Manipulator at Martin Marietta during the course of this thesis. Two were designed for the first mode and two for the second mode. Each pair consisted of one fullwidth and one halfwidth sensor. Three of the sensors worked successfully, but one failed; this one was mounted underneath another fullwidth sensor, which could have caused the failure. Gains at the natural frequencies were determined experimentally. They showed the modal filtering aspects of these sensors. The off-design response was between 2% and 10% of the response to the design mode. The halfwidth sensor for mode two worked as well as the fullwidth one, so it is possible to avoid the experimental problems associated with layering the sensors. This does make the sensors sensitive to torsional modes, as they are no longer symmetric about the beam's centerline. While strain gauges could be placed at nodes of certain modes, making them unobservable, this left the other modes being observable. Modal sensors, on the other hand, made all modes, apart from the design mode, unobservable, or nearly so.

The modal sensors can also be interpreted as spatial filters. This response of a uniform (or rectangular) sensor was also considered from this perspective, revealing that the distributed sensor acts like a point sensor whose signal has been passed through a filter. This filter is implemented spatially, so noncausal dynamics can be realized. For example, second-order rolloff with no phase lag was achieved. The inverse Fourier transform revealed the appropriate sensor shape was an exponential function symmetric about $x = 0$. By analyzing a point sensor on a structure and filtering the response with the distributed sensor, it was found that a second-order temporal frequency rolloff was attained on the rod, while it was a first-order rolloff on the beam because of the dispersion relation. Truncation effects reduced this rolloff at high frequencies, and it introduced phase reverals. These effects could be shifted to higher frequencies by incorporating more scale lengths into the sensor. An attempt to implement an ideal lowpass filter resulted in a sinc function sensor. While this had higher-order rolloff, the general properties were the same as with the exponential sensor, namely the beam's rolloff was not as great as the rod's, and truncation decreased this rolloff and added phase reversals. Both of

these functions were truncated using a rectangular sensor; the truncation errors can be modified by using a Bartlett window. There are no longer any phase reversals, but the magnitude response is smoothed. These relations were experimentally verified for an exponential sensor and a sinc function sensor on a beam; both were truncated with a rectangular window. There was good agreement with theory, although problems with the sensors' noise floors were encountered at the zeros of the moment to strain transfer function. Another error was that the corner frequency was underestimated in both cases. This could have been due to a modelling error in the disperion relation.

There are several direct extensions of this work which could be pursued. The robustness of the modal sensors to variations in the boundary conditions could be studied in the Martin Marietta Large Space Manipulator by changing the tip payload. The modal sensors could also be used as part of a closed-loop modal control experiment. The use of a sinc function sensor in a closed-loop control experiment is currently being attempted. The sensor will be truncated with a Bartlett window to demonstrate the elimination of the sign changes.

We have demonstrated that some interesting sensor dynamics can be created through the use of spatially shaped distributed piezopolymer sensors. But fairly simple characteristics were added, although their combination was original. The next logical step would be to attempt more complicated sensor dynamics. For example, the noncausal compensators suggested by optimal power flow control could be incorporated into a distributed sensor. This would seem to require some design tools beyond Fourier transforms. It may be possible to interpret linear quadratic regualtor gains in such a way that these gains suggest the required spatial pattern. Wave sensors are another challenging application, possibly requiring the combination of distributed and point sensors to achieve the required directional sensitivity.

The sensors do not have to be part of a closed-loop feedback system to be useful. Modal sensors can be used to verify the accuracy of modal estimators, for example, or distributed sensors could be used as tools for identification. Because the temporal

frequency response of these sensors depends on the dispersion relation of the structure to which they are attached, it has been suggested they could be used to study the dispersion relations of complicated built-up structures not amenable to simple wave-type analyses.

References

Abbreviations of Journal Names

Abh. Gött.	Abhandlungen der Königlichen Gesellschaft der Wissenschaften zu Göttingen
AIAA J.	A.I.A.A. Journal
An. chim. phys.	Annales de chimie et de physique
Appl. Opt.	Applied Optics
Appl. Phys. Lett.	Applied Physics Letters
Bell Syst. Tech. J.	Bell System Technical Journal
Ber. Sächs.	Berichte über die Verhandlungen der Königlichen Sächsischen Gesellschaft der Wissenschaften zu Leipzig (mathematisch-physische Classe)
Bull. soc. min. Fr.	Bulletin de la société minéralogique de France
C.r.	Comptes rendus hebdomadaires des séances de l'académie des sciences
C.r. (Sov.)	Comptes rendus (Doklady) de l'académie des sciences de l'URSS
Chem. Abstr.	Chemical Abstracts
Dokl. Akad. Nauk SSSR	Doklady Akademiia Nauk SSSR
Electron. W.	Electronics Week
Ferroelectr.	Ferroelectrics
IEEE Control Syst. Mag.	I.E.E.E. Control Systems Magazine
Ind. Eng. Chem.	Industrial and Engineering Chemistry
Izv. Akad. Nauk SSSR	Izvestiia Akademiia Nauk SSSR (Physico-Mathematical Class)
J. Acoust. Soc. Am.	Journal of the Acoustical Society of America
J. Appl. Mech.	Transactions of the A.S.M.E., Journal of Applied Mechanics

J. Appl. Phys.	Journal of Applied Physics
J. Basic Eng.	Transactions of the A.S.M.E., Journal of Basic Engineering
J. Chem. Ed.	Journal of Chemical Education
J. Compos. Mater.	Journal of Composite Materials
J. Dyn. Sys. Meas. Contr.	Transactions of the A.S.M.E., Journal of Dynamic Systems, Measurement, and Control
J. Guid. Contr. Dyn.	Journal of Guidance, Control, and Dynamics, formerly Journal of Guidance and Control [1978–1981]
J. Opt. Soc. Am.	Journal of the Optical Society of America
J. Optim. Theory Appl.	Journal of Optimization Theory and Applications
J. phq.	Journal de physique, formerly Journal de physique théorique et appliquée [1872–1919]
J. Phys. Soc. Japan	Journal of the Physical Society of Japan
J. Robotic Syst.	Journal of Robotic Systems
Jpn. J. Appl. Phys.	Japanese Journal of Applied Physics
J. Sound Vib.	Journal of Sound and Vibration
KYNAR Appl. Not.	KYNAR Piezo Film Application Notes
Macromolec.	Macromolecules
Nachr. Gött.	Nachrichten von der Königlichen Gesellschaft der Wissenschaften zu Göttingen (mathematisch-physikalische Klasse)
Naturwiss.	Die Naturwissenschaften
Phys. Rev.	The Physical Review, 2nd Series
Proc. Phys. Soc.	Proceedings of the Physical Society, London
Trans. IECE Japan	Transactions of the I.E.C.E. of Japan
Trans. AIEE	Transactions of the A.I.E.E.

[1] J.J. D'Azzo and C.H. Houpis, *Feedback Control System Analysis and Synthesis*, 2nd ed., McGraw-Hill Book Company, New York, 1966, 824 pp.

[2] E.F. Crawley and J. de Luis, "Use of Piezoelectric Actuators as Elements of Intelligent Structures," *AIAA J.*, **25** (10), 1987, pp. 1373–1385.

[3] T. Bailey and J.E. Hubbard, Jr., "Distributed Piezoelectric-Polymer Active Vibration Control of a Cantilever Beam," *J. Guid. Contr. Dyn.*, **8** (5), Sept.-Oct. 1985, pp. 605–611.

[4] C.-K. Lee and F.C. Moon, "Laminated Piezopolymer Plates for Torsion and Bending Sensors and Actuators," *J. Acoust. Soc. Am.*, **85** (6), June 1989, pp. 2432–2439.

[5] T. Sato, H. Ishida and O. Ikeda, "Adaptive PVDF Piezoelectric Deformable Mirror System," *Appl. Opt.*, **19** (9), May 1980, pp. 1430–1434.

[6] S.E. Burke and J.E. Hubbard, Jr., "Active Vibration Control of a Simply Supported Beam Using a Spatially Distributed Actuator," *IEEE Control Syst. Mag.*, **7** (4), Aug. 1987, pp. 25–30.

[7] C.-K. Lee and F.C. Moon, "Modal Sensors/Actuators," *J. Appl. Mech.*, **57** (2), June 1990, pp. 434–441.

[8] L. Meirovitch and H. Baruh, "The Implementation of Modal Filters for Control of Structures," *J. Guid. Contr. Dyn.*, **8** (6), Nov.–Dec. 1985, pp. 707–716.

[9] D.W. Miller and A.H. von Flotow, "A Travelling Wave Approach to Power Flow in Structural Networks," *J. Sound Vib.*, **128** (1), Jan. 1989, pp. 145–162.

[10] D.W. Miller and S.R. Hall, "Experimental Results Using Active Control of Travelling Wave Power Flow," presented at 1989 ASME Winter Meeting, San Fransisco, CA, Dec. 11–15, 1989. To appear in *J. Guid. Contr. Dyn.*

[11] D.G. MacMartin and S.R. Hall, "An $\mathcal{H}_\infty$ Power Flow Approach to Control of Uncertain Structures," *Proc. of the 1990 American Control Conference*, San Diego, CA, May 23–25, 1990, pp. 3073–3080. To appear in *J. Guid. Contr. Dyn.*

[12] A.H. von Flotow and B. Schäfer, "Wave-Absorbing Controllers for a Flexible Beam," *J. Guid. Contr. Dyn.*, **9** (6), Nov.-Dec. 1986, pp. 673–680.

[13] W.G. Cady, *Piezoelectricity*, 2 vols. (revised ed. of McGraw-Hill ed., 1946), Dover Publications, Inc., New York, 1964, 822 pp.

[14] B. Jaffe, W.R. Cook, Jr. and H. Jaffe, *Piezoelectric Ceramics*, Vol. 3 of *Non-Metallic Solids*, J.P. Roberts and P. Popper, gen. eds., Academic Press Inc., London, 1971, 317 pp.

[15] S.D. Lang,"Bibliography on Piezoelectricity and Pyroelectricity of Polymers," *Ferroelectr.*

I.	1961–1980	**32** (1–4)	1981	pp. 191–245
II.	1980	**34** (4)	1981	pp. 239–251
III.	1980–1981	**45** (3–4)	1982	pp. 283–294
IV.	1981	**46** (1–2)	1982	pp. 51–60
V.	1981–1982	**47** (3–4)	1983	pp. 259–267
VI.	1982–1983	**61** (1–3)	1984	pp. 157–232
VII.	1984	**62** (3–4)	1985	pp. 259–307
VIII.	1984–1985	**67** (2–4)	1986	pp. 223–282
IX.	1985–1986	**74**	1987	pp. 109–206
X.	1986	**77**	1988	pp. 235–291
XI.	1986–1987	**88**	1988	pp. 259–332
XII.	1987–1988	**99**	1989	pp. 315–402
XIII.	1988–1989	**103**	1990	pp. 219–337

[16] M.G. Broadhurst, F. Micheron and Y. Wada, eds., "Special Issue on PVDF and Associated Piezoelectric Polymers," *Ferroelectr.*, **32** (1–4), 1981, pp. 1–247.

[17] K.D. Pae and Y. Wada, eds., "Proc. of US-Japan Seminar on Piezoelectric Polymers, Honolulu, Hawaii, 1983," *Ferroelectr.*, **57** (1–4), 1984, pp. 1–353.

[18] Plato (427–347 B.C.), *Timaeus*, Sec. 80c. See, for example, F.M. Cornford, *Plato's Cosmology (The* Timaeus *of Plato translated with a running commentary)*, Routledge & Kegan Paul Ltd., London, 1948, 376 pp.

[19] J. Curie and P. Curie, "Développement par compression de l'électricité polaire dans les cristaux hémièdres à faces inclinées [Development by Compression of Polar Electricity in Hemihedral Crystals with Inclined Faces]," *Bull. soc. min. Fr.*, **3** (4), April 1880, pp. 90–93.

[20] W.G. Hankel, "Ueber die Entwickelung polarer Elektricität durch Aenderung des Druckes in der Richtung der unsymmetrisch ausgebildeten Axen [On the Development of Polar Electricity through Variation of the Pressure in the Direction of the Asymmetric Axes]," *Ber. Sächs.*, **32**, Nov. 1880, pp. 144-147.

[21] W.G. Hankel, "Ueber die aktino- und piezoelektrischen Eigenschaften des Bergkrystalles und ihre Beziehung zu den thermoelektrischen [On the Actino- and Piezoelectric Properties of Quartz and their Relation to the Pyroelectric]," *Ber. Sächs.*, **33**, April 1881, pp. 52–63.

[22] M.G. Lippmann, "Principe de la conservation de l'électricité ou second principe de la théorie des phénomènes électriques [Principle of Conservation of Electricity or

Second Principle of the Theory of Electrical Phenomena]," *J. phq.*, **10**, Sept. 1881, pp. 381-394.

[23] J. Curie and P. Curie, "Contractions et dilatations produites par des tensions électriques dans les cristaux hémièdres à faces inclinées [Contractions and Dilatations Produced by Electrical Tensions in Hemihedral Crystals with Inclined Faces]," *C.r.*, **93** (26), Dec. 1881, pp. 1137–1140.

[24] W. Voigt, "Allgemeine Theorie der piëzo- und pyroelectrischen Eigenschaften der Krystalle [General Theory of Piezo- and Pyroelectric Properties of Crystals]," *Abh. Gött.*, **36**, 1890, pp. 1–99.

[25] W. Voigt, "Piëzo- und Pyroelectricität, diëlectrische Influenz und Electrostriction bei Krystallen ohne Symmetriecentrum [Piezo- and Pyroelectricity, Dielectric Influence and Electrostriction in Crystals without Centers of Symmetry]," *Nachr. Gött.*, Dec. 1894, pp. 343–372.

[26] J. Curie, "Recherches sur le pouvoir inducteur spécifique et la conductibilité des corps cristallisés [Research on the Specific Inductive Capacity and the Conductivity of Crystallised Bodies]," *An. chim. phys.*, **6** (17), Aug. 1889, pp. 385–434.

[27] P. Curie and S. (*sic*) Curie, "Sur une substance nouvelle radio-active, contenue dans la pechblende [On a New Radioactive Substance Contained in Pitchblende]," *C.r.*, **127** (3), July 1898, pp. 175–178.

[28] P. Biquard, "Les premiers pas dans les recherches sur les ultrasons [The First Steps in the Research on Ultrasonics]," *J. phq.*, **33**, Colloq. C6, Suppl. to No. 11–12, Nov.–Dec. 1972, pp. C6-1–3.

[29] P. Langevin, French Patent 505 703, appl. Sept. 17, 1918, issued Aug. 5, 1920; British Patent 145 691, July 28, 1921; U.S. Patent 2 248 870, appl. June 21, 1920, issued July 8, 1941.

[30] D. Clark, *Plane and Geodetic Surveying*, Vol. I: *Plane Surveying*, 5th ed., revised by J. Clendinning, Constable & Co. Ltd., London, 1957, 673 pp.

[31] W.P. Mason, "Piezoelectricity, Its History and Applications," *J. Acoust. Soc. Am.*, **70** (6), Dec. 1981, pp. 1561–1566.

[32] A.M. Nicolson, "The Piezo Electric Effect in the Composite Rochelle Salt Crystal," *Trans. AIEE*, **38** Part II, Sept.–Dec. 1919, pp. 1467–1485.

[33] W.G. Cady, "The Piezo-Electric Resonator," *Phys. Rev.*, **17** (4), April 1921, p. 531.

[34] G.W. Taylor, J.J. Gagnepain, T.R. Meeker, T. Nakamura and L.A. Shuvalov, eds., *Piezoelectricity*, Vol. 4 of *Ferroelectricity and Related Phenomena*, G.W. Taylor, gen. ed., Gordon and Breach, Science Publishers, Inc., New York, 1985, 406 pp.

[35] W.P. Mason, "Electrical Wave Filters Employing Quartz Crystals as Elements," *Bell Syst. Tech. J.*, **13** (3), July 1934, pp. 405–452.

[36] H.S. van Klooster, "Three Centuries of Rochelle Salt," *J. Chem. Ed.*, **36** (7), July 1959, pp. 314–318.

[37] J. Valasek, "Piezo-Electric and Allied Phenomena in Rochelle Salt," *Phys. Rev.*, **17** (4), April 1921, pp. 475–481.

[38] G. Busch and P. Scherrer, "Eine neue seignette-elektrische Substanz [A New Seignette-Electric Substance]," *Naturwiss.*, **23** (43), Oct. 1935, p. 737.

[39] B.M. Wul and I.M. Goldman, "Dielectric Constants of Titanates of the Metals of the Second Group," *C.r. (Sov.)*, **46** (4), Feb. 1945, pp. 139–142.

[40] B.M. Wul and L.F. Vereshchagin, "Dependence of the Dielectric Constant of Barium Titanate Upon the Pressure," *C.r. (Sov.)*, **48** (9), Sept. 1945, pp. 634–636.

[41] A. Von Hippel, R.G. Breckenridge, F.G. Chesley and L. Tisza, "High Dielectric Constant Ceramics," *Ind. Eng. Chem.*, **38** (11), Nov. 1946, pp. 1097–1109.

[42] B. Jaffe, R.S. Roth and S. Marzullo, "Piezoelectric Properties of Lead Zirconate–Lead Titanate Solid-Solution Ceramics," *J. Appl. Phys.*, **25** (6), June 1954, pp. 809–810.

[43] K.R. Brain, "Investigations of Piezo-Electric Effects With Dielectrics", *Proc. Phys. Soc.*, **36**, 1924, pp. 81–93.

[44] A.V. Šubnikov and B.K. Brunovskij, "On Piezoelectric Amorphous and Crystalline Substances in an Electric Field" (in Russian), *Izv. Akad. Nauk SSSR*, Series 7 (4–5), 1928, pp. 367–374, *q.v.* English abstract by B.C.A. in *Chem. Abstr.*, **23** (18), Sept. 1929, p. 4605.

[45] V.A. Bazhenov and V.P. Konstantinova, "Piezoelectric Properties of Wood" (in Russian), *Dokl. Akad. Nauk SSSR*, **71** (2),1950, pp. 283–286, *q.v.* English abstract by W. Eitel in *Chem. Abstr.*, **45** (7), April 1951, p. 2747.

[46] E. Fukada, "Piezoelectricity of Wood," *J. Phys. Soc. Japan*, **10** (2), Feb. 1955, pp. 149–154.

[47] E. Fukada and I. Yasuda, "On the Piezoelectric Effect of Bone," *J. Phys. Soc. Japan*, **12** (10), Oct. 1957, pp. 1158–1162.

[48] E. Fukada, "Mechanical Deformation and Electrical Polarization in Biological Substances," *Biorheology*, **5** (3), Sept. 1968, pp. 199–208.

[49] P.M. Galletti, M.G. Broadhurst and D. De Rossi, eds., "Proc. of the First International Symposium on Piezoelectricity in Biomaterials and Biomedical Devices," *Ferroelectr.*, **60** (1–4), 1984, pp. 1–317.

[50] H. Kawai, "The Piezoelectricity of Poly(vinylidene Fluoride)," *Jpn. J. Appl. Phys.*, **8** (7), July 1969, pp. 975–976.

[51] Y. Wada and R. Hayakawa, "Piezoelectricity and Pyroelectricity of Polymers," *Jpn. J. Appl. Phys.*, **15** (11), Nov. 1976, pp. 2041–2057.

[52] I. Amato, "Piezo: Tough Plastic With a Sensitive Side," *Los Angeles Times*, Science/Medicine Section, Dec. 4, 1989.

[53] *KYNAR Piezo Film Technical Manual*, Pennwalt Corp., Valley Forge, PA, 1987, 65 pp.

[54] G.M. Sessler, "Piezoelectricity in Polyvinylidenefluoride," *J. Acoust. Soc. Am.*, **70** (6), Dec. 1981, pp. 1567–1576.

[55] L.T. Chen and C.W. Frank, "The Influence of Head-to-Head Defects on the Crystallization of PVF_2," *Ferroelectr.*, **57** (1–4), 1984, pp. 51–62.

[56] K. Tashiro, H. Tadokoro and M. Kobayashi, "Structure and Piezoelectricity of Poly(vinylidene Fluoride)," *Ferroelectr.*, **32** (1–4), 1981, pp. 167–175.

[57] A.J. Lovinger, "Annealing of Poly(vinylidene Fluoride) and Formation of a Fifth Phase," *Macromolec.*, **15** (1), Jan.–Feb. 1982, pp. 40–44.

[58] E.L. Nix, L. Holt, J.C. McGrath and I.M. Ward, "Highly Drawn Poly(vinylidene Fluoride) With Enhanced Mechanical and Electrical Properties," *Ferroelectr.*, **32** (1–4), 1981, pp. 103–114.

[59] Y. Wada and R. Hayakawa, "A Model Theory of Piezo- and Pyroelectricity of Poly(vinylidene Fluoride) Electret," *Ferroelectr.*, **32** (1–4), 1981, pp. 115–118.

[60] N. Takahashi and A. Odajima, "Ferroelectric Reorientation of Crystallites in Polyvinylidene Fluoride," *Ferroelectr.*, **32** (1–4), 1981, pp. 49–59.

[61] *IEEE Standard on Piezoelectricity*, ANSI/IEEE Std 176-1987, The Institute of Electrical and Electronics Engineers, Inc., New York, 1988, 53 pp.

[62] H. Ohigashi, "Electromechanical Properties of Polarized Polyvinylidene Fluoride Film as Studied by the Piezoelectric Resonance Method," *J. Appl. Phys.*, **47** (3), March 1976, pp. 949–955.

[63] J.F. Legrand, "Structure and Ferroelectric Properties of P(VDF-TrFE) Copolymers," *Ferroelectr.*, **91**, 1989, pp. 303–317.

[64] J.V. Chatigny, "Piezo Film Yields Novel Transducers," *Electron. W.*, **57** (17), August 1984, pp. 74–77.

[65] J.E. Hubbard, Jr., " Distributed Transducers for Smart Structural Components," *Proc. of the 6th International Modal Analysis Conference*, Kissimmee, FL, Feb. 8–12, 1988, pp. 856–862.

[66] P.A. Lagace, J.C. Brewer and C.F. Varnerin, "TELAC Manufacturing Course Notes," Technology Laboratory for Advanced Composites, Massachusetts Institute of Technology, Cambridge, MA, 1987, pp. 90.

[67] J.F. Campbell, D.S. Cairns, M.G. Abdallah, E.G. Vanderheiden and L.A. Martinez, "A Multi-Purpose Sensor for Composite Laminates," submitted to *J. Compos. Mat.*, 1990.

[68] Y. Daben, "Composite Piezoelectric Film Made from PVDF Polymer and PCM-PZT Ferroelectric Ceramics," *Ferroelectr.*, **101**, 1990, pp. 291–296.

[69] R.E. Newham, Q.C. Xu, S. Kumar and L.E. Cross, "Smart Ceramics," *Ferroelectr.*, **102**, 1990, pp. 259–266.

[70] S.A. Kokorowski, "Analysis of Adaptive Optical Elements Made From Piezoelectric Bimorphs," *J. Opt. Soc. Am.*, **69** (1), Jan. 1979, pp. 181–187.

[71] T. Sato, H. Ishikawa and O. Ikeda, "Multilayered Deformable Mirror Using PVDF Films," *Appl. Opt.*, **21** (20), Oct. 1982, pp. 3664–3668.

[72] H.S. Tzou and M. Gadre, "Active Vibration Isolation by Polymeric Piezoelectret with Variable Feedback Gains," *AIAA J.*, **26** (8), Aug. 1988, pp. 1014–1017.

[73] H.S. Tzou and M. Gadre, "Theoretical Analysis of a Multi-Layered Thin Shell Coupled with Piezoelectric Shell Actuators for Distributed Vibration Controls," *J. Sound Vib.*, **132** (3), Aug. 1989, pp. 433–450.

[74] H.S. Tzou, "Integrated Distributed Sensing and Active Vibration Suppression of Flexible Manipulators Using Distributed Piezoelectrics," *J. Robotic Syst.*, **6** (6), Dec. 1989, pp. 745–767.

[75] H.S. Tzou and C.I. Tseng, "Distributed Piezoelectric Sensor/Actuator Design for Dynamic Measurement/Control of Distributed Parameter Systems: A Piezoelectric Finite Element Approach," *J. Sound Vib.*, **138** (1), April 1990, pp. 17–34.

[76] R.E. Kalmann and J.E. Bartram, "Control System Analysis and Design Via the 'Second' Method of Lyapunov," *J. Basic Eng.*, 1960, pp. 371–400.

[77] J.M. Plump, J.E. Hubbard, Jr. and T. Bailey, "Nonlinear Control of a Distributed System: Simulation and Experimental Results," *J. Dyn. Syst. Meas. Contr.*, **109** (2), June 1987, pp. 133–139.

[78] J.A. Connally and J.E. Hubbard, Jr., "Low Authority Control of a Composite Cantilever Beam in Two Dimensions," *Proc. of the 1988 American Control Conference*, Atlanta, GA, June 15–17, 1988, pp. 1903–1908.

[79] S.E. Miller and J. Hubbard, "Theoretical and Experimental Analysis of Spatially Distributed Sensors on a Bernoulli-Euler Beam," C.S. Draper Laboratory Report CSDL-C-5953, Cambridge, MA, July 1987, 35 pp.

[80] S.E. Burke, "Shape and Vibration Control of Distributed Parameter Systems—Extension of Multivariable Concepts Using Spatial Transforms," 2 vols., PhD Thesis, Dept. of Mechanical Engineering, Massachusetts Institute of Technology, Cambridge, MA, May 1989, 312 pp.

[81] C.-K. Lee, W.-W. Chiang and T.C. O'Sullivan, "Piezoelectric Modal Sensors and Actuators Achieving Critical Active Damping on a Cantilever Plate," *Proc. of the AIAA/ASME/ASCE/AHS/ASC 30th Structures, Structural Dynamics and Materials Conference*, Mobile, AL, April 3–5, 1989, pp. 2018–2026. Submitted to *J. Acoust. Soc. Am.*

[82] "Shielded Transducers," *KYNAR Appl. Not.*, No. 3, 3 pp.

[83] "Interfacing Piezo Film to Electronic Circuits," *KYNAR Appl. Not.*, No. 7, 2 pp.

[84] P.F. Radice, "Quick Glance Adhesive Chart," *KYNAR Appl. Not.*, No. 9, 1987, 4 pp.

[85] "Lead Attachment Techniques for KYNAR Piezo Film Sensors," *KYNAR Appl. Not.*, No. 20, 4 pp.

[86] "Piezo Film Polarity," *KYNAR Appl. Not.*, No. 21 (Rev. A), March 1990, 6 pp.

[87] M.G. Broadhurst, F. Micheron and Y. Wada, "Guest Editorial," *Ferroelectr.*, **32** (1–4), 1981, p. iii.

[88] W.R. Scott and P.E. Bloomfield, "Durable Lead Attachment Techniques for PVDF Polymer Transducers with Application to High Voltage Pulsed Ultrasonics," *Ferroelectr.*, **32** (1–4), 1981, pp. 79–83.

[89] C.-K. Lee, "Piezoelectric Laminates For Torsional and Bending Modal Control: Theory and Experiment," PhD Thesis, Dept. of Theoretical and Applied Mechanics, Cornell University, Ithaca, NY, May 1987, 199 pp.

[90] S.W. Sirlin, "Piezoelectric Polymer-Based Isolation Mount for Articulated Pointing Systems on Large Flexible Spacecraft," *Astrodynamics 1987*, J.K. Soldner, A.K. Misra, R.E. Lindberg and W. Williamson, eds., Vol. 65, Part I of *Advances in the Astronautical Sciences*, American Astronautical Society, San Diego, CA, 1988, pp. 613–627.

[91] A. Huntington, "Final Report on SIRPNT Lab Work, Summer 1987," Tech. Memo, NASA JPL, Pasadena, CA, Sept. 1987, 2 pp.

[92] M. Toda and S. Osaka, "Electromotional Device Using PVF_2 Multilayer Bimorph," *Trans. IECE Japan*, **E 61** (7), July 1978, pp. 507–512.

[93] R.J. Notestine and J.M. Beninato, "Piezoelectric Film as a Distributed Vibrational Mode Sensor," Final Report, 16.622 Experimental Projects Course, Massachusetts Institute of Technology, Cambridge, MA, Dec. 1988.

[94] A.S. Sedra and K.C. Smith, *Microelectronic Circuits*, Holt, Rinehart and Winston, New York, 1982, 927 pp.

[95] H. Öz and L. Meirovitch, "Stochastic Independent Modal-Space Control of Distributed Parameter Systems," *J. Optim. Theory Appl.*, **40** (1), May 1983, pp. 121–154.

[96] M. Balas, "Active Control of Flexible Systems," *J. Optim. Theory Appl.*, **25** (3), July 1978, pp. 415–436.

[97] L. Meirovitch and H. Baruh, "On the Problem of Observation Spillover in Self-Adjoint Distributed-Parameter Systems," *J. Optim. Theory Appl.*, **39** (2), Feb. 1981, pp. 269–291.

[98] S.A. Collins, C.E. Padilla, E. Schmitz, R.J. Notestine, M. Ramey and A.H. von Flotow, "Design, Manufacture, and Application to Space Robotics of Distributed Piezoelectric Film Sensors," *Proc. of the AIAA/ASME/ASCE/AHS Structures, Structural Dynamics, and Materials Conference*, Long Beach, CA, April 2–4, 1990, pp. 1899-1906.

[99] S.H. Crandall, N.C. Dahl and T.J. Lardner, eds., *An Introduction to the Mechanics of Solids*, 2nd ed., McGraw-Hill Book Co., 1972, 628 pp.

[100] L. Meirovitch, *Analytical Methods in Vibrations*, Macmillan Publishing Co., Inc., New York, 1967, 555 pp.

[101] R.D. Blevins, *Formulas for Natural Frequency and Mode Shape*, Robert E. Krieger Publishing Co., Malabar, FL, 1979, 492 pp.

[102] R. Skelton and P. Likins, "Orthogonal Filters for Model Error Compensation in the Control of Nonrigid Spacecraft," *J. Guid. Contr. Dyn.*, 1 (1), Jan.–Feb. 1978, pp. 41–49.

[103] W.P. Hurty, "Dynamic Analysis of Structural Systems Using Component Modes," *AIAA J.*, 3 (4), April 1965, pp. 678-685.

[104] E. Schmitz, "Modelling and Control of a Planar Manipulator with an Elastic Forearm," *Proc. of the 1989 IEEE International Conference on Robotics and Automation*, Scottsdale, AZ, May 14–19, 1989, pp. 894–899.

[105] W.H. Press, B.P. Flannery, S.A. Teukolsky and W.T. Vetterling, *Numerical Recipes: The Art of Scientific Computing*, Cambridge University Press, Cambridge, 1986, 818 pp.

[106] B. Porter and R. Crossley, *Modal Control: Theory and Applications*, Taylor & Francis Ltd, London, 1972, 233 pp.

[107] A. Gelb, ed., *Applied Optimal Estimation*, The M.I.T. Press, Cambridge, MA, 1974, 374 pp.

[108] S. Timoshenko, D.H. Young and W. Weaver, Jr., *Vibration Problems in Engineering*, 4th ed., John Wiley & Sons, Inc., New York, 1974, 521 pp.

[109] J.C. Bruch, Jr. and T.P. Mitchell, "Vibrations of a Mass-Loaded Clamped-Free Timoshenko Beam," *J. Sound Vib.*, 114 (2), April 1987, pp. 341–345.

[110] E. Schmitz and M. Ramey, "Large Space Manipulators Study," First Annual Report, Contract No. F49620-88-C-0037, Martin Marietta Space Systems, Denver, CO, July 1989.

[111] H.W. Bode, *Network Analysis and Feedback Amplifier Design*, D. Van Nostrand, Inc., Princeton, NJ, 1945, 551 pp.

[112] J. de Luis, E.F. Crawley and S.R. Hall, "Design and Implementation of Optimal Controllers for Intelligent Structures Using Infinite Order Structural Models," Space Systems Laboratory Report No. 3-89, Massachusetts Institute of Technology, Cambridge, MA, Jan. 1989, 198 pp.

[113] D.W. Miller, S.R. Hall and A.H. von Flotow, "Optimal Control of Power Flow at Structural Junctions," *Proc. of the 1989 American Control Conference*, Pittsburgh, PA, June 21–23, 1989, pp. 212–220. To appear in *J. Sound Vib.*

[114] G. Maidanik and D.W. Jorgensen, "Boundary Wave-Vector Filters for the Study of the Pressure Field in a Turbulent Boundary Layer," *J. Acoust. Soc. Am.*, **42** (2), Aug. 1967, pp. 494–501.

[115] F.A. Aupperle and R.F. Lambert, "On the Utitlization of a Flexible Beam as a Spatial Filter," *J. Sound Vib.*, **24** (2), Sept. 1972, pp. 259–267.

[116] N.C. Martin and P. Leehey, "Low Wavenumber Wall Pressure Measurements Using a Rectangular Membrane as a Spatial Filter," *J. Sound Vib.*, **52** (1), May 1977, pp. 95–120.

[117] R.N. Bracewell, *The Fourier Transform and Its Application*, 2nd ed., McGraw-Hill Book Co., New York, 1978, 444 pp.

[118] K.G. Beauchamp and C.K. Yuen, *Digital Methods for Signal Analysis*, George Allen & Unwin, London, 1979, 316 pp.

[119] "The Fundamentals of Signal Analysis," Application Note 243, Hewlett-Packard, Palo Alto, CA, Feb. 1985, 57 pp.